

A Study of Proton Photoproduction on Carbon.

Gillian E Cross

Presented as a Thesis for the Degree of Doctor of Philosophy

Department of Physics and Astronomy,
University of Glasgow,
April 1994.

© Gillian Cross 1994.

ProQuest Number: 13833765

All rights reserved

INFORMATION TO ALL USERS

The quality of this reproduction is dependent upon the quality of the copy submitted.

In the unlikely event that the author did not send a complete manuscript and there are missing pages, these will be noted. Also, if material had to be removed, a note will indicate the deletion.



ProQuest 13833765

Published by ProQuest LLC (2019). Copyright of the Dissertation is held by the Author.

All rights reserved.

This work is protected against unauthorized copying under Title 17, United States Code
Microform Edition © ProQuest LLC.

ProQuest LLC.
789 East Eisenhower Parkway
P.O. Box 1346
Ann Arbor, MI 48106 – 1346

Thesis
9840
copy 1



Tell all the Truth but tell it slant -
Success in Circuit lies
Too bright for our infirm Delight
The Truth's superb surprise
As Lightning to the Children eased
With explanation kind
The Truth must dazzle gradually
Or every man be blind -

Emily Dickinson

Abstract

The work presented in this thesis describes an experimental study of the photodisintegration of the carbon-12 nucleus at intermediate photon energies. This is the first in a series of experiments by Glasgow University in collaboration with Edinburgh and Tübingen Universities at the tagged photon facility at MAMI-B at the Mainz Institut für Kernphysik.

Two nucleon emission in the energy region between 50 and 150MeV has already been studied extensively, the results indicating that photons in this energy range are absorbed by a correlated nucleon pair, the quasi-deuteron mechanism. However, immediately above these energies the photon can be absorbed by single nucleon forming a $\Delta(1232)$ resonance which subsequently de-excites via quasi-free pion production. Previous experiments in the Δ resonance region have suffered from poor resolution and it is therefore the aim of the present experiment to study these competing mechanisms in detail. It is anticipated that such a study will yield information about meson exchange currents, short range correlations and Δ propagation in nuclear matter.

Photons were produced by Bremsstrahlung on a metal foil using 855MeV electrons extracted from MAMI-B and their energies were calculated by momentum analysing the residual electrons using the Glasgow tagging spectrometer. The photons impinge on a natural graphite target and the momenta of the photoreaction products are measured by two new detector arrays PIP and TOF. PIP is a large solid angle ΔE - ΔE -E telescope which was placed at 90° to the photon beam to detect protons and pions. The associated particle is detected by the time-of-flight spectrometer TOF which was placed on the opposite side of the beam covering polar angles 10° - 160° . A segmented ΔE detector was placed near the target in front of TOF to discriminate between charge and neutral particles. The experimental system has missing energy resolution of order 7MeV which is sufficient to resolve the shells from which the nucleons were ejected.

The data was used to study the inclusive (γ, p) reaction channel, and the exclusive (γ, pn) , $(\gamma, p\pi)$ and (γ, pp) reaction channels and is presented in the form of proton energy distributions. These spectra were shown to largely agree with several previous measurements. The variation of the cross sections were studied both as a function of photon energy and of proton angle and were compared to the intranuclear cascade code PICA. This was shown to provide an adequate

comparison to all but the (γ, pp) reaction channel and evidence of the quasi-deuteron and quasi-free pion production mechanisms are observed. However, detailed analysis indicates that PICA is too crude a model to fully describe the data and further initial comparisons to new microscopic calculations are shown. These also provide an adequate description of the data, and the similarity of all models suggests that this method of data presentation is insensitive to the details of the reaction mechanisms.

Declaration

The data presented in this thesis was obtained by the Nuclear Structure group of the University of Glasgow in collaboration with colleagues from the Universities of Edinburgh and Tübingen. I participated fully in all aspects of the preparation and execution of the experiment. The analysis and interpretation of this data is entirely my own work. This thesis was composed by myself.

Gillian E Cross

Acknowledgements

I would like to take this opportunity to express my appreciation to SERC for providing me with a grant, and with all the extra travelling expenses required for these experiments. I would also like to thank Prof Ferrier, the head of Glasgow University Physics Department, for additional funding to go to conferences.

This project would obviously have been impossible without help from the Institut für Kernphysik at Mainz Universität, and I would therefore like to convey my gratitude to Prof Walcher, the then head of the Institut. I should also like to thank Dr Kaiser and his team for providing excellent beam throughout our experiments, and Dr Ahrens for his support as the spokesperson for the A2 collaboration.

I delighted to be able to thank Peter Grabmayr, Torsten Hehl, Ralf Schneider, Tomas Lamparter and Karin Spaeth from Tübingen Universität, and Derek Brandford, John MacKenzie, Doug Johnstone and Tom Davinson from Edinburgh University for all the effort they put into setting up and running the experiments, and for the unfailing friendship during those endless day- and nightshifts, and even longer analysis meetings. In addition I would like to express my gratitude to John MacKenzie and Peter Grabmayr for their hard work and advice in getting PIP and TOF into ACQU.

I would like to say a big thank you to everyone at the Kelvin Lab, academic staff, technical staff and students for all their help and advice both with the experiments and with the analysis. It would also like to thank you for helping to make my time there so enjoyable, and for teaching me so much about getting organised. This would become unbelievably mawkish if I thanked everyone individually, but there are a number of you who I must single out. I would like to start by thanking my supervisors Dr Douglas MacGregor and Prof Robert Owens for their support throughout my studentship. I am immensely grateful to Andy Sibald and Ian Anthony for maintaining an idiot friendly computing system, for tolerating this idiot using it. I would also like to thank Gary Miller for helping me with PICA, and Peter Harty for the many fruitful discussions about data analysis. James Wilson and Scott Lumsden also deserve a vote of thanks for providing a place of sanctuary. Special thanks are due to John Annand without whose efforts the experiments would never have been performed, and without whose patient advice I would not have known how to even get started on the analysis.

I have saved my deepest thanks 'til last. I am indebted to Cameron McGeorge for his valiant efforts guiding me patiently through the mires of data analysis, I would never have got to this stage without his help. I would also like to take this opportunity to say thanks to Rebecca Crawford for being such a ray of sunshine in my life for the past few years. Lastly I would like to thank my family for their support throughout this project, and to apologise to them for my incoherent ramblings about my work.

Perhaps I should also thank the Amazon rainforests for providing 40% of the Earth's oxygen, but then again perhaps not.

Contents

1	Introduction	1
1.1	The Interaction of Photons with Nuclei	2
1.2	Photon Sources	5
1.2.1	Photon Production	6
1.2.2	Monochromatic photon sources	7
1.3	The Quasi-Deuteron Process	8
1.3.1	Testing the Quasi-Deuteron Model	11
1.3.2	Recent Theoretical Developments	14
1.4	The Quasifree Pion Production Mechanism	18
1.4.1	Testing the Quasifree Pion Production Mechanism	18
1.4.2	Recent Theoretical Developments.	21
1.5	Complementary Processes	23
1.5.1	The (γ,N) Reaction	23
1.5.2	Pion Absorption	25
1.5.3	Electron Scattering	26
1.6	Present Work	27
2	Experimental Apparatus	29
2.1	Mainz Microtron	30
2.2	Photon Production and Tagging	34
2.2.1	Photon Production	34
2.2.2	The TAGGER	34
2.2.3	Photon Collimation	37
2.2.4	Tagging Efficiency	37
2.2.5	Photon Beam Viewer	39
2.3	Targets	39
2.4	Particle detector requirements	40
2.4.1	Charged Particle Detectors	41

2.4.2	PIP	43
2.4.3	The TOF Array	49
2.5	Electronics and Data Acquisition	52
2.5.1	Triggers	54
2.5.2	Data Acquisition	60
3	Detector Calibrations	63
3.1	Particle Identification	64
3.1.1	PIP	64
3.1.2	TOF	67
3.2	Walk Corrections	67
3.3	Position Calibrations	70
3.4	Energy Calibrations	73
3.4.1	The TAGGER	73
3.4.2	PIP	74
3.5	Cosmic Ray Data and Gain Monitoring	80
3.5.1	Energy calibrations	80
3.5.2	Droop corrections	80
3.5.3	Gain monitoring in PIP and TOF	82
3.6	Detector Performance	82
4	Data Analysis	85
4.1	Data Reduction	86
4.2	Random and Background Subtraction	88
4.2.1	The TAGGER	88
4.2.2	TOF	90
4.2.3	Yield Calculations	91
4.3	Cross Section Calculations.	93
4.3.1	Tagging Efficiency.	94
4.3.2	Neutron detection efficiency	96
4.4	Statistical and Systematic Uncertainties	98
4.5	Theoretical Simulations.	100
5	Discussion and Conclusions	104
5.1	Comparison with Previous Experiments	105
5.1.1	Inclusive Measurements	105
5.1.2	Exclusive Measurements	110

5.1.3	Checks on Experimental Cross Sections	113
5.2	Comparison between the Data and Theory	114
5.2.1	The $^{12}\text{C}(\gamma, p)$ Reaction	117
5.2.2	The $^{12}\text{C}(\gamma, pn)$ Reaction	121
5.2.3	The $^{12}\text{C}(\gamma, p\pi)$ Reaction	124
5.2.4	The $^{12}\text{C}(\gamma, pp)$ Reaction	127
5.2.5	Other Theories	129
5.3	Conclusions	134

List of Figures

1.1	Total photon absorption cross section	4
1.2	Schematic diagram of a tagging system	9
1.3	Diagrams contributing to two-body absorption	16
1.4	Diagrams contributing to pion photoproduction	19
2.1	Schematic diagram of a racetrack microtron	31
2.2	The Mainz Microtron MAMI-B	33
2.3	The tagging spectrometer	36
2.4	Schematic view of the photon beam line	38
2.5	The layout of the A2 experimental hall	42
2.6	A schematic diagram of PIP	44
2.7	The Start Detector	46
2.8	Schematic diagram of a TOF stand	51
2.9	Segmentation of the TOF ΔE	53
2.10	Schematic diagram of the electronics circuit	55
2.11	The electron reject circuit	57
2.12	The pion identification circuit	57
2.13	The cosmic trigger	59
2.14	Event processing	61
3.1	Particle identification in PIP	65
3.2	Particle identification in TOF	66
3.3	Estimation of rise times	69
3.4	Position calibration	72
3.5	Energy calibration for the E1 layer	76
3.6	Measured vs calculated energy	78
3.7	Energy resolution for protons of energy 50-60MeV	79
3.8	Droop along an E bar	81
3.9	A typical proton energy spectrum	83

4.1	TAGGER TDC spectrum	89
4.2	Relative sizes of real and random components	92
4.3	Relative sizes of target in and target out components	92
4.4	Tagging efficiency as a function of photon energy	95
4.5	Neutron detection efficiency as a function of neutron energy	97
4.6	An example of a $^{12}\text{C}(\gamma, p)$ simulated cross section	103
5.1	The (γ, p) cross section at $E_\gamma \sim 200\text{MeV}$	107
5.2	The inclusive (γ, p) cross section at $E_\gamma \sim 400\text{MeV}$ and $\theta_p \sim 60^\circ$	108
5.3	Renormalised exclusive cross sections at $E_\gamma \sim 300\text{MeV}$ and $\theta_p \sim 60^\circ$	111
5.4	Renormalised exclusive cross sections at $E_\gamma \sim 400\text{MeV}$ and $\theta_p \sim 60^\circ$	112
5.5	The ^{12}C total photoabsorption cross section	115
5.6	The $^{12}\text{C}(\gamma, p)$ cross section at $61^\circ \pm 8^\circ$	118
5.7	The $^{12}\text{C}(\gamma, p)$ cross section at $300 \pm 10\text{MeV}$	119
5.8	The $^{12}\text{C}(\gamma, pn)$ cross section at $61^\circ \pm 8^\circ$	122
5.9	The $^{12}\text{C}(\gamma, pn)$ cross section at $300 \pm 10\text{MeV}$	123
5.10	The $^{12}\text{C}(\gamma, p\pi)$ cross section at $61^\circ \pm 8^\circ$	125
5.11	The $^{12}\text{C}(\gamma, p\pi)$ cross section at $300 \pm 10\text{MeV}$	126
5.12	The $^{12}\text{C}(\gamma, pp)$ cross section at $61^\circ \pm 8^\circ$	128
5.13	The $^{12}\text{C}(\gamma, pp)$ cross section at $300 \pm 10\text{MeV}$	130
5.14	Exclusive cross sections at $E_\gamma \sim 400\text{MeV}$ and $\theta_p \sim 60^\circ$	132
5.15	Inclusive (γ, p) cross sections at $\theta_p \sim 60^\circ$	133

Chapter 1

Introduction

Introductory Remarks

The present experiments probe the contributions of the two basic processes, quasi-deuteron absorption and quasi-free pion production, leading to (γ, NN) and $(\gamma, N\pi)$ reactions. These two mechanisms dominate the photonuclear cross section at intermediate photon energies, and the present measurements allow a complementary study of both processes. This chapter introduces the basic concepts involved in intermediate energy photonuclear physics and the motivation behind the present work. The following sections discuss the production of high energy photon beams, the present theoretical and experimental understanding of the two reaction mechanisms, and other complementary reactions which can aid in the interpretation of these mechanisms.

1.1 The Interaction of Photons with Nuclei

The photon is a very powerful and versatile nuclear probe. In comparison with the strong interaction between the nucleons, the electromagnetic interaction between photon and nucleons is weak. The photon can therefore probe the entire nuclear volume, unlike pions and nucleons whose strong interaction with the nucleus ensures that surface absorption is dominant. Thus reactions such as pion absorption provide an interesting contrast to photonuclear data (see section 1.5.2). In addition, the relative weakness of the electromagnetic interaction both ensures that the photon is unlikely to suffer initial state interactions (ISI), and that the interaction is localised and is therefore able to probe the few particle structure of the nucleus.

In order to understand photonuclear reactions it is important to realise that the nucleus is not simply the collection of independent, elementary protons and neutrons envisaged by the shell model. Instead nucleons can be excited to form resonances and interact with each other, via the exchange of mesons, within the limits of the Pauli principle. Therefore the photon sees the nucleus as a collection of nucleons, mesons and nuclear resonances, and is able to interact with all of these.

Mathematically this means that the nuclear current \underline{j} , which enters the $\underline{j}\cdot\mathbf{A}$ term in the interaction Hamiltonian, is a sum of one-body, two-body and higher order terms. Traditionally the many-body terms are included implicitly by use of Siegert's theorem, allowing the interaction between photons and the nucleus to be

described as a sum of one-body terms via the charge density operator. Although this makes the mathematics much more tractable, the use of the Siegert theorem is an approximation which neglects magnetic transitions and is only strictly valid for low energy photons. It also excludes such constituents as the isobar currents. As a consequence, theorists have now started to devise frameworks which explicitly include the many-body components (see sections 1.3 and 1.4).

Total Photon Absorption Cross Section

The character of the interaction of photons with nuclei varies with photon energy. This is best demonstrated by the total absorption cross section ([1] and references therein) shown in figure 1.1. Figure 1.1 shows the cross section per nucleon as a function of photon energy for a number of elements, and is commonly known as the 'Universal Curve' since between $\sim 100\text{MeV}$ and $\sim 1.5\text{GeV}$ the cross section per nucleon is the same for all complex nuclei (above that is the shadowing region). This can be simply explained if it is assumed that the photon interacts with a body which is similar in size to its wavelength. Therefore the photon sees the nucleus as a single body at 10's of MeV, as a collection of nucleons, mesons and resonances at 100's of MeV, and perhaps as a collection of individual quarks above a few GeV.

At energies below 50MeV , the photon is mainly absorbed by electric dipole transitions within the nucleus. This is described by collective models in which the photon causes a collective electric excitation of the nucleus. Therefore at these energies the details of the cross section are dependent on the nuclear structure and hence dependent on A . The collective models successfully describe the A dependence of the peak position and its width.

In the range of energies between 50 and 200MeV the cross section is thought to be mainly due to the absorption of the photon by two or more interacting nucleons. At these energies conservation of momentum suppresses the direct knock-out of a single nucleon leading to the assumption that the photon is likely to couple to a correlated pair. The similarity of the reaction kinematics in complex nuclei to that of the deuteron, has given rise to the quasi-deuteron model (QD) [2]. This model has been able to successfully describe the broad features of photon interactions at these energies and has led to the development of more sophisticated microscopic models (section 1.3).

The peak at $\sim 300\text{MeV}$ in the proton cross section (figure 1.1) is due to the

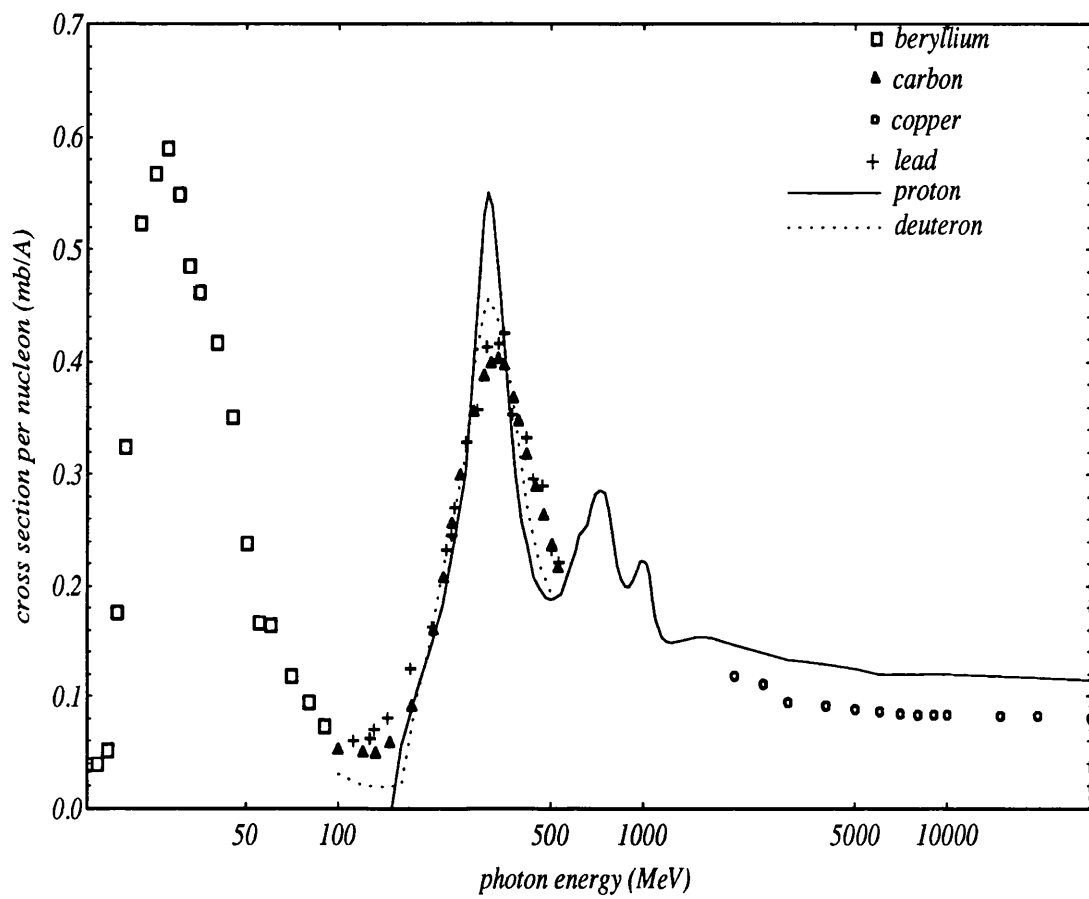


Figure 1.1: *Total photon absorption cross section*

excitation of the $\Delta(1232)$ resonance, the first excited state of the nucleon which decays to a pion and nucleon. The cross section per nucleon for ^{12}C is also shown and this has a strong peak very similar to that of the proton. This is true for all nuclei, and the similarity between the reaction kinematics in complex nuclei and the proton has led to the concept of the quasi-free pion production mechanism (QFPP). The QFPP mechanism assumes that the photon is absorbed by a single nucleon forming a $\Delta(1232)$. The resonance is broadened by the Fermi motion of the nucleons and its strength is decreased by Pauli blocking in nuclear matter. This simple model has also been successful in qualitatively describing the features of the data, and has again led to more sophisticated microscopic models (section 1.4).

The higher baryon resonances evident in figure 1.1 for the proton fall into two groups; the Δ^* resonances with isospin $\frac{3}{2}$ and the N^* resonances with isospin $\frac{1}{2}$. Both groups can decay into a nucleon and a pion, but the N^* resonances can also decay into a nucleon and an eta. Total photonuclear cross section measurements on complex nuclei have been unable to find evidence of these higher resonances. The heavier resonances overlap, and it is not known if this, accompanied by Fermi motion and Pauli blocking, washes out their effect in complex nuclei, or if the present measurements have been too poor to find them. The higher baryon resonances therefore still provide an experimental challenge, and also a theoretical challenge as simple quark models are unable to predict all the known properties of the N^* resonances [3].

Above the baryon resonances, at photon energies greater than ~ 2 GeV, the total photonuclear absorption cross section remains roughly constant with photon energy. At these energies the interaction cross section for the pure photon state becomes negligible. However, the photon has a low probability of being in a hadronic state and can therefore undertake hadron-hadron interactions with the nucleus. The observed cross sections are small due to the low probability of the photon being in a hadronic state. In this process the photon is mainly absorbed on the front side of the nucleus with the result that the remainder of the nuclear volume is 'shadowed'.

1.2 Photon Sources

One of the greatest challenges in photonuclear physics has been the development of intense high energy photon beams of known energy. The methods of producing

photon beams, and of calculating the photons' energies, are described in this section.

1.2.1 Photon Production

The three most common methods of producing photon beams in the intermediate energy range are Bremsstrahlung, inverse Compton scattering and positron annihilation.

- Bremsstrahlung; $e^- + Z \longrightarrow e^- + Z + \gamma$

The deceleration of electrons in the Coulomb field of an atom produces an electromagnetic radiation called Bremsstrahlung. As the nucleus is massive compared to the photon and electron it can be assumed that it receives no energy in this process, and thus the photon's energy is given by

$$k = E_0 - E_1 \quad (1.1)$$

where E_0 and E_1 are the electron's incident and residual energies respectively. Experimentally Bremsstrahlung is produced by passing a high energy electron beam through a thin radiator, the photons being emitted in an intense forward peaked cone.

- Inverse Compton scattering; $e^- + \gamma \longrightarrow e^- + \gamma'$

In Compton scattering a photon is scattered by an atomic electron, causing the photon to lose energy and the electron to be ejected. In the inverse process a photon is scattered by a high energy electron causing the electron to lose energy to the photon. This produces photons of energy

$$k = \frac{4k_1\gamma^2}{1 + \lambda + \chi} \quad (1.2)$$

where $\gamma = \frac{E}{m}$, $\lambda = \frac{4Ek_1}{m^2}$, $\chi = (\gamma\theta)^2$, m is the rest mass of the electron, E is the incident electron energy, k_1 is the incident photon energy and θ is the angle between the incident electron beam and the emitted photon. Experimentally an intense beam of high energy photons is produced by back scattering laser light. This produces maximum photon energies at small θ values;

$$\theta \longrightarrow 0, k \longrightarrow \frac{4k_1\gamma^2}{1 + \lambda} = E \frac{\lambda}{1 + \lambda}.$$

- Positron annihilation; $e^+ + e^- \rightarrow \gamma + \gamma$

When a positron and electron annihilate they produce a pair of photons. Assuming that the electron is initially at rest the higher photon energy is given by

$$k = \frac{m}{1 - \beta \cos \theta} \quad (1.3)$$

where $\beta = \sqrt{\frac{E_{e^+} - m}{E_{e^+} + m}}$, m is the rest mass of the positron and electron, E_{e^+} is the energy of the incident positron and θ is the emission angle of the photon with respect to the positron beam. Experimentally a weak positron beam is produced by bombarding a high Z target with electrons. The positron beam is then passed through a thin radiator producing photons both from annihilation and positron Bremsstrahlung. Again maximum photon energies are produced for small angles where as $\theta \rightarrow 0$, $k \rightarrow E_{e^+} + \frac{1}{2}m$.

Bremsstrahlung was used to produce the photon beam at the tagged photon facility at MAMI-B as it is a simple method which produces a high photon flux.

1.2.2 Monochromatic photon sources

In all but the simplest of nuclei, the knowledge of energy of the photon is required to fully determine the kinematics of reactions in which two particles are emitted. However, all of the processes described above produce photons in a continuum, with the result that any single photon will have some arbitrary energy below the maximum energy determined by the kinematics of the production process. There are three methods of producing photons whose individual energies are known which have been widely used in photonuclear physics.

- The Bremsstrahlung difference technique was developed in order to produce photons of known energies from Bremsstrahlung beams. It involves performing the experiments at two slightly different end point energies and subtracting one set of results from the other, leaving a small range of photon energies. However, this has large systematic uncertainties as the shape of the Bremsstrahlung spectrum is not well known near its end point, making the normalisation difficult. Also the small number of counts near the end point of the Bremsstrahlung spectrum generally results in large statistical uncertainties.

- Both inverse Compton scattering and positron annihilation are two-body processes. Therefore, if the angle of the emitted photon is measured it is possible to calculate its energy. This can be exploited by collimating the beam at an appropriate angle to produce photons with a restricted energy range at the required energy.
- The tagging technique [4] involves measuring the energies of the incident and residual electrons. By demanding a coincidence between the reaction products and the residual electron it is trivial to calculate the energy of a photon produced by Bremsstrahlung. Similar techniques are used for positron annihilation and inverse Compton scattering. Tagging has become widely used in photonuclear experiments as it is able to accurately measure each photon's energy over a wide energy range.

A schematic diagram of a tagging system is shown in figure 1.2. The energy of the incident beam is generally well known. By bending the residual electron in the field of a magnetic spectrometer it is possible to accurately calculate its energy from its exit position, typically using an array of plastic scintillators.

1.3 The Quasi-Deuteron Process

The earliest intermediate energy photonuclear experiments [5] used the entire spectrum of photon energies produced by Bremsstrahlung, typically using electrons of $\sim 300\text{MeV}$. It was found that the spectrum of photoprotons produced fell into two categories; low energy photons produced low energy protons whose distribution had a weak dependence on angle and high energy photons produced high energy protons whose distribution was strongly forward peaked. The first component was successfully explained by the Giant Dipole Resonance where the photon causes a collective excitation of the nucleus which emits nucleons when it de-excites. The second component was less easy to explain. Levinthal and Silvermann [6] suggested that the high energy component could be explained by the absorption of the photon by some sub-unit within the nucleus, for simplicity their calculations assumed a single nucleon. These calculations explained the anisotropy in the proton angular distribution but required the nucleons to have initial momenta far greater than the Fermi momentum to provide the energies measured.

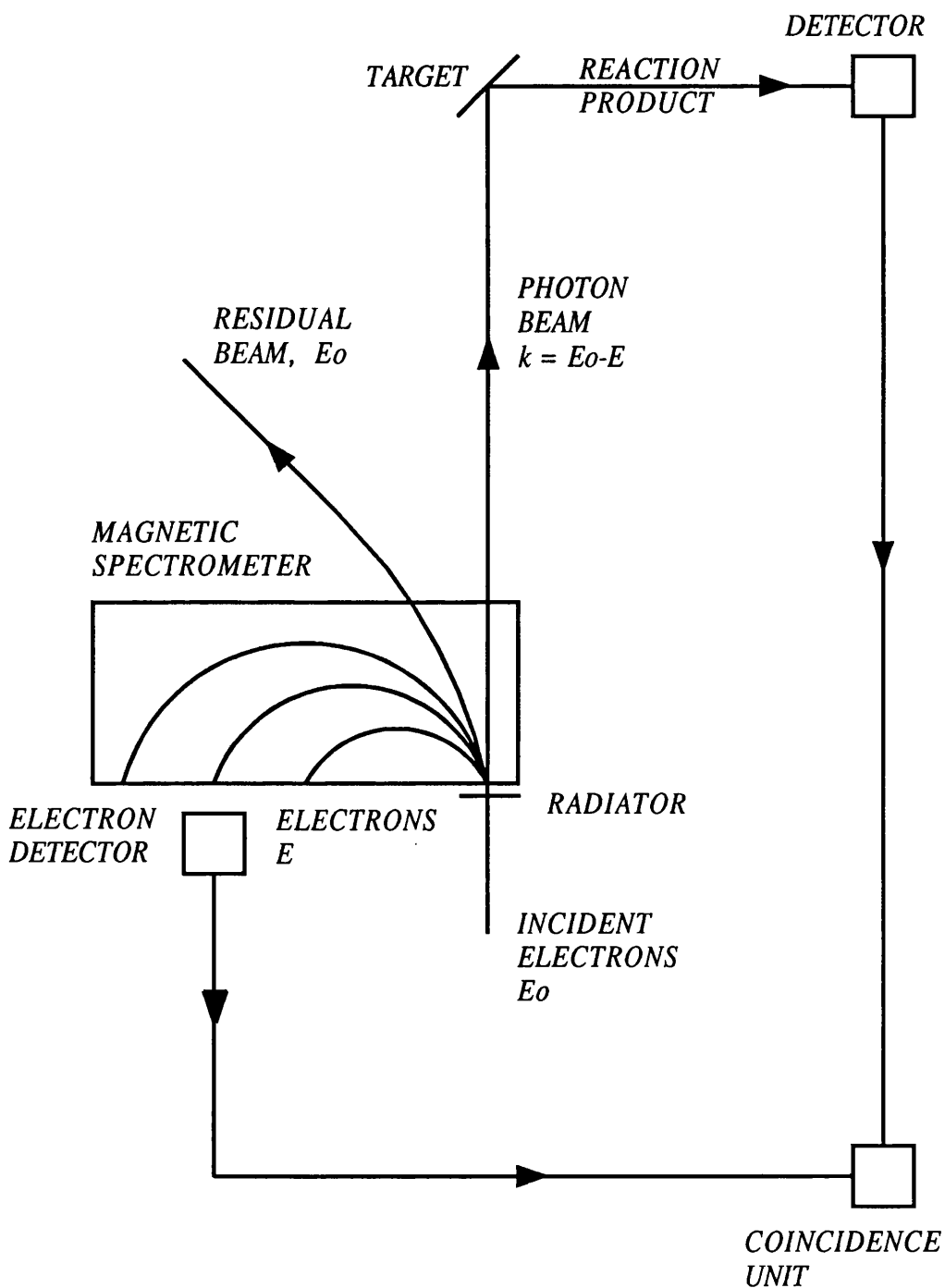


Figure 1.2: Schematic diagram of a tagging system

Levinger [2] suggested that the photonuclear process might be similar to meson capture since both processes have high momentum nucleons in the final state which cannot be provided by an interaction on a single nucleon. It had been suggested that meson capture could take place on a cluster of nucleons, the high momentum component coming from the strong interaction between nucleons at closer than average separation. As the probability of finding three or more nucleons at the required proximity is extremely small, Levinger proposed that the photon is most likely to be absorbed on a nucleon pair. From this hypothesis the quasi-deuteron model was derived. It assumes that the nucleon pair must be a proton and a neutron in order to provide an electric dipole to which the photon can couple. The photodisintegration cross section can then be obtained from that of the deuteron which is assumed to apply to all possible proton-neutron pairs within the nucleus, *ie*

$$\sigma = L \frac{NZ}{A} \sigma_D \quad (1.4)$$

where L is the Levinger parameter, N the number of neutrons, Z the number of protons and $A = N + Z$ is the nuclear mass number. The Levinger parameter L represents the relative probability of two nucleons being near each other in a complex nucleus compared with that in a free deuteron. Levinger obtained the constant 6.4 from his calculations [2], but when experimentalists used the equation to fit their data and theorists used other methods of deriving the formula different values were obtained.

The simple quasi-deuteron model gained credence as it successfully explained the kinematics of photonuclear reactions at intermediate energies. However, it is a naive model and cannot explain the detailed physics of the interaction. In 1957 Gottfried [8] proposed the factorised cross section

$$d\sigma = (2\pi)^{-4} d^3\mathbf{k}_1 d^3\mathbf{k}_2 F(P) S_{fi} \delta(E_f - E_i) \quad (1.5)$$

where the first term relates to the available phase space, $F(P)$ is the probability of finding two initial nucleons at zero separation with momentum $P = |\mathbf{k}_1 + \mathbf{k}_2 - \boldsymbol{\omega}|$ (where $\boldsymbol{\omega}$ is the momentum of the incident photon) in the Slater determinant, and S_{fi} is the transition matrix. The formula was derived assuming that the photonuclear interaction energy is the sum of two-body operators, the residual excitation energy is small compared to the photon energy (allowing the summation over all final states of the residual nucleus), the influence of the other nucleons can be ignored during the interaction, and that the ground state Ψ_0 is the product of short-ranged pair correlations and the Slater determinant of shell model states.

Gottfried's factorised cross section is more rigorous than Levinger's simple quasi-deuteron model. The factor $F(P)$ can be derived from the wavefunctions of the initial nucleons, which can be confirmed by other sources such as electron scattering data. The second factor S_{fi} is analogous to the use of the deuteron cross section in the quasi-deuteron model and is generally of more interest as it contains the dynamics of the interaction. Explicitly contained within the factor S_{fi} are details of the short range correlations (SRC), the change in the nuclear wavefunctions caused by the forces between nucleons at closer than average separation. As a consequence photonuclear experiments have been performed in an attempt to probe the details of these SRCs.

Gottfried retained the essence of the quasi-deuteron model in his calculations by assuming that the photon is absorbed by a pn pair in a relative 3S state. However, he noted that a small cross section for (γ, pp) reactions had been measured experimentally at MIT [9], the magnitude being about 2% of that for (γ, pn) in ^{16}O . It had been suggested that this was due to final state interactions (FSI) in which a neutron knocked out a proton. Gottfried noted that if the cross section was due to a photon being absorbed on a pp pair (which has $T = 1$) the 3S state could no longer contribute, and he suggested that dipole absorption on protons in a relative 3P state is most probable. Continuing in this vein, Gottfried noted that absorption on pn pairs in relative P states should therefore also be allowed. Using the (γ, pp) cross section measured at MIT he calculated that neglecting such processes resulted in the (γ, np) cross section being underestimated by $\sim 7\%$.

1.3.1 Testing the Quasi-Deuteron Model

Early (γ, NN) Experiments

The work by Levinger [2] prompted a series of experiments by groups at MIT and Illinois. These experiments [10], [11], [13] were designed to study the kinematics of the proton-neutron pair in complex nuclei and compare them to the deuteron kinematics. Both groups used continuous energy photon beams produced by Bremsstrahlung with end point energies of 240-320MeV and studied the opening angle between neutrons and fixed energy protons. The results strongly confirmed that the interaction produced proton-neutron pairs and that in the centre of mass frame the average opening angle was the same as that for the deuteron in a number of elements (^4He , ^6Li , ^{12}C and ^{16}O). It was also noted that the angular distributions in complex elements were considerably wider than that in

deuteron and this smearing was assumed to be due to the initial momentum of the quasi-deuteron pair.

Levinger had originally suggested a value of 6.4 for the Levinger parameter for carbon. The group at Illinois obtained $L = 6.3$ in helium and $L = 7.5$ in lithium. When workers at MIT measured L in a variety of elements (${}^6\text{Li} \rightarrow {}^{208}\text{Pb}$) [12] they obtained the result $L \sim 3.0$. They also found that L decreased with A and this was assumed to be due to FSI in the complex nuclei. This discrepancy, and the work by Gottfried, prompted Garvey *et al* at Glasgow [14] to perform similar experiments.

The Glasgow experiment used a Bremsstrahlung beam of end point energy 250MeV and restricted both the angle and energy of both the protons and neutrons. They obtained a value of $L = 10.3$, having corrected for the effects of FSI by assuming an absorption correction factor of 70%. They also suggested that the MIT group had lost most of their expected cross section since the complex nuclei would probably be left in an excited state and therefore the photon could not provide sufficient energy for the kinematics studied. Correcting for the lost yield would increase L by a factor of 2 or 3.

The MIT group also performed an experiment to investigate the importance of the (γ, pp) reaction [9]. Protons from a number of targets were detected by two detectors both at 90° in the centre of mass frame. The results indicated that the ratio of (γ, pp) to (γ, pn) cross sections was 0.4% in ${}^6\text{Li}$ and 2.2% in ${}^{16}\text{O}$. The results were explained assuming (γ, pn) absorption followed by final state interactions.

(γ, NN) Experiments with Tagged Photons

The early experiments were hindered by the technology available. Following several advances recent measurements have been able to improve the quality of the data and therefore have begun to challenge theory properly. The biggest advance has been the use of tagged photons as a result of improvements in electronics and the introduction of high duty cycle accelerators. However, the availability of large solid angle detectors and more reliable measurement techniques have also been an important factor. Therefore, experiments are now able to completely determine the kinematics of reactions where two nucleons have been emitted allowing the residual excitation of the nucleus to be measured experimentally. High resolution (γ, pn) coincidence data have been obtained below the pion production threshold

at both Mainz and Lund on a variety of nuclei. Workers at Bonn and Tokyo have performed similar experiments at higher energies but with poorer resolution. All these experiments are discussed in detail below.

Experiments at photon energies of 80-157MeV by the Glasgow-Edinburgh-Mainz collaboration at Mainz studied (γ, pN) interactions on a number of targets, ^4He [15], ^6Li [16], [17], ^{12}C [18], [19] and ^{16}O [20]. They used a plastic scintillator telescope to detect protons and a time-of-flight spectrometer to detect the associated nucleon. This apparatus has 7MeV missing energy resolution which is sufficient to resolve the shells from which the nucleons were ejected. Results from both carbon and oxygen targets provide quantitative evidence for the QD mechanism, and indicate that much of the strength lies at low missing energy where both nucleons are ejected from the $1p$ shell. At higher missing energies the data are consistent with a QD mechanism where one nucleon is ejected from the $1p$ and one from the $1s$ shell. These experiments also provided good quality (γ, pp) data which suggests that at these energies its cross section is only about 2% of that for (γ, pn) . The (γ, pp) data are more difficult to interpret, but a (γ, pn) initial reaction followed by pn charge exchange in the FSI seems most likely.

The photon tagging system at Lund provides photons of energy $\sim 55\text{-}80\text{MeV}$ with resolution of ~ 300 keV. This has been exploited by a collaboration from Glasgow, Tübingen and Lund who have studied the $^{16}\text{O}(\gamma, pn)^{14}\text{N}$ reaction using a CsI proton telescope and plastic scintillator time-of-flight array. The experimental system has missing energy resolution of less than 2MeV which is sufficient to resolve the low lying states in ^{14}N . This should therefore indicate the isospin of the initial pn pair allowing a comparison of the strengths of absorption on $T = 0$ and $T = 1$ quasi-deuteron states. The analysis of this data is still underway [21]. The same collaboration has also performed a series of experiments to study the A dependence of the (γ, pn) cross section at low energies [22]. A variety of light nuclei between ^6Li and ^{16}O were used and the results suggest that rather than scaling with the total number of pn pairs the cross section in these p -shell nuclei scales with the number of pn pairs with orbital angular momentum $L = 0$.

Homma *et al* have performed a number of photonuclear experiments on a number of targets [23], [24], [25] at the INS in Tokyo using tagged photons in the energy range 187-427MeV with 10MeV resolution. Protons were detected in a magnetic spectrometer at 30° to the photon beam and the associated particle in a set of scintillator hodoscopes. The overall experimental resolution was of the order 35MeV. The proton energy spectra for both single arm and coincidence

measurements support the view that protons are produced by both quasi-deuteron and quasi-free pion production (QFPP) mechanisms (see next section), with the former producing higher energy protons as the mass of the pion does not need to be supplied. The angular correlation between the two nucleons in the QD type events was studied and found to be consistent with simple QD theory for both (γ, pn) and (γ, pp) events. The (γ, pp) yield was found to be $\sim 6\%$ of the (γ, pn) at these higher photon energies.

Further experiments were performed at the INS by Baba *et al* [26] using tagged photons of energies 360-600MeV in order to study photonuclear reactions beyond the $\Delta(1232)$ resonance. Protons from ^{12}C and ^9Be targets were detected by a magnetic spectrometer at a variety of angles (23° , 55° and 130°). Evidence of QD and QFPP mechanisms was observed, and comparison with deuterium data showed that the peaks were significantly broadened by Fermi momentum. The data at backward angles were shown to be purely QD.

Arends *et al* performed experiments at Bonn which were similar to those of Homma *et al*, using tagged photons of energy 200-450MeV with 10MeV resolution again on a variety of elemental targets [27], [28], [29]. Protons and charged pions, were again detected in a magnetic spectrometer and the associated particle in a time-of-flight spectrometer giving an overall experimental resolution of about 15-20MeV. The inclusive measurements again provide evidence of both the QD and QFPP mechanisms and show that final state effects become increasingly important with increasing nuclear mass. The coincidence data also show evidence of both mechanisms, and the increasing ratio of (γ, pp) to (γ, pn) events with photon energy was taken as evidence of a two step process in the former reaction. This is supported by the studies of (γ, pn) and (γ, pp) angular correlations which show that although the (γ, pn) events are markedly quasi-deuteron in nature the (γ, pp) are not.

1.3.2 Recent Theoretical Developments

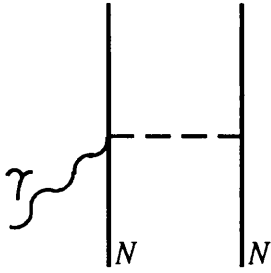
The improved quality of the recent data has prompted new theoretical work by various authors. The quasi-deuteron model used by Levinger and Gottfried assumes that the photon couples to one nucleon and the momentum is shared by a second nucleon. In addition, these models neglect absorption on pp pairs and pn pairs beyond those in a relative 3S state. Finally, the quasi-deuteron wave function is obtained by assuming that the nucleons are initially at zero separation.

Boato and Giannini [30] have performed calculations explicitly including one- and two-body terms. Following theoretical work on few-body systems they include the seagull term (figure 1.3) which has been shown to be the most important of the meson exchange currents (MEC). Their derivation otherwise follows Gottfried's work; neglecting FSI, using closure over the final states and assuming zero separation between the nucleons. They study only (γ, pn) reactions and their calculations retain a factorised form for the cross section in which S_{fi} is now a sum of a one-body term and a two-body term. Numerical calculations indicate that MEC dominate in (γ, pn) reactions. The authors suggest that (γ, pp) reactions might be a more suitable mechanism to study SRC as MEC vanish to first order in such processes.

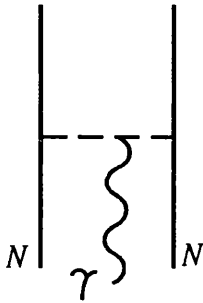
Boffi and Giannini [31] extended this work to include final state effects. They included interactions between the emitted nucleons and the residual nucleus using an optical potential to model the distortion. Assuming that a factorised cross section would still be valid, the distortion effects were included in $F(P)$ and S_{fi} separately. Using this approach S_{fi} now becomes the sum of three factors; a one-body term, a two-body term and a term describing the interference between the first two terms. Results obtained from these calculations show that the main effect of FSI is to produce an overall reduction, rather than distortions, in the cross section whose magnitude depends on the optical potential assumed.

Guisti *et al* [32] have studied contributions to the (γ, pp) cross section in which Δ -isobar configurations (IC) are excited in the intermediate nuclear states. They obtain an unfactorised cross section which includes realistic SRC, and FSI generated by assuming a distorted wave function for the outgoing protons. The work uses a nuclear current which is the sum of one- and two-body terms, but since only (γ, pp) reactions are considered MEC vanish to first order leaving one-body terms and IC. The results of numerical calculations indicate that SRC completely determine the one-body current and that its contribution to the cross section increases with the strength of the correlation.

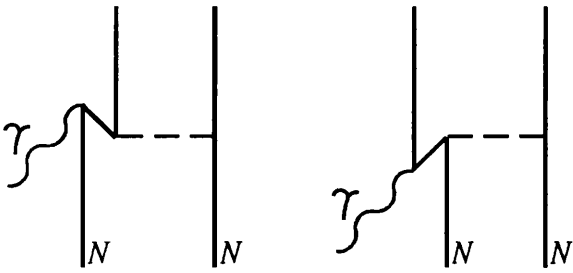
This work has been extended to cover (γ, pn) reactions by Boffi *et al* [33]. Their nuclear current again contains one-body and IC terms, and the two-body current is represented by the dominant seagull current. The results of these numerical calculations show that absorption by nucleon pairs in a 3S state is dominant, confirming the basis of the quasi-deuteron model. It is also shown that although the seagull term is dominant at low photon energies its strength



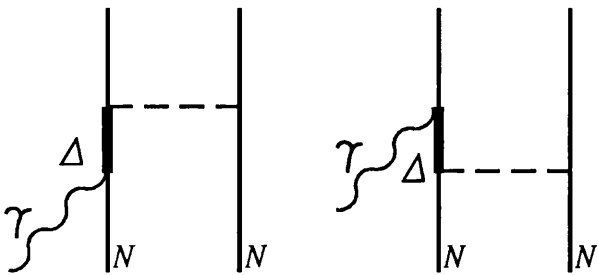
(a) *Seagull current*



(b) *Pion-in-flight current*



(c) *Pair current*



(d) *Isobar Resonance Current*

Figure 1.3: *Diagrams contributing to two-body absorption*

decreases with photon energy whereas the one-body and IC terms increase. At these high photon energies it is the strength of the short range correlation used that determines which term dominates the cross section, the stronger the correlation the stronger the one-body term.

Ryckebusch *et al* [34] have performed calculations to investigate the validity of a factorised cross section and the importance of the various two-body currents. Their calculations include the seagull and pion-in-flight meson exchange currents and the isobar current, but neglect the effects of FSI in this preliminary analysis. Their results support the view that the seagull current is dominant at intermediate energies, but show that destructive interference with the pion-in-flight term results in the factorised forms of the calculation overestimating the magnitude of the cross section due to the two-body currents. The Gent group also find that absorption on $T=1$ pairs is not negligible, and this seems to be needed to account for recent (γ, p) measurements [35]. However, their calculations show that at higher energies the Δ resonance becomes dominant and in this energy region there is evidence that pn pairs behave in a more quasi-deuteron like manner, and a factorised cross section is more justifiable at these energies.

Ryckebusch *et al* have extended their calculations to include FSI effects [36] to account for the strong interaction between the emitted nucleons and the residual nucleus. These effects are introduced to their unfactorised calculations in a distorted wave approach in which the partial waves of the outgoing nucleons are allowed to interact with the residual nucleus. This approach is not appropriate within the framework of a factorised cross section. It is noted that present techniques are not able to include the effects of interference between the emitted nucleons with the result that the two particles are independent of each other after the initial photonuclear interaction. The results of these calculations, like those of Guisti *et al*, show that the main effect of the FSI considered is to reduce the cross section and not distort it. This was ascribed to the independence of the nucleons after the interaction.

By only considering the lightest of the exchange mesons, the pion, the above calculations are essentially limited to energies below 300MeV. Ryckebusch *et al* [37] have therefore started to investigate the effects of the heavier mesons, ρ , σ , ω , on the photonuclear cross section. They include seagull, -in-flight and pair meson exchange currents and the isobar current for the π and ρ , and the pair current for the σ and ω . For simplicity, the calculation uses a factorised cross section of the form derived by Gottfried (see equation 1.4), and neglects the effects of FSI.

The numerical results suggest that the σ and ω meson contributions to the cross section are negligible. On the other hand, destructive interference between the π and ρ mesons results in a reduction in cross section from both the exchange currents and the Δ current.

Carrasco and Oset [45],[46],[47] have also developed a microscopic model of photonuclear reactions in the $\Delta(1232)$ resonance region. This is discussed fully in section 1.4.2 under quasi-free interactions.

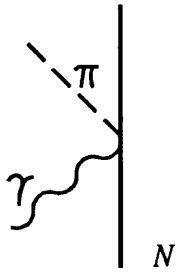
These various theoretical models have moved away from the simple, phenomenological ideas in an attempt to understand the “quasi-deuteron” mechanism in complex nuclei on a microscopic level. Each group is interested in different aspects of the photonuclear cross section, but there is a great deal of overlap in the ingredients which have been included in the calculations. It is only by detailed comparison between the various models and with high quality experimental data that the effects of the different mechanisms can be truly explored.

1.4 The Quasifree Pion Production Mechanism

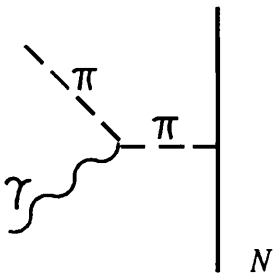
The above arguments assume that the photon must be absorbed by a pair of nucleons to provide the momentum of the emitted particles. Above the pion production threshold the photon can couple to a single nucleon and its energy can be used to emit a pion-nucleon pair either directly or through the creation and decay of a $\Delta(1232)$ resonance. This is the quasi-free pion production mechanism and the most important terms contributing to it are shown in figure 1.4. The interactions of the $\Delta(1232)$ resonance in nuclear matter are both broadened by the effects of the Fermi momentum of the nucleon and FSI and weakened by the constraints of the Pauli principle on the decay of the resonance.

1.4.1 Testing the Quasifree Pion Production Mechanism Early Experiments

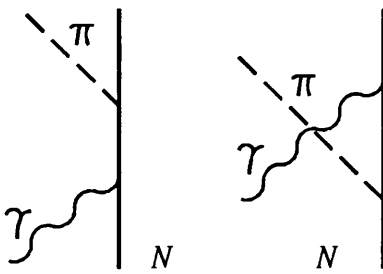
The photoproduction of charged pions was also studied before the widespread use of tagged photon beams, both using continuous energy spectrum beams [39] and using the Bremsstrahlung difference technique [40],[41],[42]. The former measurements detected photopions produced by beams of end point energies typically 300-600MeV on a variety of targets from ^1H to ^{238}U . Experiments showed that the yield of photopions from complex nuclei relative to that of hydrogen does



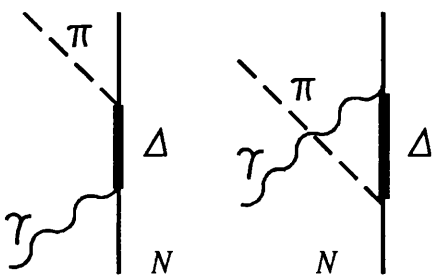
(a) *Seagull Current*



(b) *Pion Current*



(c) *Direct and Crossed Nucleon Currents*



(d) *Direct and Crossed Delta Currents*

Figure 1.4: *Diagrams contributing to pion photoproduction*

increase with A , but not linearly, confirming the importance of Pauli blocking and final state interactions in complex nuclei. Indeed, the results showed an $A^{\frac{2}{3}}$ dependence, and this was explained by assuming that only surface absorption was important, pions resulting from reactions in the interior being totally removed by FSI.

The experiments exploiting the Bremsstrahlung difference technique again detected the photopions and these have sufficient energy resolution to ensure that only one pion was emitted in the reactions studied. The differential cross section, $d\sigma/d\Omega_\pi$, in complex nuclei as a function of photon energy was again shown to be similar in shape to that of the free proton [40], its peak was again shifted to higher photon energies and smeared due to the effects discussed above. The doubly differential cross sections, $d^2\sigma/d\Omega_\pi dT_\pi$, were studied as a function of the pion momentum [41], [42] and were shown to have a broad peak at low momentum. This peak is at lower pion momentum than that of the free proton, but the size of the shift is independent of both photon energy and pion angle. The peak is also broader than that of the free proton, and the broadening increases with both photon energy and pion angle due to the Fermi momentum of the initial nucleon. The area of the peak is similar for both charges of pions, and the ratio of the two cross sections in carbon is very similar to that of the deuteron suggesting that in these reactions the nucleon can be considered quasi-free.

Recent experiments at Tomsk and MIT (see for example [43] and [44]) have measured the energies and momenta of both emitted particles allowing the reconstruction of the energies of the photon and residual nucleus. Such reactions are relatively independent of the structure of the target nucleus and can therefore be expected to provide detailed information about the reaction mechanism.

The experiments at Tomsk [43] on carbon measured the cross section as a function of proton energy at various photon energies. The results suggest that at low missing energies the neutron is emitted from the p -shell and at higher missing momenta from the s -shell, and are in reasonable agreement with DWIA (distorted wave impulse approximation) calculations assuming that the initial reaction was quasi-free. Further analysis of the data has shown evidence of exchange effects, particularly in reactions in which π^0 's were emitted, and Δ formation.

The experiments at MIT [44] used an oxygen target. The cross section was measured at two pion angles as a function of the proton out-of-plane angle. The results at backward angles show reasonable agreement with a DWIA calculation, but are a factor of 4 smaller than the calculation at forward angles. This

discrepancy may be evidence of Δ -medium effects.

Tagged Photon Experiments

The experimental advances discussed in connection with experiments on the quasi-deuteron process have also led to an improvement in the photopion production measurements. The work performed by the groups at Tokyo and Bonn covers energies above the pion production threshold allowing a first comparison between quasi-free pion production and quasi-deuteron absorption mechanisms.

Homma *et al* were able to identify both the QD and QFPP mechanisms in their single arm proton spectra as mentioned earlier, and discriminate between them. They showed that the cross section as a function of photon energy for both reactions has a broad peak at the Δ resonance, suggesting that the formation of the $\Delta(1232)$ resonance is important for the QD mechanism as well as for QFPP. This peak for the QFPP mechanism was seen to move to higher photon energies for increasing A and this was ascribed to the increased binding effects in heavier nuclei. Once FSI were taken into account, the magnitudes of the cross sections due to the two reactions were shown to increase linearly with A .

Arends *et al* also concentrated on single arm measurements, but they have studied both proton and charged pion spectra. Selection on the coincident particle was only attempted for the proton data, but this provides strong evidence of QFPP. The single arm pion cross sections were found to agree with their Monte Carlo simulation code PIKI, and with the theoretical models of both Laget and Carrasco and Oset ([29] and references therein). The proton data were also compared to the various theoretical models and were shown to be less well described. Studies of the A dependence for all three charged particles showed that protons were emitted preferentially over either charge of the pion, and this was taken as evidence of proton emission as the result of pion absorption.

1.4.2 Recent Theoretical Developments.

Carrasco and Oset have recently extended their work on pion absorption to derive a microscopic model of photonuclear reactions in the $\Delta(1232)$ resonance region [45]. Their starting point is the elementary $\gamma N \rightarrow \pi N$ reaction. This is modelled by including all the basic couplings between photons, nucleons, pions and isobars and provides a fair description of the differential cross sections in the (γ, π) channels on the proton and neutron. The calculations were then extended to account

for the effects of the other nucleons in complex nuclei by considering the photon self-energy in an infinite nuclear medium, including all the terms required for their elementary model. The interactions of the pions and Δ s inside the nucleus are treated within the framework of ph and Δh (particle-hole and Δ -hole) effective interactions, with a systematic many-body expansion up to $3p3h$ being included. The finite nuclear size is introduced by means of local density approximations. The model is then used to calculate total photon absorption cross sections, the results being able to reproduce the experimental data in ^{12}C , ^{16}O and ^{208}Pb in the Δ resonance region to within the 10% accuracy expected from the assumptions made.

In these studies photon absorption leading to the emission of two or more nucleons is split into two modes, direct and indirect absorption, and the calculation is able to differentiate between. Direct absorption is a single step process in which the photon is absorbed on two or more nucleons via the exchange of virtual pions, and it is this process which provides the cross section below the pion production threshold. Indirect absorption is a two step process in which the photon is absorbed by a nucleon and produces a pion which is later absorbed before it leaves the nucleus producing an NN pair.

Carrasco *et al* have further extended this work to study inclusive (γ, π) reactions [46] and (γ, N) and (γ, NN) reactions [47]. The model is unable to fit various experimental (γ, π) , (γ, N) and (γ, NN) differential cross sections as well as it did the total cross sections. The difficulty in fitting the differential cross sections for all reactions may be due to details of the nuclear structure which are not well represented by the modelling method, and which largely get washed out when calculating total cross sections.

Separate calculations have been carried out by Li and co-workers who have performed a full non-localised DWIA analysis of the $(\gamma, \pi N)$ reaction [48] to study effects such as the ΔN interaction. Previous analyses of the (γ, π) reaction have shown that since the nucleon remains bound this cross section is very sensitive to the nuclear structure of the target. Therefore as the nucleon is emitted in the $(\gamma, \pi N)$ reaction it should be less sensitive to the nuclear structure and hence reveal more information about the reaction mechanism.

In the calculations harmonic oscillator wavefunctions, with the oscillator parameter chosen to fit $(e, e'p)$ data, are used to describe the initial nucleon. The interaction is modelled using the Blomqvist-Laget pion production operator [49]. As the reaction is still somewhat sensitive to the nuclear structure, a finite nucleus

calculation is required. The analysis uses a full non-localised DWIA calculation where the interaction of the outgoing nucleons are modelled by optical potentials.

The results have been compared to the $(\gamma, \pi N)$ experimental data from Tomsk and MIT described in section 1.4.1. The calculations are shown to be in reasonable agreement with the data from Tomsk but overestimate the data from MIT which has poorer statistical accuracy. The detailed comparison shows that the inclusion of non-local effects is important in such reactions, and that the inclusion of FSI decrease rather than distort the cross sections. The poor agreement with the forward angle MIT data is again seen as possible evidence of Δ -medium effects and it was noted that a reduction in the Δ mass gives better agreement. This suggests that a more sophisticated model for the interaction, such as coupled channel or Δh calculation, may be required to fully explain the experimental data.

In summary the theoretical calculations predict that in the Δ resonance region QFPP is the largest component in the total photon absorption cross section. This is borne out by experimental results, but there are very little detailed $(\gamma, N\pi)$ data available to test the recent microscopic calculations which are very involved. Both QFPP and QD mechanisms have been shown to be important in (γ, NN) reactions, showing the necessity of studying both reactions in parallel in this energy region.

1.5 Complementary Processes

The (γ, NN) and $(\gamma, \pi N)$ reactions discussed above are not studied in isolation. There are a number of complementary processes which have very similar features and comparisons between these different processes aid in the understanding of each of them. A number of these complementary processes are discussed below.

1.5.1 The (γ, N) Reaction

Single arm (γ, N) experiments have long been studied and were initially expected to provide information on quasi-free knock-out (QFK) in nuclei. These experiments concentrated on (γ, p) measurements as QFK (γ, n) reactions are strongly suppressed since the photon can only couple weakly to the magnetic moment of the neutron. However, early results suggested somewhat surprisingly that the (γ, n) cross section was of similar magnitude to that of the (γ, p) . In response

Schoch proposed the so called modified quasi-deuteron mechanism (MQD) [50]. This suggests that neither reaction was due to QFK, but instead both arose from two-body absorption followed by the emission of one nucleon and the reabsorption of the other. Calculations performed using this model required a Levinger parameter of 5.4 to account for $^{16}\text{O}(\gamma, n)$ data, similar to the values needed to account for (γ, pn) data (section 1.3.1).

Recent data from Mainz have again shown evidence of the MQD mechanism. The $^4\text{He}(\gamma, p)t$ cross section [51] was scaled as a function of momentum mismatch between the ingoing photon and outgoing proton using both QFK and MQD models. Both models show clear scaling behaviour of the data but the QFK mechanism shows agreement with theoretical momentum density calculations only below 300MeV/c momentum mismatch whereas there is reasonable agreement with the predictions of the MQD model up to 500MeV/c.

The early (γ, N) measurements had poor resolution, and usually used the whole Bremsstrahlung spectrum of photons, and were therefore unable to properly resolve the final states of the residual nucleus. Recent (γ, p) measurements have achieved missing energy resolutions of $\sim 500\text{KeV}$ allowing comparison with high resolution $(e, e'p)$ measurements [35], [52], [53]. These show that although there is a great deal of similarity between the states excited by QFK in $(e, e'p)$ reactions and the (γ, p) reactions, there are additional states strongly excited by (γ, p) reactions which cannot be explained by a QFK mechanism. In an attempt to describe all states excited by (γ, p) reactions Ryckebusch *et al* studied the effect of one pion exchange currents through RPA calculations [54]. These calculations were able to successfully model the experimental results assuming a $2h1p$ mechanism, essentially the mechanism required by the quasi-deuteron model.

There is now a program of high resolution (γ, n) measurements underway. Early results from both MIT [55] and Lund [56] show a marked similarity between the states populated by (γ, p) and (γ, n) reactions. This again provides compelling evidence that QFK is not the dominant mechanism in (γ, N) reactions even at energies as low as 60MeV. However, detailed comparison between the experimental data [56] and Ryckebusch's calculations [54] has shown that this RPA model cannot describe the (γ, n) data as successfully as the (γ, p) .

1.5.2 Pion Absorption

Pion absorption is similar to photon absorption in that both particles are bosons and have small masses in comparison to that of the nucleons, resulting in the requirement that the absorption must be via a multi-nucleon mechanism for both momentum and energy to be conserved. However, pions interact strongly with the nucleons and therefore absorption is predominantly a surface interaction although processes in which an intermediate Δ propagates through the nucleus result in non-local reactions in which more central nucleons can participate.

Despite absorption being an important channel in the interactions between pions and nuclei, contributing about one third of the total cross section, it has been neglected by both experiment and theory until recently. Previously it had been widely assumed that both ISI and FSI would be important and would smear the reaction signatures, making interpretations of pion absorption difficult. However, it has since been shown that Pauli blocking, nuclear binding and the Fermi momentum wash out the effects of ISI, and the suggested importance of FSI has been reduced as recent estimates of mean free paths within the nucleus are greater than previously thought.

Absorption on a nucleon pair is assumed to be via a quasi-deuteron type interaction with two nucleons being emitted and the residual nucleus acting as a spectator. Kinematically complete experiments on ^3He [58] where both emitted nucleons are detected have shown excellent agreement with such a theory, the shape of the cross section following that for the deuteron at all energies. Experiments on heavier nuclei (^6Li [59] and ^{16}O [60]) have shown similar features and have confirmed that the cross section scales with the number of available nucleon pairs.

However, these experiments have also shown that only half of the absorption cross section is accounted for by the quasi-deuteron absorption mechanism in complex nuclei. The remainder is assumed to come from absorption on more than two nucleons. The experiments on ^3He were able to reconstruct the momentum distribution of the third nucleon and showed that it is only described by the Fermi-momentum distribution at low pion momenta. Above this the distribution can be described by a model in which the final particles share the available phase space. Moreover, these results did not favour two nucleon absorption preceded by ISI and/or followed by FSI; instead genuine three nucleon absorption was suggested. In heavier nuclei (*eg* [60], [61]) there is evidence of $3N$ absorption at

the 10-30% level, although in all of these measurements the kinematic coverage or resolution was insufficient to allow detailed analyses of the exact mechanism to be attempted. The nature of this multi nucleon absorption is not yet understood.

1.5.3 Electron Scattering

Electron scattering proceeds via the exchange of a virtual photon and therefore its study provides a valuable comparison to photonuclear experiments since the momentum of a virtual photon can be varied independently of its energy. Furthermore, as a virtual photon has a longitudinal as well as a transverse component it is able to probe the single particle structure of nuclei. The longitudinal response function is particularly sensitive to the nucleonic degrees of freedom whereas the transverse response is sensitive to the pionic components of the nuclear wavefunction.

Inclusive (e, e') measurements in quasi-free kinematics ($\omega \approx q^2/m$) have long shown that for nuclei with $A > 4$ the transverse response function agrees with mean field calculations whereas the longitudinal response is quenched by 20-40% ([62], [63] and references therein). More detailed information is available from exclusive ($e, e'p$) experiments which are normally performed with parallel kinematics, *ie* with the incident and scattered electron in the same plane as the outgoing proton, and with the proton momentum parallel to the momentum of the residual nucleus. In these kinematic conditions there is no interference between the longitudinal and transverse components. These exclusive measurements have achieved missing energy resolution of as little as 100 keV allowing the complete determination of the momentum and energy distributions of individual quantum orbits. These measurements still find a loss of strength in the longitudinal component with respect to QFK calculations, but the magnitude of the discrepancy has been reduced to between 10 and 20%, and this is only observed in the continuum above the two nucleon emission threshold, [62]. It has been suggested, [62], that the transverse strength is enhanced by effects such as meson exchange currents and final state interactions, and therefore that this anomaly is evidence of correlations in nuclear many-body systems.

Further evidence for multi-nucleon mechanisms is given by measurements in the so called dip region. Between the QFK and $\Delta(1232)$ resonance peaks there is an excess of strength which cannot be accounted for by the tail of either peak, [62]. Measurements show that this region is almost purely transverse and the

missing energy spectra are quantitatively similar to those of pion absorption and photonuclear experiments.

Above the dip region the cross section is dominated by the Δ resonance. This too is almost purely transverse with evidence of both the one-body ($\gamma^* + N \rightarrow \Delta \rightarrow N + \pi$) mechanism and the two-body ($\gamma^* + 'd' \rightarrow \Delta N \rightarrow n + p$) mechanisms being observed, [62].

To fully explore the two-body mechanisms and the effects of nucleon-nucleon correlations ($e, e'NN$) triple coincidence measurements are needed. These have not been possible technically in the past, and are still very difficult, but are now being attempted for the first time at NIKHEF [64], although the statistical accuracy expected is very much poorer than can be achieved in photon induced reactions.

1.6 Present Work

The experiments at MAMI-B are intended to probe the detailed mechanisms in both the (γ, NN) and $(\gamma, \pi N)$ reactions. In the case of the (γ, NN) reactions the expected 7MeV missing energy resolution is sufficient to determine the nucleons initial shells and hence their initial momentum distributions. The increased phase space coverage compared to earlier experiments should provide a more stringent test of the quasi-deuteron mechanism, and improve the knowledge about the comparative strength and origin of the (γ, pp) reaction. The $(\gamma, \pi N)$ data are the first to accurately measure the kinematics of these reactions and should provide new information about the propagation of the Δ through nuclear matter as well as shedding light on the underlying physics in quasi-free pion production.

The present experiment is the first in a series of (γ, NN) and $(\gamma, \pi N)$ measurements on light nuclei and as such is intended to provide a general survey of photon absorption mechanisms. Later work will concentrate on more restricted areas of phase space to probe regions of reaction kinematics which are thought to be most sensitive to the models used. The work presented in this thesis is primarily concerned with the development of a charged particle detector PIP and its use in the analysis of $^{12}\text{C}(\gamma, NN)$ data taken at photon energies from 200 to 500MeV. It follows the general approach of the previous work by Arends *et al*, Homma *et al* and Baba *et al* by comparing the features of the proton energy spectra for the inclusive (γ, p) reaction channel and exclusive (γ, pn) , $(\gamma, p\pi)$ and (γ, pp) reaction channels. The earlier data were used to provide a comparison to the present data

which significantly extends and improves on these previous studies as a much larger phase space is covered by both detectors, the missing energy resolution has been significantly improved and better statistics have been obtained. The interpretation of the analysed data has been guided by calculations carried out using the code PICA which is described in section 4.5. Further theoretical comparison is provided by the newer microscopic calculations of Ryckebusch *et al* and Carrasco and Oset.

Chapter 2

Experimental Apparatus

Introduction

The present experiment was carried out using the Glasgow photon tagging spectrometer installed at the Institut für Kernphysik at Mainz University. The system used is described in detail below and fully determines the kinematics of (γ, NN) and $(\gamma, \pi N)$ reactions.

The electron beam hits a thin radiator producing Bremsstrahlung photons whose energies are calculated from the trajectories of the associated recoiling electrons in the tagging spectrometer. The photon beam is collimated before impinging on a target, and the reaction products are detected by two large particle detectors PIP and TOF placed opposite each other on either side of the photon beam. PIP is a segmented ΔE - ΔE -E telescope which measures both the energies and trajectories of protons and pions. Associated particles are detected in TOF, an array of plastic scintillators which measures particle energies using the time of flight technique. The data acquisition system collates the signals recorded by the electronics and transfers them to the controlling computer for on-line analysis and subsequent storage on magnetic exabyte tapes.

2.1 Mainz Microtron

The electron beam was provided by the Mainz Microtron, MAMI-B, which came into operation in 1990 [65]. It is a cascaded racetrack microtron delivering electrons of energy 855MeV at currents of up to $100\mu\text{A}$, although for tagging the current was always less than 100nA.

Principles of Operation

In a microtron a low energy electron beam is injected into an accelerating section and recirculated by two bending magnets. At each pass the electrons gain sufficient energy to increase their orbit length by an integer number of wavelengths of the accelerating field ensuring that they are returned to the accelerating section in phase with the field. The increase in orbit length also causes the electron's return paths to diverge allowing each to travel through separate beam pipes and be steered and focussed separately, also facilitating extraction. Since the beam may be recirculated many times only modest energy gain is required at each pass, reducing the power density requirements of the accelerating section.

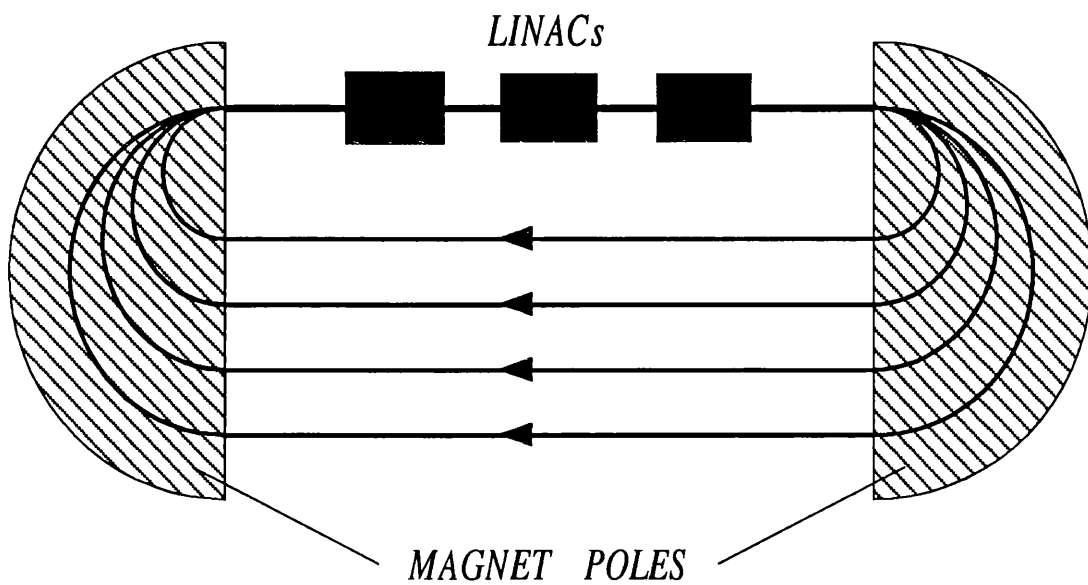


Figure 2.1: *Schematic diagram of a racetrack microtron*

In a racetrack microtron (RTM) a linear accelerator section (linac) is used as the accelerating section, the name RTM coming from the characteristic shape (figure 2.1). The linac accelerates the electrons down waveguides using a radio frequency (RF) electric field provided by klystrons. The low power density requirements of the microtron allow the linac to be operated in continuous wave mode. Although the electron beam retains the RF microstructure it can be considered DC for practical purposes as the GHz modulation is too fast to be observed by the particle detectors. A DC beam is essential for most coincidence experiments as it reduces the random backgrounds and high dead times during the high current pulses produced by low duty cycle (pulsed) machines while producing the same average current.

Since microtrons are designed to return the electrons to the linacs in phase with the RF field the electrons should all have the same energy. However, due to the characteristic called phase stability a slight divergence in the phase, and therefore energy, is accommodated. Electrons which have a slightly lower energy than those in phase with the RF field (resonant electrons) have a slightly smaller orbit and hence arrive back at the linac ahead of the RF field. These electrons are accelerated with respect to the resonant electrons causing a relative increase in their orbital period and therefore they converge towards the energy of the resonant electrons and the phase of the RF field. Similarly electrons of slightly higher energy than the resonant electrons also converge due to their relative deceleration causing a decrease in orbital period. However, electrons which are at the wrong energy would never reach the correct energy (but only oscillate around it) in the absence of synchrotron radiation. In practice this causes all electrons to deviate from the correct energy to some extent, but also provides those electrons away from the correct energy with a mechanism to approach the correct value.

MAMI-B

The increase of energy achievable in a microtron is determined by the number of electron orbits and the energy increase per orbit. The energy increase is limited by the power that the linac is able to dissipate, and the number of orbits by the size of the magnet pole faces. To produce a high energy DC electron beam MAMI-B uses a cascaded design with three separate RTMs (figure 2.2) which reduces the relative energy gain required at each stage. This design also allows

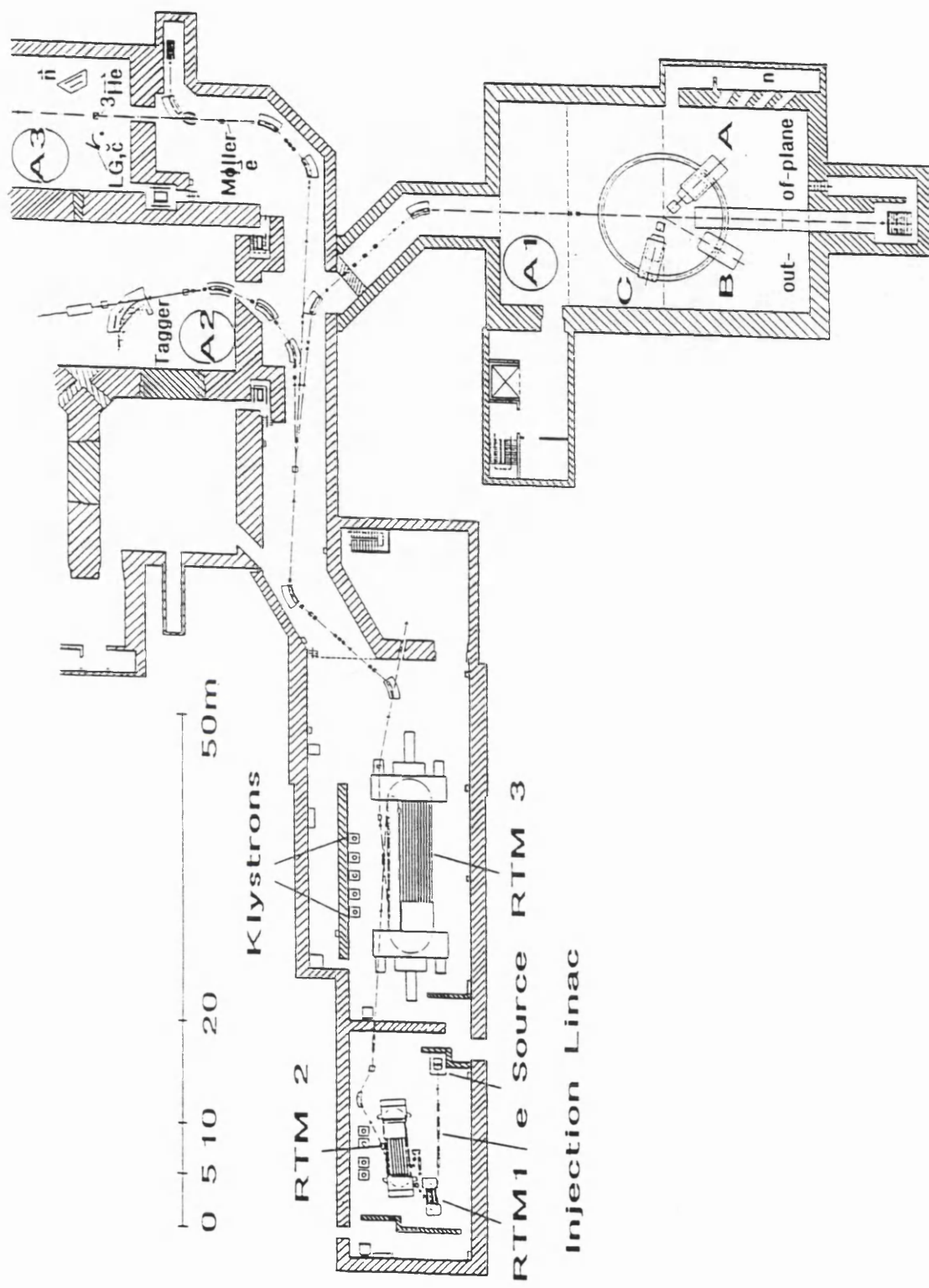


Figure 2.2: *The Mainz Microtron MAMI-B*

additional treatment of the electron beam between the stages to compensate for the weak focussing and fringe field deformation inherent in RTMs.

The electron beam is supplied by a 3.5MeV linac. This is injected into the 14MeV 18 turn RTM1 which is then injected into the 180MeV 51 turn RTM2. The third phase is the 855MeV 90 turn RTM3. MAMI-B provides a beam of up to $100\mu\text{A}$ with resolution of 60 keV. After being extracted from MAMI-B the electrons are steered through a number of dipole steering and quadrupole focussing elements into the A2 experimental hall. This transport system is designed to ensure that there is no increase in the divergence of the electron beam between the microtron and the Bremsstrahlung radiator.

2.2 Photon Production and Tagging

2.2.1 Photon Production

The photons are produced by the Bremsstrahlung process in the tagging system by passing the extracted electron beam through a thin foil radiator. The choice of radiator requires a balance between the desire for high photon flux and high tagging efficiency (see sections 2.2.3 and 2.2.4). Multiple scattering results in a divergence of the beam and hence a reduction in the fraction of photons which reach the target. Both multiple scattering and the photon flux depend on the thickness of the radiator in radiation lengths, making high Z radiators unattractive as the thin foils required are difficult to handle. However, low Z materials give larger Møller scattering contributions, which effectively reduce the tagging efficiency. In the following experiments a $4\mu\text{m}$, 3×10^{-4} radiation lengths, nickel foil radiator was used.

2.2.2 The TAGGER

The Tagging Spectrometer

The design of the tagging spectrometer and focal plane detector is based on the needs of the planned experiments. As a wide range of photonuclear experiments are planned at MAMI-B, it was decided to cover as wide an energy range as possible at one magnet setting. The spectrometer covers electron energies from 40 to 790MeV [66], covering the single and double pion production thresholds as well as the eta meson production threshold.

There are also a number of practical considerations in the spectrometer design. The spectrometer must have a large enough acceptance angle to ensure that most of the residual electrons reach the focal plane. A fairly straight focal plane to simplify the construction of the focal plane detector and good vertical focussing to minimise the pole gap required are also desirable. Finally, a compact design minimises the collimation required to produce a small beam spot on the target.

Calculations [66] indicated a QD magnet system is most appropriate for this application, the design is shown in figure 2.3. The quadrupole provides extra vertical focussing and the large 'C' type dipole magnet bends the residual electrons round to the approximately straight focal plane. It also acts to direct the main beam to the beam dump in the Faraday Cup. The spectrometer tags electrons of energies 40-790MeV with an intrinsic resolution of order 120 keV over the entire range.

The Focal Plane Detector

It would be complicated and expensive to construct a focal plane detector of similar resolution to that of the spectrometer, and unlikely that such good resolution would be required except over restricted regions of the focal plane. Therefore for the present round of experiments a focal plane detector of 352 overlapping plastic scintillator elements covering the whole accessible length of the focal plane was constructed [67]. This results in an electron energy acceptance of 40-790MeV with ~ 2 MeV resolution. The design allows for adding more elements to reduce this to 1MeV if required.

Each scintillator is individually coupled to a lightguide and photomultiplier tube which is connected to printed circuit boards containing a voltage divider, discriminator and a coincidence unit. The output signal is derived from a coincidence between neighbouring elements to reduce background. The signals are recorded by scalers, and by TDCs and pattern units which are gated by the trigger of the main experiment. To simplify data analysis each channel is recorded separately in high density computer controlled FASTBUS units.

The focal plane detector has its own data handling electronics controlled by a VME computer system. This can be used on its own or controlled by the acquisition system of the main experiment. As well as recording hits in the focal plane the TAGGER produces a logic signal to provide a coincidence between an electron in the focal plane and a photoreaction product.

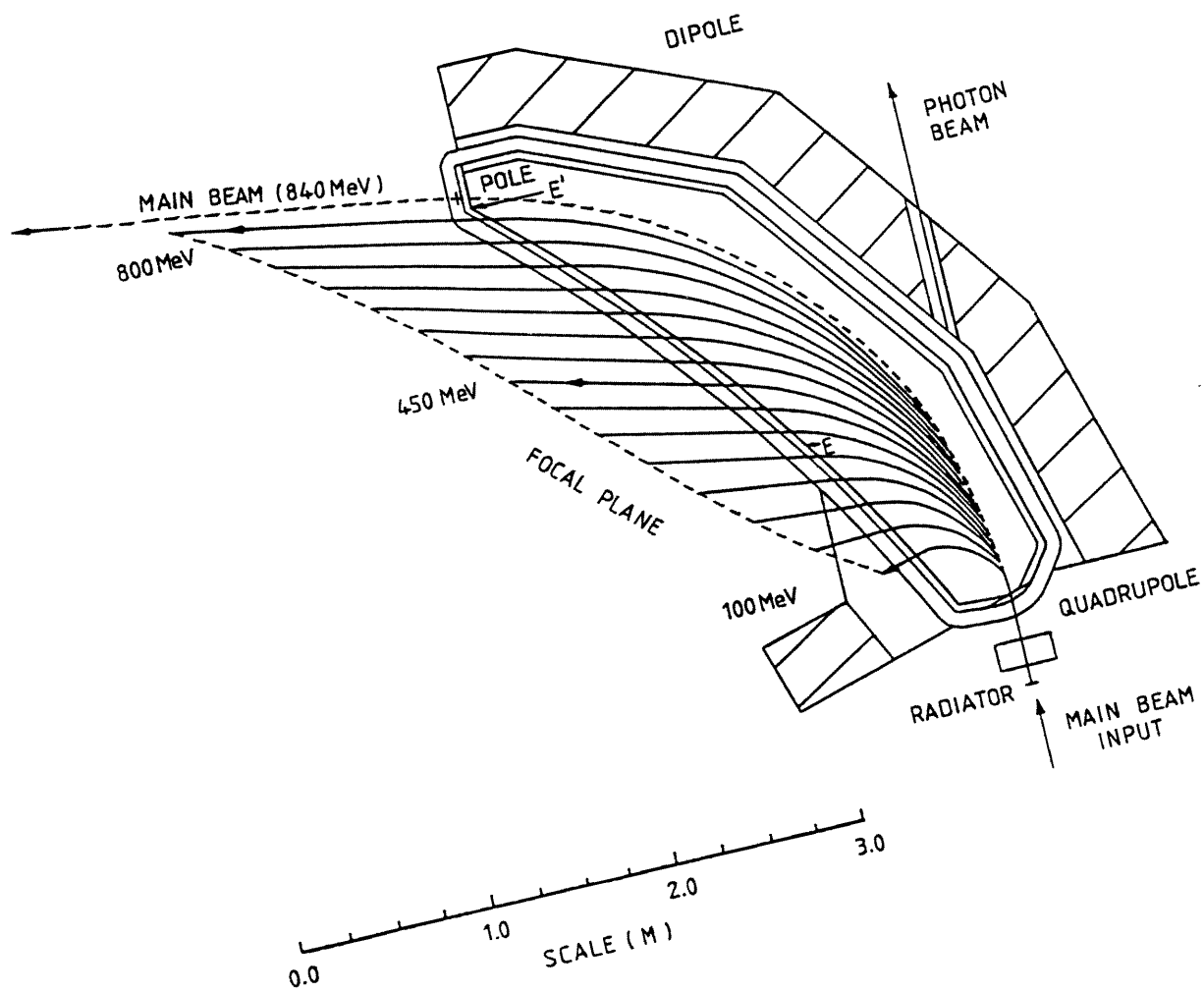


Figure 2.3: The tagging spectrometer

2.2.3 Photon Collimation

The Bethe-Heitler formula [68] shows that Bremsstrahlung is produced in a cone of semi-angle $\sim \frac{m_0 c^2}{T + m_0 c^2}$, where m_0 is the rest mass of the electron and T its kinetic energy, and therefore for high energy electrons the photon beam is strongly forward peaked. However, the radiator-target distance is several metres and the photon beam must be collimated both to ensure a small beam spot on target and to allow detectors to be positioned near to the beam line. The small beam spot is desirable as it minimises the error in estimating the reaction point, and hence the error in particle trajectory.

In these experiments a 5cm long lead collimator with 5mm diameter was placed 250cm from the radiator. There was a similar secondary collimator a few centimeters downstream to remove most of the electrons and positrons produced in the first collimator. A third lead collimator with 30mm diameter was placed approximately 7m downstream of the radiator (near the target) to stop charged particles produced in the collimator reaching the ΔE detectors near the beam. The beam spot had a 15mm diameter on the target, resulting in a contribution of $\sim 1^\circ$ to the uncertainty in emitted particle angle deduced from the hit position in the particle detectors.

2.2.4 Tagging Efficiency

The tagging efficiency, ϵ_t , is a measure of the fraction of the electrons reaching the focal plane detector having a corresponding photon which reaches the target, and is always less than 1 as the collimator removes some photons. In the following experiments it is measured by counting the coincidences between a Pb glass detector in the photon beam and electrons in the TAGGER. The Pb glass detector is placed well downstream of the target and can be moved into the photon beam by remote control, its position in the experimental hall is shown schematically figure 2.4. It has dimensions 25cm \times 25cm \times 25cm. At 30 radiation lengths this is large enough to ensure it is very close to 100% efficient at detecting photons over the entire TAGGER energy range. The tagging efficiency is obtained from the expression

$$\epsilon_t = \frac{\text{Pb glass to tagger coincidence rate}}{\text{singles rate in ladder - singles rate in ladder without radiator}} \quad (2.1)$$

A test showed that the background singles rate in the ladder without the radiator was effectively zero, and could therefore be ignored.

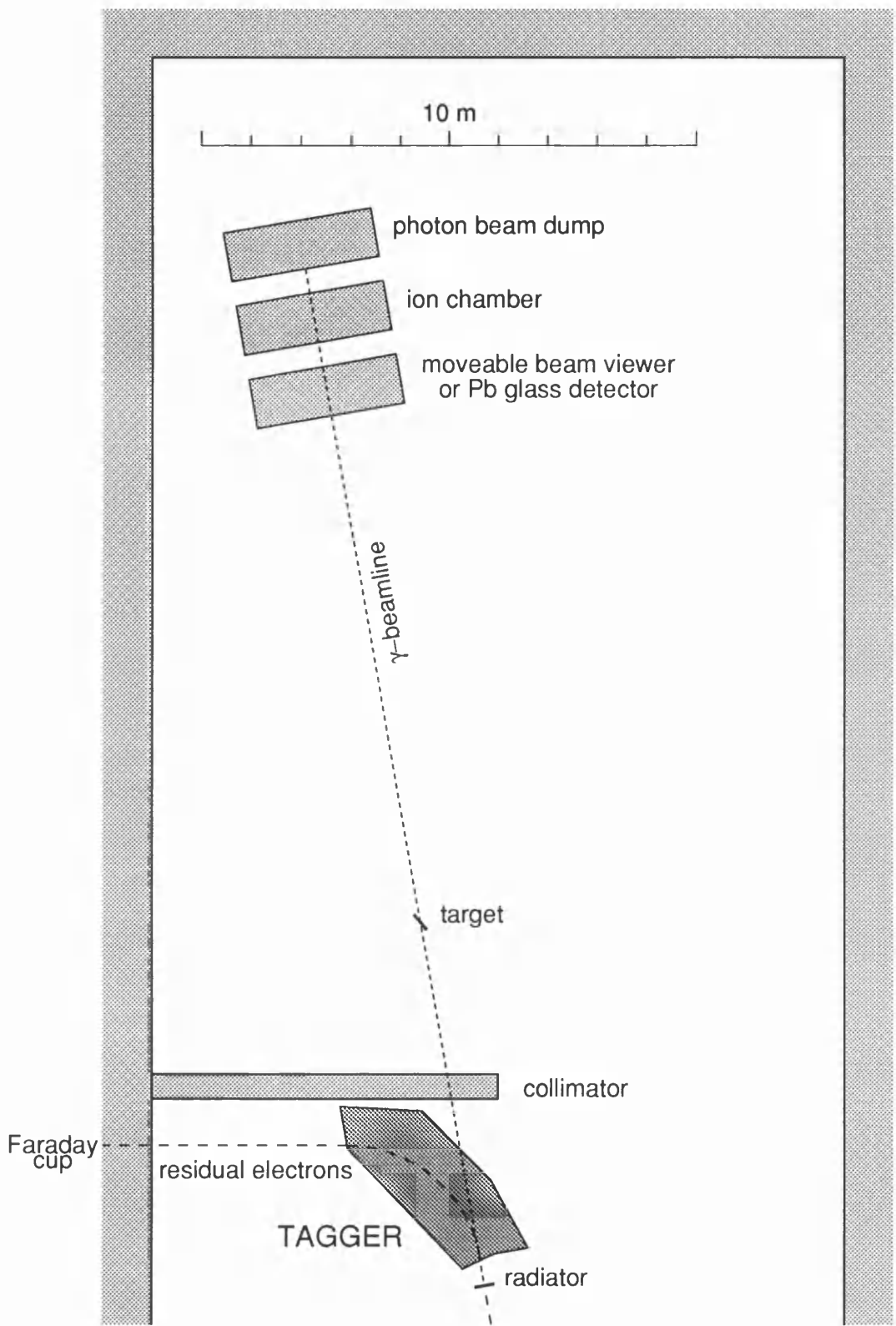


Figure 2.4: *Schematic view of the photon beam line*

Tagging efficiency measurements were made periodically, ϵ_t being measured at $\sim 45\%$. These measurements must be performed at low electron beam flux to ensure that the Pb glass can count every photon. To obtain an on-line indication of tagging efficiency variations the ratio of current in an ion chamber permanently positioned in the photon beam downstream of the target to the electron rate in the focal plane was continuously monitored (figure 2.4). If this ratio decreases it shows that the beam has drifted from its properly aligned position thus reducing tagging efficiency.

2.2.5 Photon Beam Viewer

It is vital to ensure that the electron beam points along the collimator axis as this produces the maximum tagging efficiency and stability. In this condition the photon beam will be properly aligned along the designed beam line, and therefore that the beam will hit the centre of the target and miss the apparatus close to it. For the experiments at MAMI-B an on-line monitor has been developed. It has the advantage of allowing immediate view of the beam at any time without interrupting the measurement.

During experiments the photon beam viewer is permanently mounted in front of the ion chamber well downstream of the target area (figure 2.4). It consists of a BC430 plastic scintillator screen viewed via a mirror by a high sensitivity camera which includes an image intensifier. The resulting image can be viewed in the Control Room where there is an intelligent framestore allowing the image to be averaged over many frames. This improves the picture quality for low intensity beams. The screen is carefully aligned on the collimator axis and has reference marks to indicate the correct photon beam position and the beam diameter.

2.3 Targets

Several thin targets were used. Most of the beam time was needed to study photoreactions in carbon-12 and lithium-6, with shorter periods being set aside for calcium-40 and lithium-7 to provide preliminary data for the design of future experiments. The data analysed in this thesis were obtained using CD_2 and graphite targets. Since the detectors overdetermine deuterium kinematics the CD_2 data allows independent energy calibration of the two particle detectors used. CD_2 is an attractive source of deuterium as it is solid and easy to handle,

and the carbon background may be subtracted if required. Tagging efficiency and target out runs were also carried out. The target out runs were required for background subtractions, as some events result from interactions in the air around the target.

Most theoretical work in this field has been done for ^{16}O whose doubly closed shell structure simplifies the calculations. ^{12}C , in the form of graphite sheets, was chosen as a target in this experiment because its shell structure is sufficiently similar to that of oxygen for comparison. It is a light nucleus reducing the importance of final state effects. In addition there is a wide body of previous experimental work on carbon. From a practical point of view, the elemental form, graphite, is readily available and is rigid and inert, and therefore can be formed into thin targets without the need for additional support or containment.

The targets were mounted on a remotely controlled target ladder, which ensured that the target height and angle were easily reproducible. The target must be set at some angle to the beam to ensure that it intercepts all of the photons. This angle is a compromise between the large charged particle energy losses at angles close to 90° and the large photon beam spot on the target, resulting in a loss of angular resolution, at angles close to 0° . An angle of 30° was chosen. Initial tests using a CD_2 target showed that at this angle a 2mm thickness was sufficient to give reasonable counting rates at moderate photon flux without losing energy resolution. Calculations indicate that a 50MeV proton will lose approximately 3MeV in 2mm of CD_2 , causing a 1.5MeV uncertainty in its reconstruction, similar to that of the TAGGER. The other targets had similar surface densities.

2.4 Particle detector requirements

In order to fully explore the kinematics of (γ, NN) and $(\gamma, \pi N)$ interactions particle detectors with the following properties are required.

- Particle discrimination

The various reaction products (p, n, π, d) must be distinguishable both from each other and from the large atomic background (γ, e).

- Energy range and resolution

To study reactions around photon energies of 50-500MeV particle energies of typically 25 - 250MeV must be measured. It is helpful in the study of the reaction mechanism if the resolution is sufficient to determine the nucleon's

initial shells. This means that a resolution of less than 5MeV is desirable in each particle detector.

- Angular range and resolution

It is only by measuring reactions over as large a phase space as possible that detailed investigations of the various mechanisms can be achieved. Good resolution, typically less than 5° , is required to observe effects due to features in the nucleon momentum distributions.

- Neutron detection

In order to make the best use of the beam time reasonably high neutron detection efficiencies are required. Furthermore, to explore fully those reactions emitting neutrons, detectors which can measure the neutron's energy and trajectory accurately are required.

- Large solid angle

Since the reaction cross-sections in photonuclear experiments are rather small detectors with large solid-angle are required.

- Fast detector response

At least some part of the detection system should be able to produce a fast event trigger to allow a reasonable photon flux, and hence reduce the proportion of random electrons. This again compensates for the small reaction cross sections.

Two detectors were built to satisfy these requirements. They sit either side of the photon beam, and both have $\sim 1\text{sr}$ solid angle. Their design largely prohibits the study of out-of-plane kinematics, but this should be relatively unimportant as the kinematics of the reactions are such that the photon and ejected nucleons are close to being coplanar, and the acceptances are sufficient to sample the full range of initial Fermi momenta. The detectors are PIP, primarily designed to detect protons and π^+ s, and TOF, to detect the associated particles (n, p, π^\pm). Their positions in the experimental hall are shown in figure 2.5 and their detailed design is described below.

2.4.1 Charged Particle Detectors

There are two widely used methods for performing measurements on charged particles, tracking detectors (such as magnetic spectrometers or multi-wire propor-

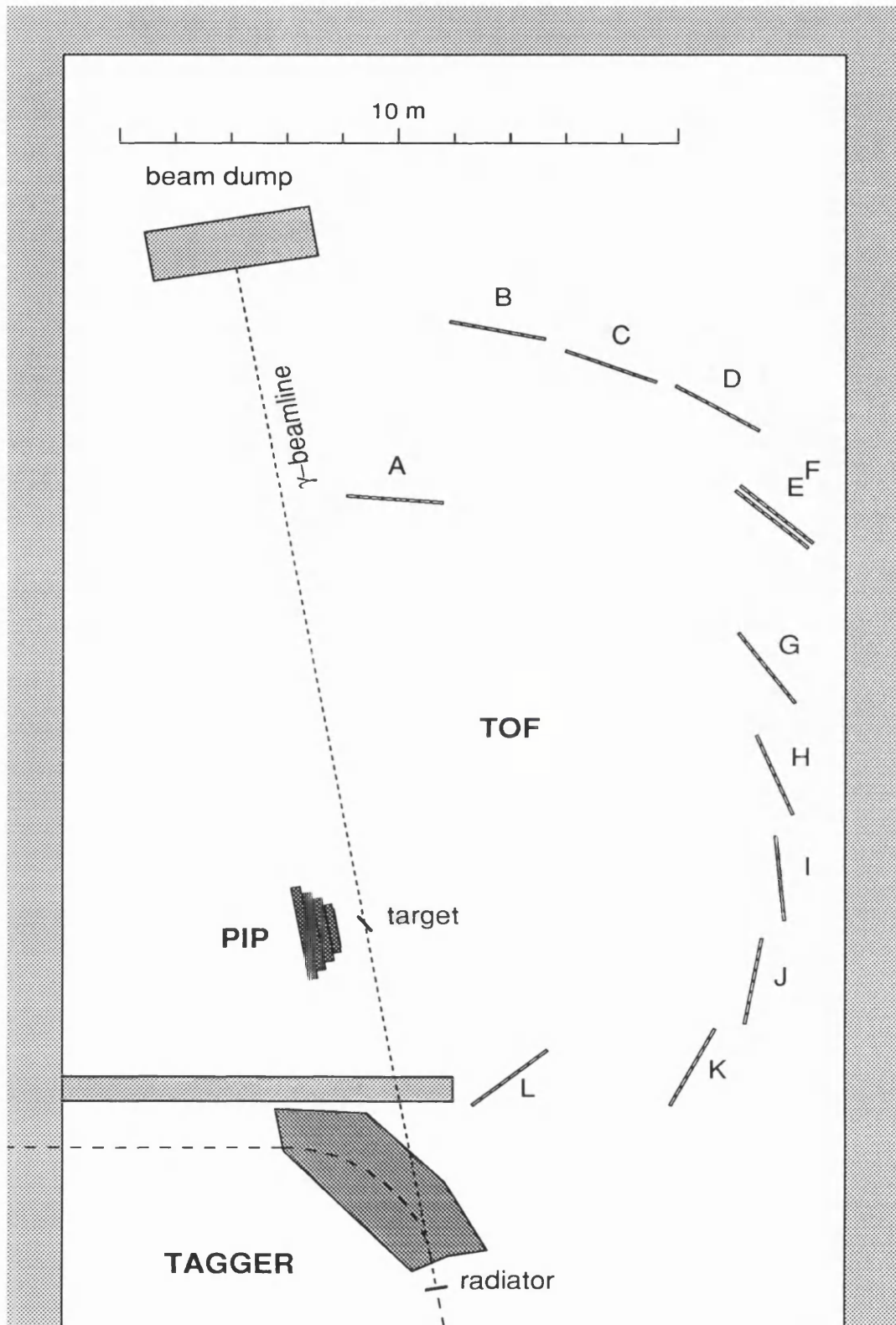


Figure 2.5: *The layout of the A2 experimental hall*

tional counters) and energy loss detectors (such as scintillators or semi-conductor counters).

Magnetic spectrometers measure momenta from the trajectories of charged particles in the magnetic field often using multi-wire proportional counters or drift chambers at the entrance and exit to the field. The polarity of the field selects either positively or negatively charged particles and any further particle identification is made by $E/\Delta E$ measurements. These provide excellent energy and position resolution, but have comparatively small solid-angle and are expensive. Multi-wire proportional counters track charged particles by measuring the charge produced by the passage of the particle through an ionising gas. These have excellent position resolution and are able to cover large solid angles, but are expensive and complicated to construct and use. Energy measurements require an external magnetic field, or another detector.

Energy loss detectors measure particle's energies from the amount of excitation their passage produces, *eg* the light output from scintillators. Plastic scintillator is particularly attractive as it is available in large blocks, is easily formed into different shapes and is relatively inexpensive. It has also an extremely fast response which is attractive for coincidence experiments and can be exploited to give position information via the time difference between the signal at each end of a long block. Again particle identification is made via $E/\Delta E$ measurements.

2.4.2 PIP

PIP is a segmented ΔE - ΔE -E telescope used to detect charged particles and provides the trigger for the experiments (figure 2.6). It is similar to the proton detector used previously by the collaboration [69], with changes being made to allow for the higher particle energies at MAMI-B and to eliminate problems encountered in the previous detector. The segmented design maximises the light collection efficiency improving position and energy resolution, and it also helps in identifying and treating events in which a large amount of energy is deposited in one block after a particle undergoes a nuclear interaction in the scintillator. The detector has been designed to achieve proton energy resolutions of the order ~ 2 -3MeV at 50MeV incident energies. It has 4 E layers and two ΔE layers, the first of which is curved round the target providing the start time for the reaction.

The scintillator itself cannot distinguish between π^+ s and π^- s. Although reactions involving both of these are of interest only π^+ s can be readily identified

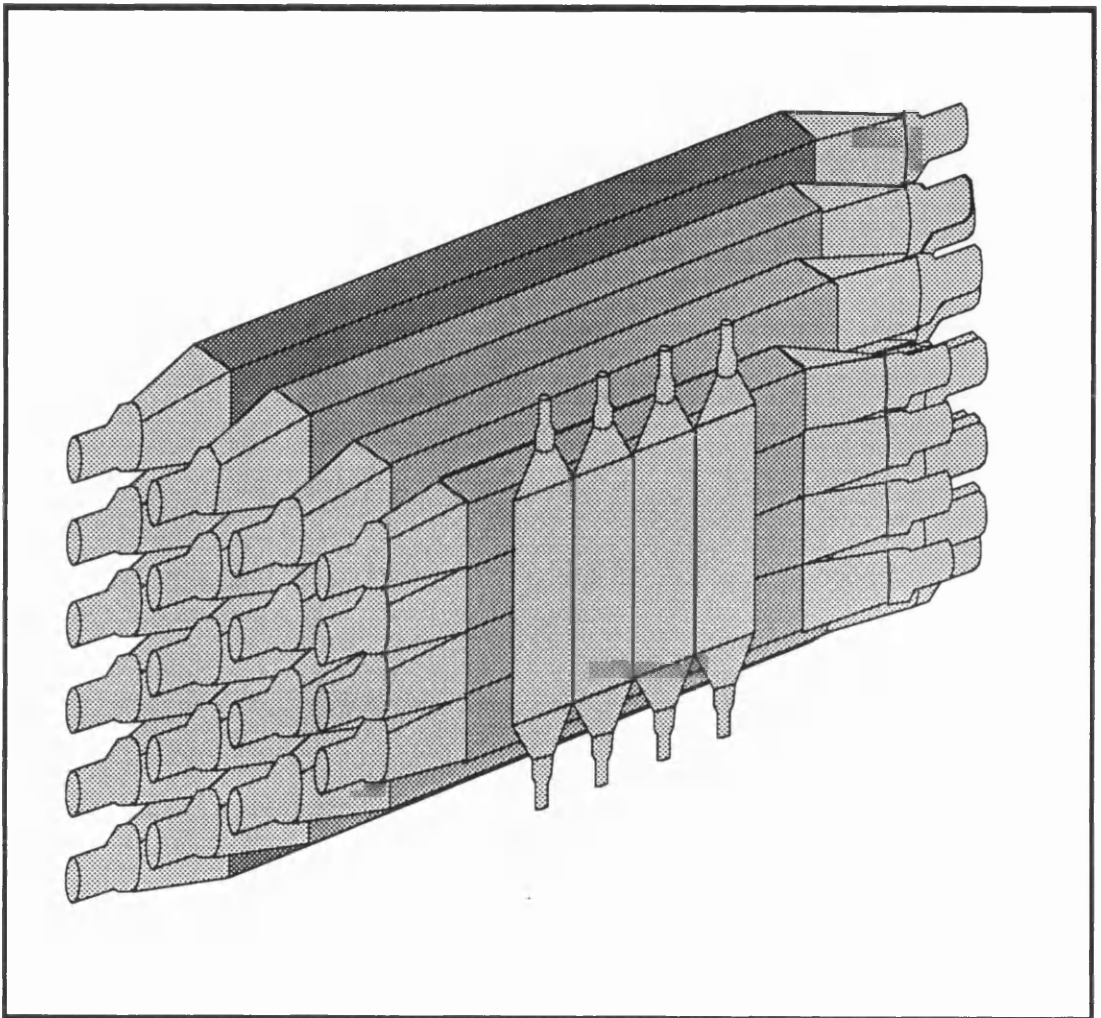


Figure 2.6: A schematic diagram of PIP

by the afterpulses produced during their subsequent decay $\pi^+ \rightarrow \mu^+ \rightarrow e^+$. Pions whose decays are not detected are rejected.

The Start Detector

The first layer is a thin transmission detector of dimensions 150mm \times 100mm \times 1mm thick curved in an arc of radius 80mm (figure 2.7). It is separate from the main detector and is placed with the centre of the target at its centre of curvature. This detector provides a reference ‘start time’ signal for all the electronic signals recorded in each event. As the signals from this detector are used primarily for timing the 1mm thickness gives sufficient light output without seriously degrading the particles’ energies. The thickness is also sufficient to give additional information for particle identification. Its surface area is chosen so that when carefully aligned it does not limit the solid angle of PIP.

A curved design was chosen as this minimises the variation in path length from the target to the detector and hence maintains optimum on-line timing resolution. This design is also attractive for covering PIP at a range of positions, as it can simply be rotated around a vertical axis to cover different angles.

The detector consists of a curved piece of scintillator in a perspex frame which gives additional structural strength and is used to attach it to the lightguides. This whole structure is mounted in an aluminium stand designed to hold it rigidly in position while ensuring that both stand and detector are kept well away from the beam and cannot cause background.

ΔE_2

The second ΔE transmission layer consists of 4 strips of scintillator of dimensions 200mm \times 420mm \times 2mm mounted vertically at the front of PIP (figure 2.6). It is this layer which defines the solid-angle, ~ 1 sr at the design position of 50cm from the target. All subsequent layers subtend slightly larger solid-angle to ensure no particles are lost via multiple scattering.

The ΔE_2 layer is used for particle identification via E- ΔE measurements, and provides the vertical position of a hit from time difference measurements. The 2mm thickness is sufficient to give useful signals without seriously degrading the particles’ energies before they enter the main body of the detector. The 42cm \times 20cm surface area gives reasonable solid-angle from the four elements and is about the maximum practical size before the ‘droop’ in light collection from one

end of the detector to the other because unmanageable.

Two E Layers

The main volume of PIP consists of 4 layers E1-E4 of horizontal blocks. Their dimensions are 10 cm x 10 cm x 10 cm. The detector is designed to detect particles with energies up to 10 MeV. The detector is made of plastic scintillators. The detector is made of plastic scintillators. The detector is made of plastic scintillators.



The cross-section of the detector is shown in Figure 2.7. The detector is made of plastic scintillators. The detector is made of plastic scintillators. The detector is made of plastic scintillators.

The detector is made of plastic scintillators. The detector is made of plastic scintillators. The detector is made of plastic scintillators.

Figure 2.7: The Start Detector

end of the element to the other becomes unmanageable.

The E Layers

The main volume of PIP consists of 4 layers E1-E4 of horizontal blocks. Their dimensions are given in the table below. These layers measure particle energies from the scintillator pulse heights and are used in $E-\Delta E$ measurements for particle identification. The E1 layer provides the horizontal position of a hit on the detector.

layer	no of blocks	dimensions L × D × H (cm)
E1	4	100 × 11.0 × 13.5
E2	4	130 × 17.5 × 17.5
E3	5	160 × 17.5 × 17.5
E4	6	190 × 17.5 × 17.5

Table 2.1: *Dimensions of the PIP E blocks*

The cross sections of the blocks were chosen to roughly match the cathode area of the photomultiplier tubes used since this provides the best light collection and hence resolution. The photomultiplier tubes used were 130mm in diameter which is the largest readily available. The E block lengths were chosen to give large solid-angle without losing resolution due to long path lengths in the target and ΔE s. The E1 layer covers an angle of $\sim 77^\circ$ in the horizontal plane, and can be used to cover angles from 22° to 158° in three positions. The angular acceptance is $\sim 44^\circ$ in the vertical plane. The E1 and E2 layers will stop protons of energy up to 250MeV at extreme angles, and all 4 layers will stop pions of up to 200MeV. At higher proton energies inelastic collisions and nuclear processes become dominant [70] and may affect the energy deposited too seriously for the detector to yield useful results. Therefore, in the present work only the first 2 layers are used for proton detection. For the E3 and E4 layers to be used in future work this effect must be investigated and accounted for using computer simulations of the detector.

Detector Construction

The ΔE_1 detector is constructed of NE102A plastic scintillator and the ΔE_2 layer NE110, they are both coupled to perspex twisted-strip lightguides with optical cement to ensure a permanent transparent join. NE102A has high light output and reasonably long attenuation length [71] which is required to give large enough signals in the very thin layer used. However, NE110 is used in the second layer as the marginally lower light output is compensated for by the considerably longer attenuation length [71]. The twisted-strip lightguides are essential to transmit light from the rectangular scintillator to the circular faces of the photomultiplier tubes. As the timing from the start detector is important, each strip was the same length to provide equal path lengths and these maintain good time resolution. In the ΔE_2 layer the strips had slightly different lengths, but this did not greatly spread the times. The lightguides are coupled to the photomultiplier tubes with silicone rubber. This bond is transparent to the scintillation light, but may be broken if required. The ΔE_2 layer used 50mm diameter EMI 9954KB tubes and the start detector 50mm diameter Phillips XP2262 which have better timing characteristics.

Each detector and lightguide is highly polished to ensure maximum light transmission via internal reflection. They are individually wrapped first in Al foil which easily covers the awkward shapes of these detectors and their lightguides and is a light material, and then black tape and card to ensure that the detectors are light tight. These wrappings were kept as thin as possible to minimise particle energy losses. A proton of 100MeV typically loses 5MeV in the target, wrappings and ΔE 's on its way to the E1 layer.

The E blocks are made of NE110 plastic scintillator. Each end is coupled to solid perspex lightguides with optical cement. These lightguides reduce the variation in light collection times close to the ends. This is important as the hit position is obtained from the time difference of the signals at each end of a block and thus any non-uniformity in the light collection will affect the measured position. The lightguides are coupled to 130mm diameter EMI 9823KB photomultiplier tubes with silicone rubber, again allowing removal if required.

Each scintillator element is highly polished to aid internal reflection and is wrapped individually to ensure that there is no cross-talk between elements. The E1 and E2 layers are wrapped in 1 layer of matt black card to minimise the wrapping thickness and hence particle thresholds. For such blocks a reflective

wrapping does not improve light collection as most of the light is transmitted via total internal reflection. The E3 and E4 layers were wrapped in several layers of Al foil and black polythene.

The ΔE_2 layer and each of the E layers are permanently mounted in modular fashion in separate aluminium stands. These stands are then mounted in a large steel frame which keeps them rigid and properly aligned with respect to each other. The frame is partially enclosed by steel plates to provide an electromagnetic shield, additional light proofing and heat stability for the photomultiplier tubes as well as additional structural strength. The electronics required for read-out is mounted on the back of the frame. This means that the cables from the detector to the electronics are permanently attached and the whole system can be moved into position near the target quickly and easily.

2.4.3 The TOF Array

The most important property of the associated detector is its ability to detect neutrons. As these are uncharged they must be detected by secondary processes, most commonly by the signal produced by recoil protons. Plastic scintillator is an attractive material for this application as it has a high density of hydrogen atoms, and therefore effectively unbound protons. It is then necessary to discriminate between neutrons, photons and charged protons and pions (neutral pions will decay in the target). This is achieved by using a thin scintillation detector near the target to identify the charged particles and time-of-flight information to distinguish between neutrons and photons. The detection of the knockout protons gives only a lower limit to the neutron's energy which is normally found by time-of-flight measurements. These detectors therefore require long flight paths to provide good energy resolution, and enough thickness to provide a reasonable neutron detection efficiency without losing that resolution. As it is impossible to determine the depth of the interaction within the scintillator the length of the flight path has an uncertainty equal to half the thickness of the plastic.

Time of flight detectors similarly provide information about charged particles, protons and pions being distinguished by E- ΔE measurements. Again π^+ s and π^- s cannot be distinguished, but below the double pion production threshold their charge can normally be deduced from the other particle detected in the reactions studied here. As PIP is used to detect positively charged particles most pions detected in TOF will be π^- s.

The TOF array consists of 96 20cm×5cm×300cm plastic scintillator bars mounted vertically in groups of 8 on up to 12 separate stands. This design is similar to the long neutron detectors used in previous experiments [72] and is highly flexible, allowing the detectors to be placed in different configurations for different experiments. It is possible to put up to 4 layers of detectors on each stand to improve neutron detection efficiency and increase the stopping power for charged particles; two layers (E and F) were put on one stand to test this during the present experiments. The positions of the TOF detectors in the present work are shown in figure 2.5 (10 stands of 8 detectors and 1 of 16). This arrangement ensures that the flight paths are set for roughly constant neutron energy resolution at all angles.

The Design of the TOF Detector

The geometry of the bars in the TOF detector was chosen to make best use of the space available and to provide resolution at least matching that of the TAGGER and PIP. A vertical orientation was chosen for easy handling of the detectors. The 3m length of the bars is limited both by the height of the A2 experimental hall and by the self-attenuation of light in the scintillator. The pulse height information is recorded as it is helpful in discriminating between different types of charged and neutral particles, and also allows the threshold to be set by software during the analysis. The thickness of the detector limits the neutron energy resolution, the 5cm thickness chosen results in a transit time of about 400ps for 100MeV neutrons, which should be no poorer than the timing resolution of the TAGGER. However, this thin design limits the efficiency for detecting neutrons to about 5% and also limits the energy range of stopped charged particles, but these limits can be improved by simply placing more than one layer of detectors on each stand.

TOF also provides accurate angular information, horizontally from the position of the bar hit and vertically from the time difference between signals from each end of a bar. The 20cm width gives angular resolution of better than 3° for all flight paths longer than 4m.

Detector Construction

The TOF detectors are made of NE110 plastic scintillator, chosen because of its long attenuation length, which is again highly polished to maintain total internal reflection. Each bar is coupled top and bottom to solid perspex lightguides

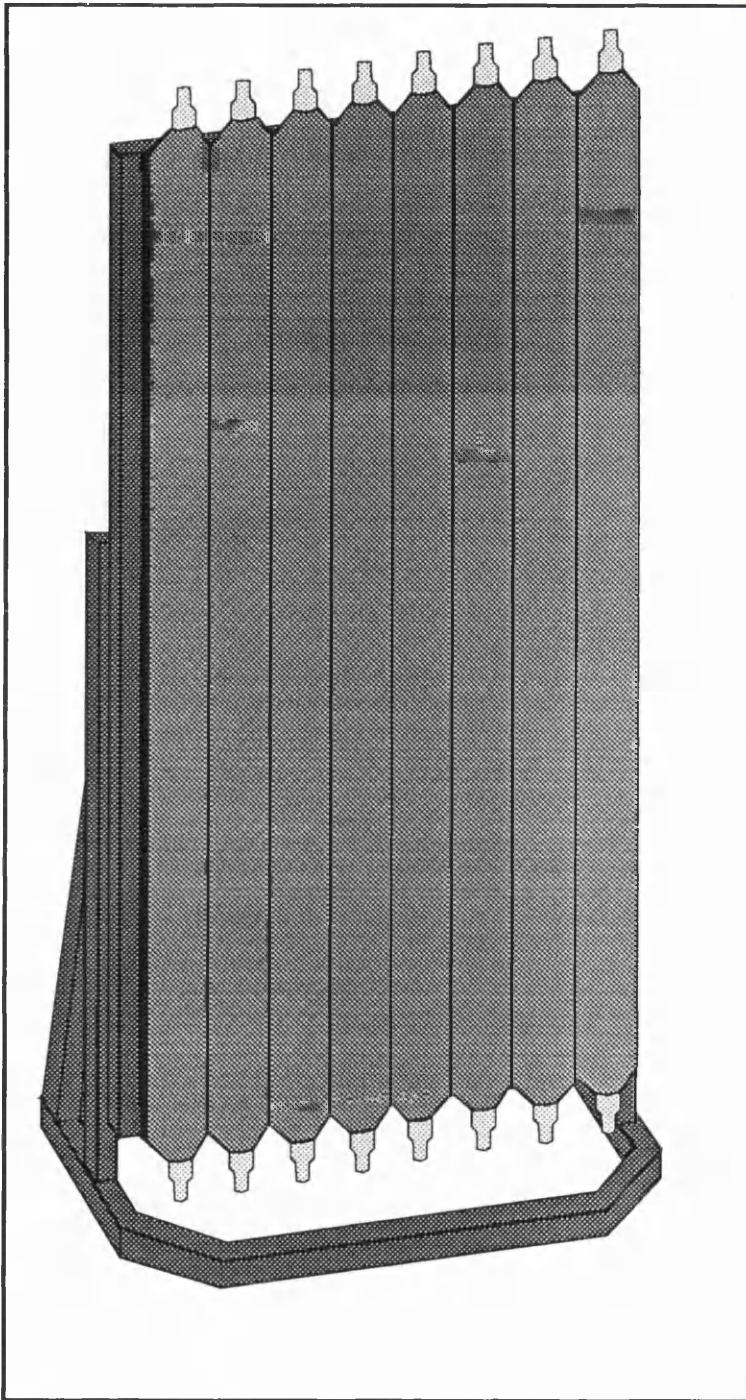


Figure 2.8: *Schematic diagram of a TOF stand*

with optical cement. They are then coupled to 72mm diameter Phillips XP2312 photomultiplier tubes with silicone rubber. These are of considerably smaller cross section than the bars, but the resulting loss of collected light and thus pulse height resolution is small [73], and the smaller size is convenient for lightguide design. The bars are individually wrapped in Al foil and ~ 3 mm thick neoprene rubber to ensure a robust light proofing, the Al foil ensuring that neoprene does not stick to the scintillator losing internal reflection. These wrappings are thicker than those on PIP, but this thickness is small in comparison with the air along the 4 - 12m flight paths.

TOF ΔE

A segmented ΔE detector is used with TOF to discriminate between charged and neutral particles. The segmented design was chosen to ease the analysis of multiple hits in the array and to ensure that the response was not dominated by the highly forward peaked electromagnetic background. The design is shown in figure 2.9. As this is a prototype detector, it was limited to 3 segments with lengths as shown, the size of each segment is roughly inversely proportional to the count-rate at the angles it covers. All elements are 10cm high and 2mm thick to ensure that all charged particles leave a detectable signal. The detector is mounted 10cm from the target where it covers all of the TOF array.

The detector is constructed from NE102A plastic scintillator coupled top and bottom to perspex lightguides on which are mounted Valvo 50mm diameter XP2252 photomultiplier tubes. Each element is wrapped individually with Al foil and polythene, and then mounted in an aluminium stand to hold them rigidly in the correct position. The stand is designed so that it is kept safely out of the beam to avoid creating background.

2.5 Electronics and Data Acquisition

Electronic circuitry is required to convert the raw signals from the detectors into digital words containing pulse height and time information. These can then be stored on magnetic tape before being translated into physical energies and momenta during the analysis. In order to do this efficiently hardware decisions must be made to reliably identify a 'true' event, and hence minimise overheads in processing and storing too much of the 'random' background. These decisions

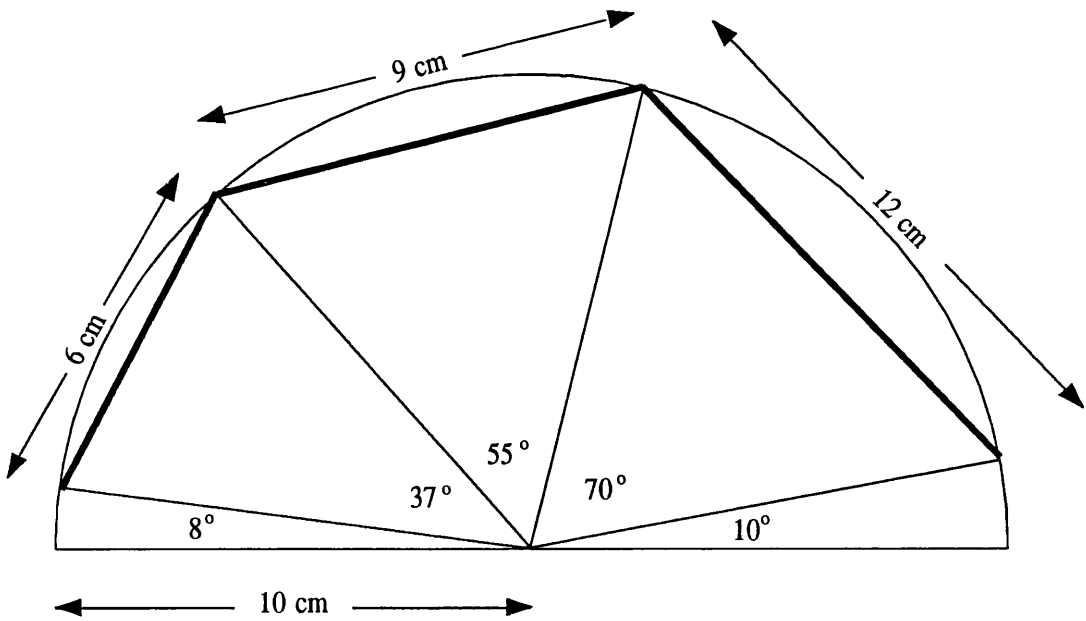


Figure 2.9: Segmentation of the TOF ΔE

are made by the trigger logic circuit described below which looks for events in which a charged particle is detected in PIP in coincidence with an event in the TAGGER. This trigger initiates the readout of PIP, TOF and the TAGGER. A schematic diagram of PIP's circuit is shown in figure 2.10, the circuit for the E2-E4 blocks and TOF bars are similar to that of the E1 blocks.

In the experiments 3 linked bus systems were used; VME-bus [77], FASTBUS [78] and CAMAC [79], as well as the more conventional NIM modules. FASTBUS ADCs (either charge- or time-to-digital convertors) were chosen for their fast timing, high resolution and high channel density. FASTBUS scalers were also used. The ADCs have programmable upper and lower thresholds to allow on-line data filtering, and MEGABLOCK readout facility allowing a number of units to be treated as a single module thus reducing readout overheads. CAMAC was used to provide high density programmable logic and control modules. This, for example, allows the thresholds of the discriminators to be set remotely, and should in future allow remote changing of triggers. The other logic modules such as gates and latches were NIM. The VME system was used to control the other bus systems and readout the data. It consists of a MC68030 based Eltec E6 single board computer running an OS9 operating system. The software for this was written at the Kelvin Lab. The CAMAC crates are daisy chained together and linked to the VME by a CBD8208 CAMAC branch driver via a standard A2 controller. Each FASTBUS crate is controlled by a LeCroy 1821 segment manager interface configured as a FASTBUS master. This is connected to the VME via a LeCroy 2891A CAMAC register.

2.5.1 Triggers

A simple fast trigger was constructed which identifies charged particles in PIP by demanding a coincidence between the start detector and an element in the ΔE_2 layer. The trigger sets a latch to prevent further events from being accepted until the present event has been dealt with. It also initiates the fast clear process. This fast trigger requirement was subsequently augmented by demanding that an element in the E1 layer fired and that the trigger from the TAGGER was present, thus insisting on a (γ, X) event. If the latter conditions were not met the event was rejected via the fast clear inputs. An outline of this circuit is included in figure 2.10. This provided the main trigger used. However, a number of other logic circuits were employed to provide more stringent tests, or in parallel to

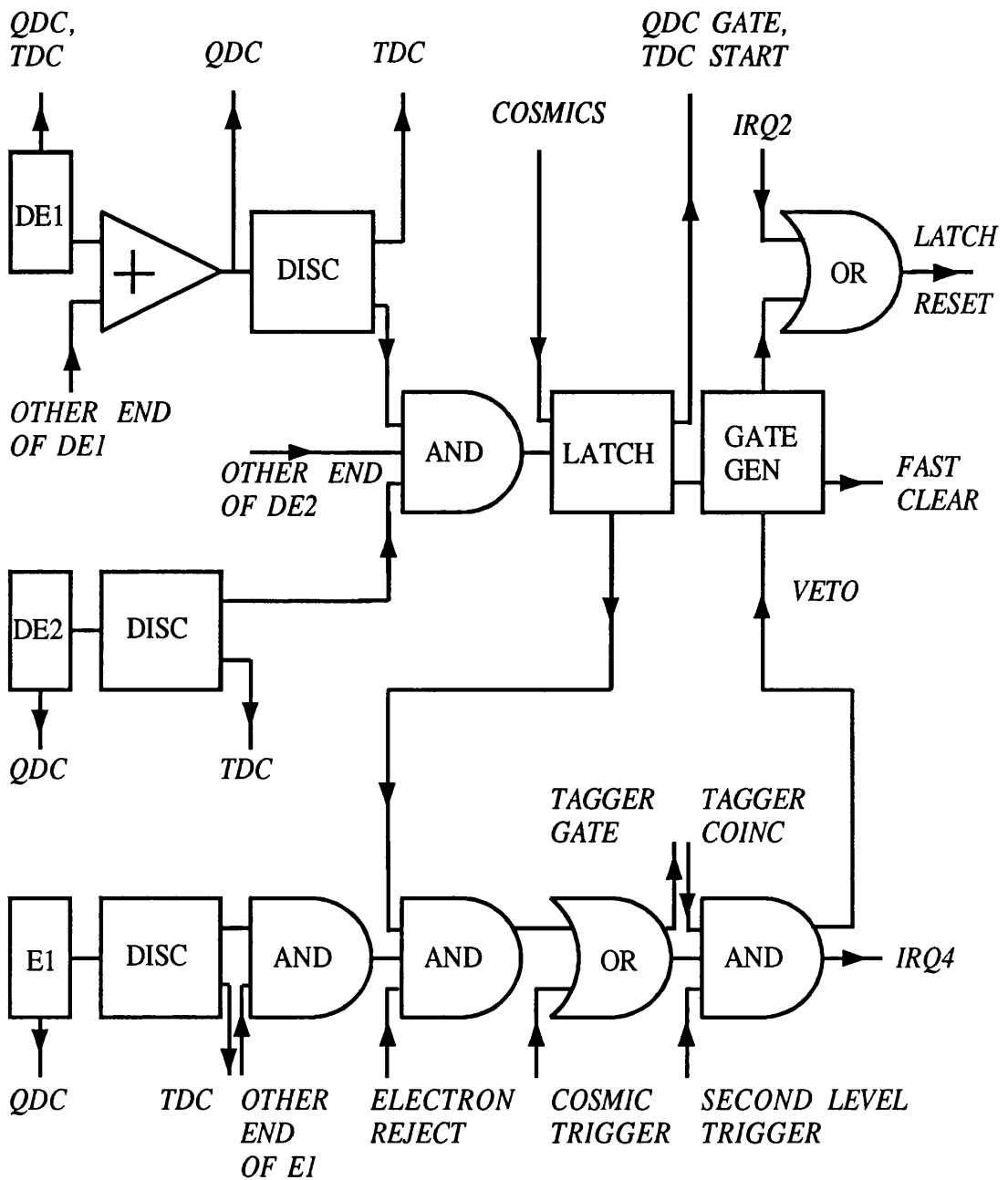


Figure 2.10: Schematic diagram of the electronics circuit

accept other types of events. These are described below.

Electron reject circuit

The largest component of background in PIP comes from the electrons produced in Compton scattering of the photon beam and e^\pm from pair production. As electrons have very low stopping powers this background can be greatly reduced on-line by making a diagonal cut in a E - ΔE plots of signals from the E_1 and ΔE_2 or ΔE_1 layers of PIP. The cut is achieved by means of a discriminator set on the analogue sum of pulses from the ΔE signals, the slope and position of the cut being controlled using the separate attenuators on the input signals. Figure 2.11 shows the circuit used to achieve this, and it is used in coincidence with the main trigger shown in figure 2.10. The bypass for events which fire the E2 layer (figure 2.11) is used in order to ensure that no high energy particles, which have low pulse height in both E_1 and the ΔE s, are lost. Later runs used a modified circuit which also rejected events below a diagonal cut from the E - ΔE plot of signals from the E_2 and E_1 layers, signals from the E3 layer now providing the bypass to ensure high energy particles were not lost.

Electrons and most pions entering the detector are minimum ionising and produce similar signals. Thus some low energy pions are also rejected when using PIP in this mode. To avoid this in experiments where PIP is being used to detect pions the electron reject circuit can be either removed or the cut can be made less stringent to accept all pions at the expense of accepting a significant fraction of the electrons. However, most of these electrons can be rejected by incorporating the signal from the pion identification circuit into the second level trigger (see below).

Second level trigger

As (γ, NN) and $(\gamma, \pi N)$ events were being studied, a trigger which insisted on a coincidence with TOF was used for part of the time. This was achieved by insisting that both ends of at least one TOF bar fired. The trigger now required coincidence between PIP, TOF and the TAGGER.

The more stringent coincidence requirement produces a considerable reduction in computer interrupt rate. This provided an opportunity to increase the electron beam current and hence photon flux without introducing excessive computer deadtime. To do this the low E_γ section of the TAGGER had to be switched off

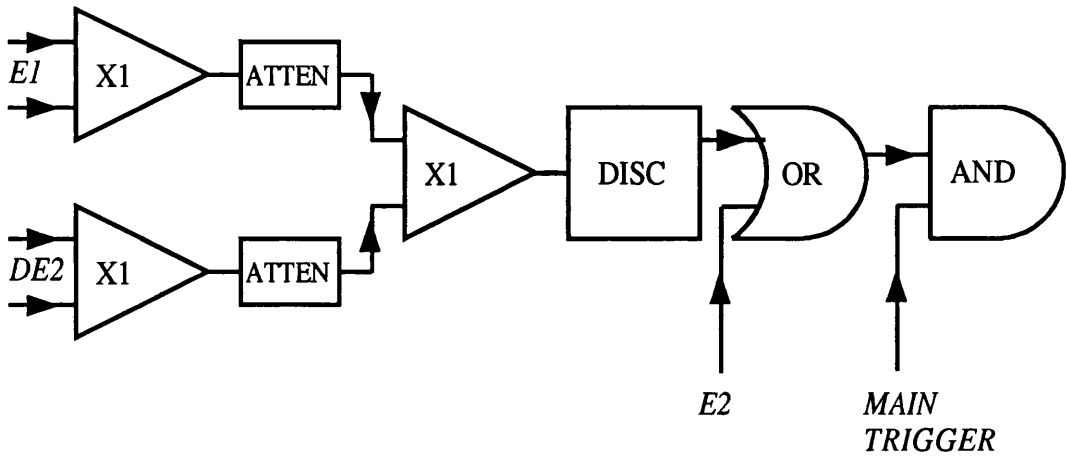


Figure 2.11: *The electron reject circuit*

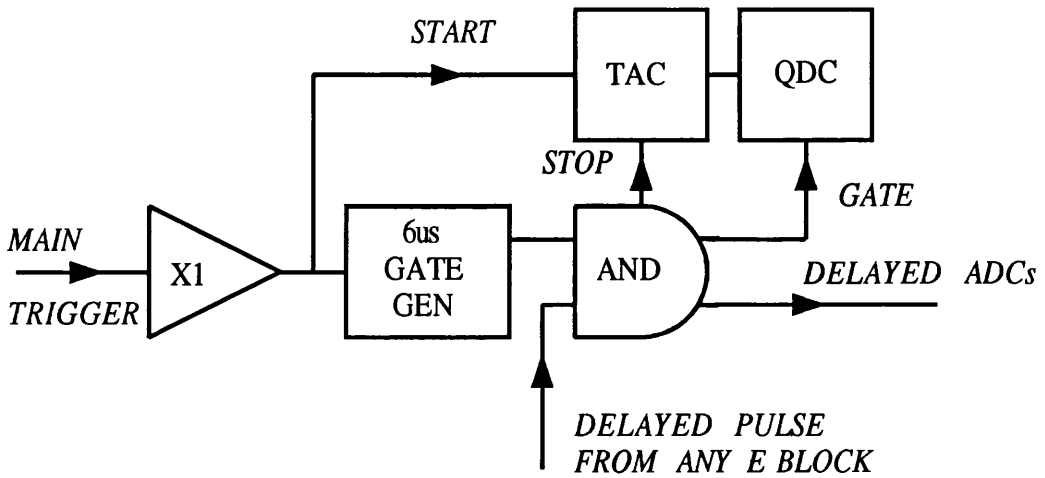


Figure 2.12: *The pion identification circuit*

(*i.e.* E_γ less than 110MeV), as the count rate was too high for the photomultiplier tubes. This was acceptable as sufficient data in this high yield area had already been accumulated in runs where no TOF hit was required.

Pion identification

As pions have low stopping power it is difficult to discriminate between them and electrons using only pulse height information. A more certain method is to look for the delayed pulse caused by the decay chain $\pi^+ \rightarrow \mu^+ \rightarrow e^+$, the latter stage of which has a mean life of $2.2\mu s$. Once the main trigger identifies a charged particle in PIP it starts the pion identification circuit shown in figure 2.12 which looks for the afterpulse of the π^+ decay. A second pulse within $6\mu s$ of the trigger produces the delayed ‘pion trigger’ which provides a gate for a second set of ADCs and TDCs on each block and records the time between the prompt and delayed triggers on the TAC. Initial tests suggest that this method, which has background solely from randoms, accepts only $\sim 30\%$ of particles identified as pions by E- ΔE methods [74]. The rejected events are due to π^- s, which do not trigger this circuit, electron contamination and pions near the outside of the detector whose decay e^+ s escape leaving too little energy in the E blocks. This value of 30% compares reasonably with the optimum value of 42% estimated assuming 50% of the identified particles are π^- s and an 85% probability of the pion decaying within the gate.

Cosmic trigger

The above triggers are all useful in the identification of (γ, NN) and $(\gamma, \pi N)$ events. A second trigger was employed in parallel with the main experiment. This trigger identified cosmic muons passing through PIP by looking for coincidences between the top and bottom blocks (figure 2.13). Such events are detected at a rate of about 25 Hz in PIP and are useful in gain monitoring. This trigger was divided down to ~ 2 Hz during the experiments to minimise the number of ‘real’ events rejected due to dead time effects.

Incorporated into this trigger were events generated by the flasher circuit which is used for gain monitoring in the TOF detectors [75]. This consists of an LED flasher unit of wavelength ~ 650 nm to match the characteristics of both the photomultiplier tube and the PIN diode used in the flasher unit. A flasher pulse is sent to each photomultiplier tube and the light is directed to the photomultiplier

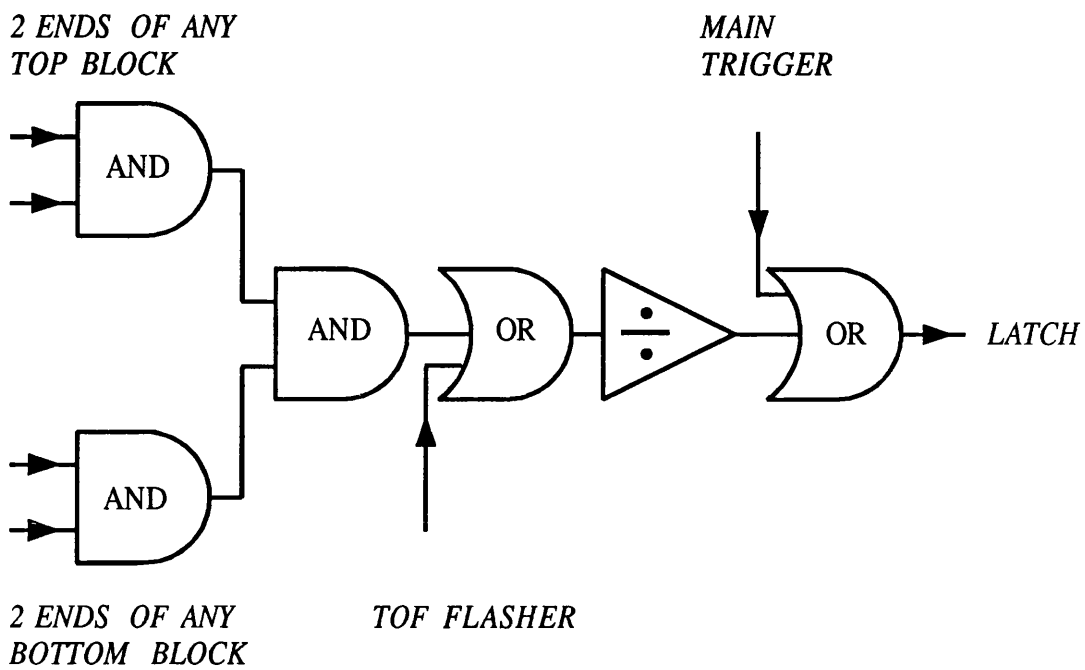


Figure 2.13: *The cosmic trigger*

tube through the light guide.

A signal from the combined circuit was sent to an empty channel in the TAGGER ladder in order to fulfill the tagger coincidence mentioned previously, and to provide identification of cosmic or flasher events.

2.5.2 Data Acquisition

The data acquisition process 'ACQU' [76] was run on a VME-bus microcomputer which was linked via the ethernet to a VAX workstation. The VME-bus system controls the dependent electronics and data transfer. The data are transferred to the workstation which stores it on disk or magnetic tape. The workstation also runs an analysis program which allows the display of data to provide on-line analysis and monitoring.

The VME-bus system runs an OS9 operating system which has 'UNIX-like' commands and directory structure. When the acquisition is started the VME SUPERVISE software module initialises all the hardware as instructed by parameter files and those 'child' processes ('acqu', 'store' and 'hist') that have been requested. It then 'sleeps' until it is required to make a tidy shutdown of the acquisition. Each of the child processes is independent of the others for maximum efficiency, and is controlled by the main process by passing 'events' (intertask communication semaphores). If the VME is being used to control a subordinate VME system (*eg* that of the TAGGER) another child process ('slave') is generated. A schematic diagram of the data processing is shown in figure 2.14.

Signals from the particle detection system are digitised in FASTBUS and CAMAC ADCs and read out on receipt of a trigger signal to a data buffer in the shared memory. The trigger signal is fed on to the IRQ4 VME-bus interrupt line. The latch discussed above was used to gate both the ADCs and scalers, ensuring that a second trigger was not accepted while data was being processed, and was reset by a fast clear or the interrupt routine via the IRQ2 VME-bus interrupt line. When the buffer is full it sends an event signal to the 'store' process which passes the data over the ethernet to the storage and analysis program on the workstation. The data can also be processed by the 'hist' task so that spectra can be displayed on the VME system, but this was rarely used as the process on the workstation is capable of more sophisticated analysis. These child processes run in the background state to allow the user to control the system from the terminal using the program 'control'. This is used to start (and stop) the acquisition by

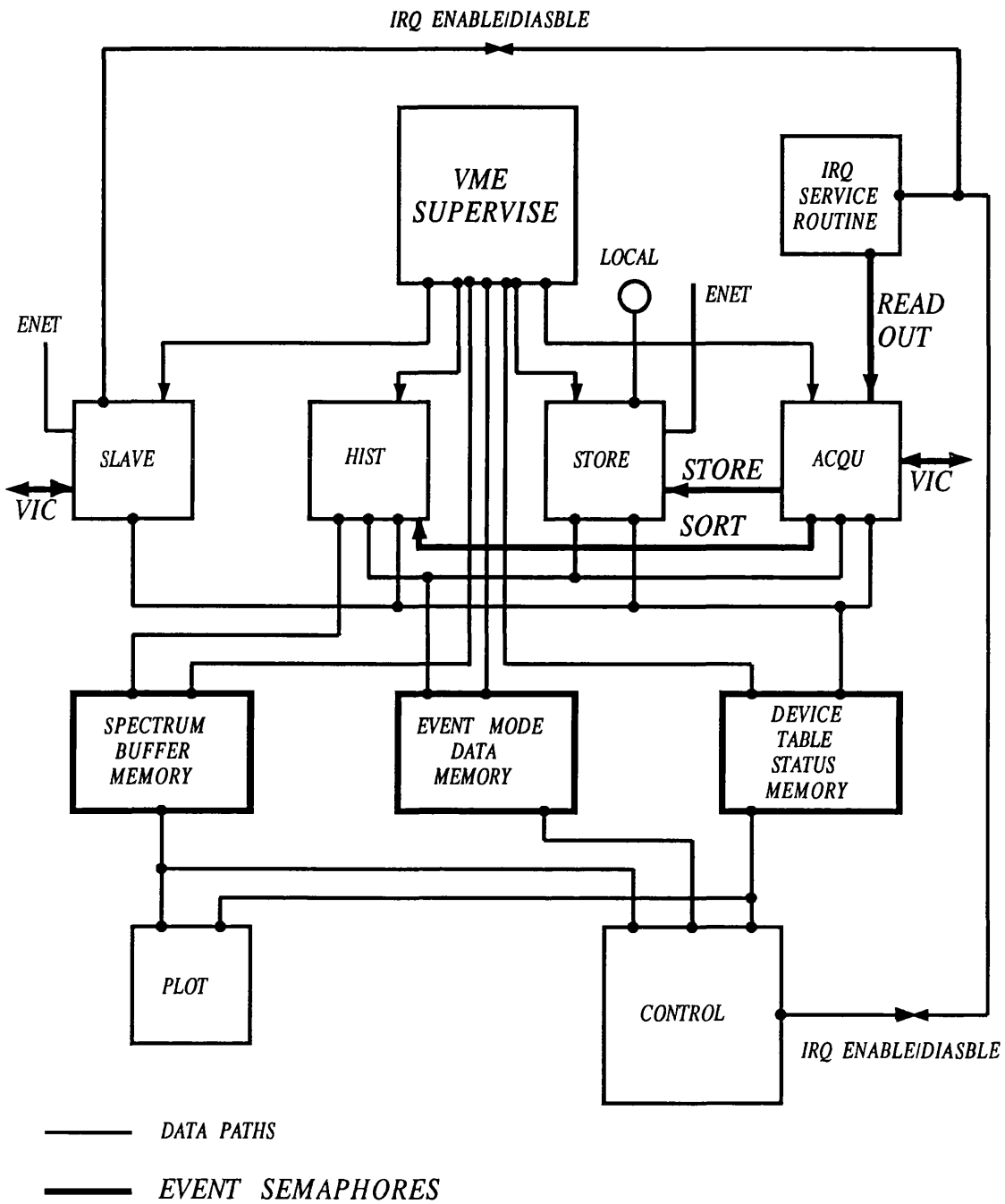


Figure 2.14: *Event processing*

enabling (disabling) the interrupt routine and is also able to check the status of the acquisition. The interrupt routine was kept simple to avoid disturbing the time-slicing within the VME-bus computer and rates of 70Hz were handled with little deadtime using the basic trigger.

Phillips 32 channel 10c2 and 10c6 FASTBUS ADCs were used, a separate channel for each photomultiplier tube. The TDCs were used in common start mode being started by the fast trigger and stopped by individual photomultiplier signals. The timing of the start signal is derived from the analogue sum of the 2 ends of the ΔE_1 as its pulse height is less dependent on the hit position than the individual pulses from either end. Struck 200 FASTBUS scalers were used to monitor the individual and coincidence rates from the blocks on PIP, TOF and the TAGGER, as well as the rates from the various trigger circuits. A number of scaler channels were left free running to show ungated rates and to measure the experimental deadtime ($\sim 10-30\%$ depending on the trigger employed).

ADC software thresholds were used to ensure that individual elements were only readout if they fired. This reduced the event lengths and hence processing overheads and deadtime by an order of magnitude. However, in a number of runs the QDC thresholds were removed in order to observe the effect of various hardware thresholds and to measure the magnitude of the pedestals, the channel corresponding to the small amount of charge accumulated by the QDC when it receives no signal.

Chapter 3

Detector Calibrations

Introduction

Detector calibration is required to convert the raw pulse heights and times measured by the QDCs and TDCs into physical quantities such as angles and energies. The angles are calculated from where the particle hits the detector, this position being derived from the time difference between the signal at either end of a block once walk corrections have been made. The energies are calculated from the total light output from the scintillator. The detailed methods of obtaining the necessary calibrations are described below. The data analysis also requires a knowledge of the particle type, and the methods used in PIP, E-E Δ measurements, and TOF, E- t measurements, are discussed below. The calibrations discussed only concern PIP and the TAGGER, as TOF was only used to identify the associated particle in the present work.

3.1 Particle Identification

3.1.1 PIP

In PIP the charged particles are identified from E- Δ E measurements. Light is lost by attenuation as it propagates along the bar with the result that the fraction of light detected is position dependent. To remove this position dependence the signals from both ends of the block are required to properly determine the energy deposited. Previous work [80] has shown that this attenuation is almost exponential and therefore the energy detected is proportional to the geometric mean of the pulse heights from either end of the block, *ie* $E \propto \sqrt{Q_1 Q_2}$. This has been shown to be a good approximation, better than 3.5% at all positions, for the E blocks in PIP [88]. An example of an E- Δ E spectrum is shown in figure 3.1(a), the loci of the various particle types are indicated. High energy particles which emerge from the back of a layer deposit smaller amounts of energy causing the dense regions of foldback. The particularly dense regions of foldback, marked # on figure 3.1, are caused by particles entering the E3 layer and which include some high energy electrons which were not rejected in the data set displayed. It is easy to identify protons and deuterons. However, the pions and background electrons overlap and the subsequent decay pulse is required to unambiguously identify π^+ s.

Proton identification was made by cutting on the proton regions in the 16 pixels defined by the overlap between the E1 blocks and Δ E₂ strips, an example

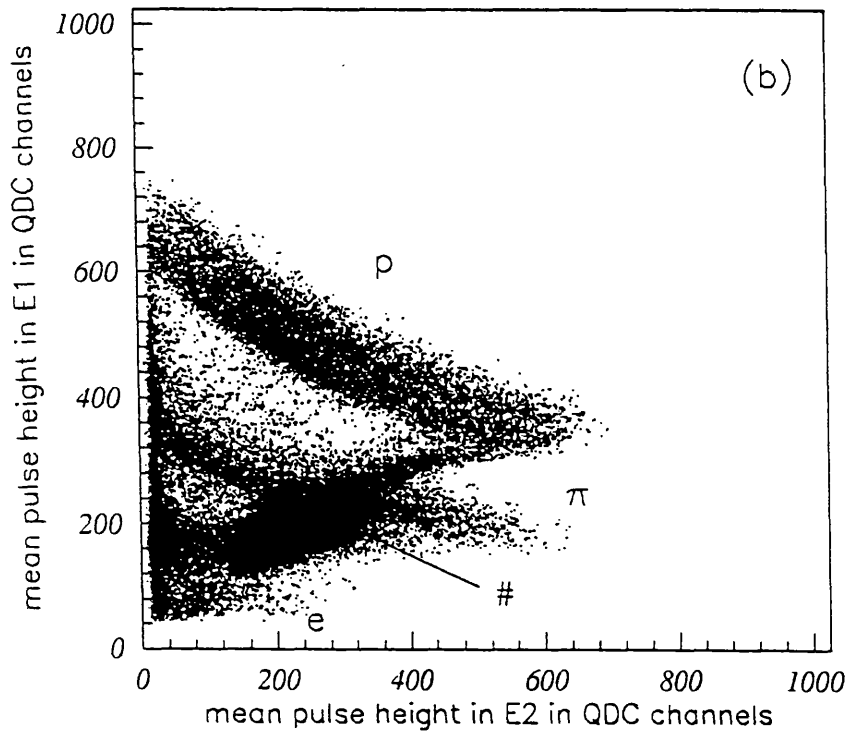
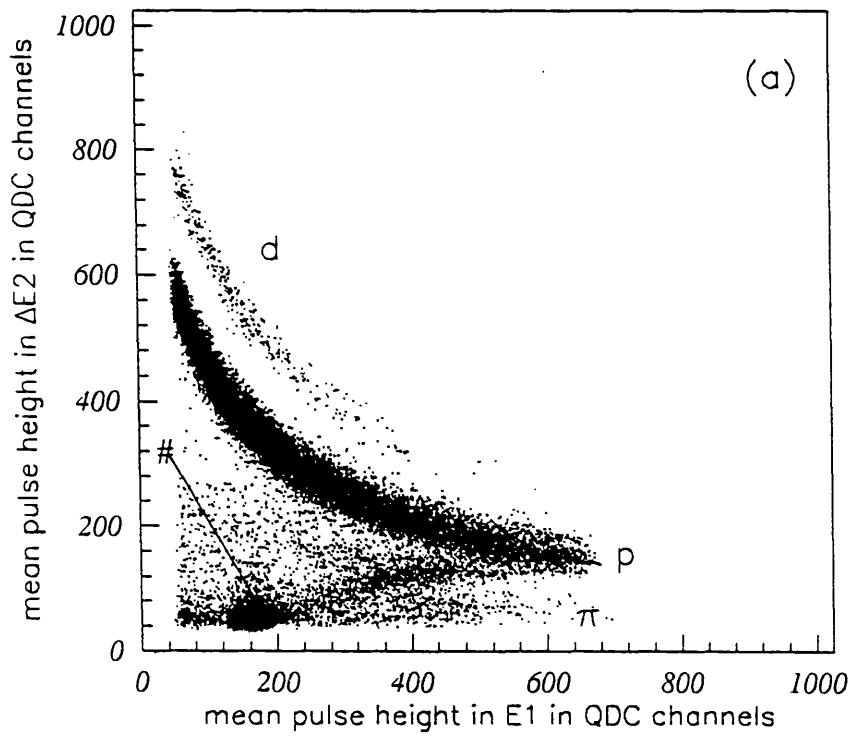


Figure 3.1: Particle identification in PIP

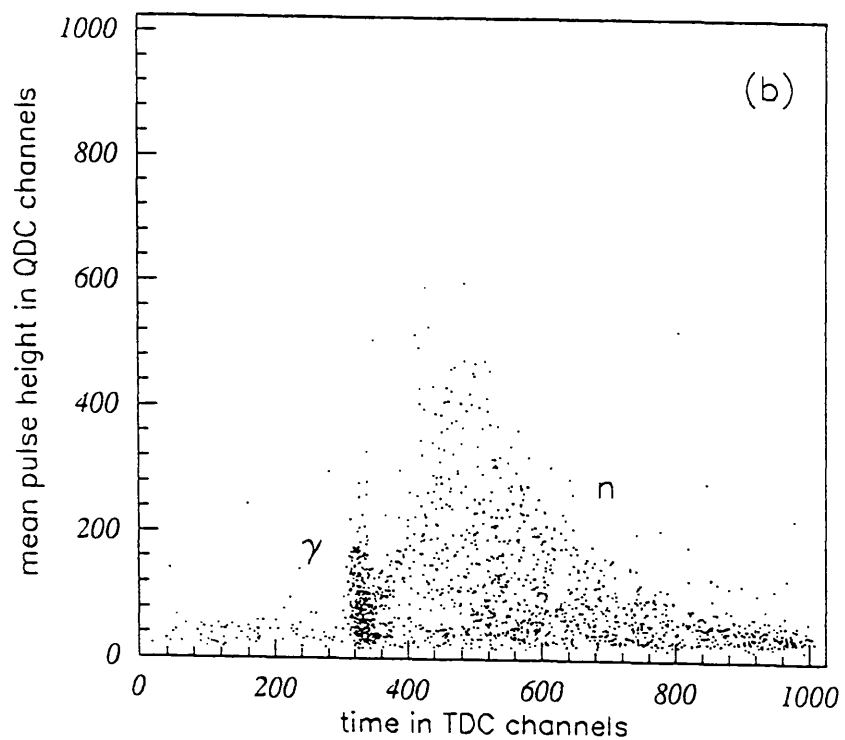
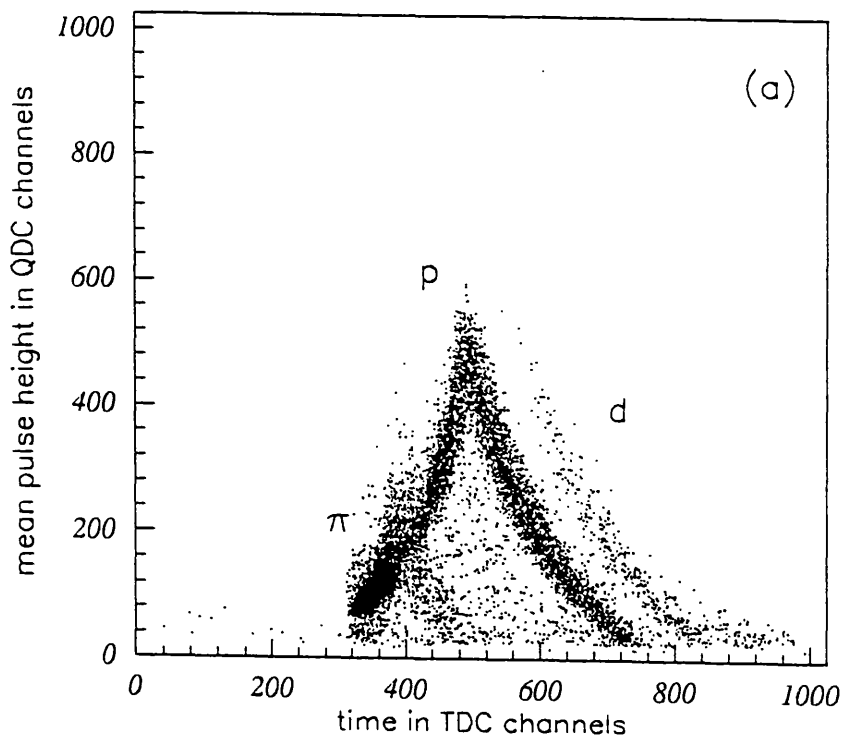


Figure 3.2: Particle identification in TOF

is shown in figure 3.1(a). Higher energy protons were included by using the proton region on the plot of the signals in E1 and E2 layers figure 3.1(b). Here the 'or' of all E2 blocks versus the 'or' of all E1 blocks was used since both sets of blocks are horizontal and therefore the overlaps are less well defined.

3.1.2 TOF

In TOF charged and neutral particles are distinguished by using the ΔE detector, since only charged particles will trigger both the ΔE and E blocks. Subsequent identification is made by pulse height *vs* time plots. Figures 3.2(a) and (b) show such a plot with and without a hit in the ΔE detector. The loci of the various particles (protons, pions and deuterons) are indicated.

Figure 3.2(b) shows the equivalent plot for neutral particles. Since the neutrons can deposit any fraction of their energy in the plastic, they can fall anywhere within that region which is defined by the loci of protons in figure 3.2(a). However, they are easily distinguishable from the photons which also deposit variable amount of their energy in the block, but which arrive at a unique time determined by the length of the flight path.

3.2 Walk Corrections

For reasons of cost and channel density leading edge discriminators were used. Although these introduce a pulse height time slewing on the output, tests [81] suggested that a simple walk correction yields timings at least as good as those obtained with constant fraction units.

In leading edge discriminators the output timing depends on when the pulse reaches the preset threshold. Therefore a small pulse, which takes longer to reach the threshold level, will have a later output than a large pulse arriving at the same time. In extreme cases the triggering time variation can be as much as the pulse rise time. In the analysis we have used the following formula derived from reference [82] to correct for this;

$$t' = t + r \left(1 - \sqrt{\frac{a_o}{a}}\right) - r_s \left(1 - \sqrt{\frac{a_{os}}{a_s}}\right) \quad (3.1)$$

where t and t' are the measured and corrected output times of the detector signal feeding the TDC stop input (in TDC channels), a_o is the discriminator threshold and a the pulse height (both in QDC channels), and r is the pulse rise time

defined as the time for a pulse to go from 10% to 90% of its height. The second term is required to compensate for the walk in the start detector as it is also subject to time slewing. The thresholds a_o and a_{os} can be measured simply from the QDC spectra leaving r and r_s (in TDC channels) as the only free parameters.

The rise time was fitted empirically using TDC *vs* QDC plots. An example is shown in figure 3.3(a) for protons stopping in a block in the E1 layer. The TDCs used in PIP had a resolution of ~ 0.1 ns per channel. The slewing of time with pulse height (energy) is clear. However, part of this is due to the dependence of flight time on energy (and therefore pulse height) and the dependence of scintillation light transit time on hit position (and therefore distance from photomultiplier tube). Therefore, if these times can be calculated and cancelled for each event all residual time slewing is due to the detector walk.

Inspection of the formula used to correct for the walk (stop only) shows that at maximum and minimum pulse heights the relationship between measured and correct hit times are

$$t' = t \quad a = a_o \quad (3.2)$$

$$t' = t + r \quad a \gg a_o \quad (3.3)$$

Therefore the rise time can be estimated by taking the difference between the centre of the ridge at very small and very large pulse heights.

The walk correction in the start detector was established first as it can be deduced independently from the rest of the detector. The rise time was measured on a spectrum of the start detector analogue sum QDC *vs* a TAGGER TDC. There is no time slewing inherent in the signals from the TAGGER as this used high/low dual threshold discriminators which have minimal walk. In addition, the signals produced by the electrons have a small range of pulse heights minimising any walk effects and these pulse heights have no correlation with the pulse height in the start detector. The small flight time to the start detector was estimated assuming that particles with $a \sim a_o$ were relativistic electrons and those with maximum a were protons just above threshold in the E1 layer. A rise time of 5ns for the start detector was estimated in this way.

The rise time for the stop signals in the E1 and ΔE_2 layers were then deduced. As the stop detectors use a wider dynamic range in their QDCs and affect the position calibration more care was taken in estimating the flight and transit times for these elements. A rough calibration was made using the methods described later in the chapter using a nominal value of 5ns for the rise time. This value was

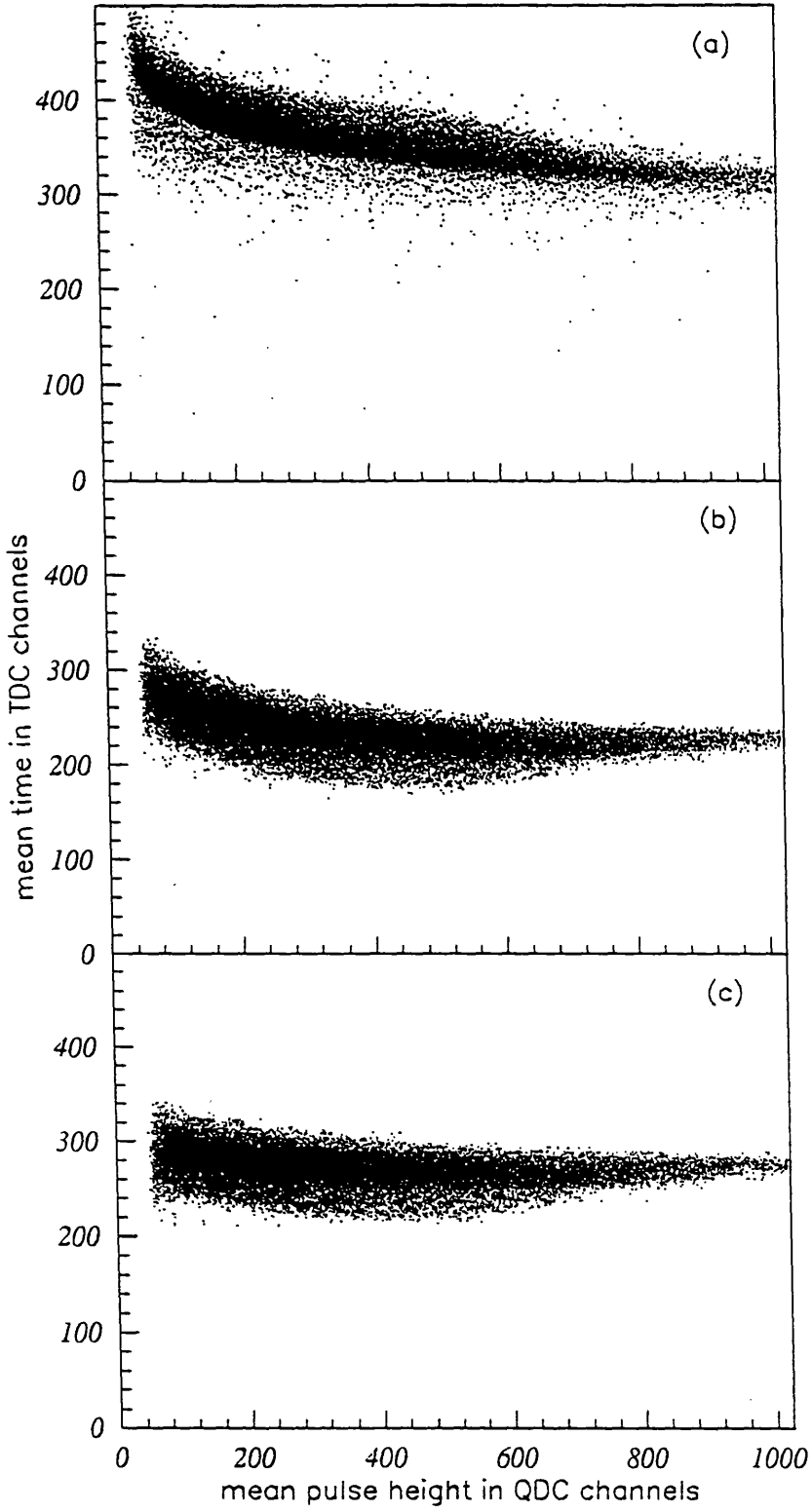


Figure 3.3: *Estimation of rise times*

obtained in bench tests of the TOF detector [81] and is similar to values observed using an oscilloscope to view the pulses. The flight time can now be calculated from the particle type, flight path and particle energy, low energy protons in PIP having been selected by demanding a hit on the proton region in any E- Δ E plot, *eg* figure 3.1(a). The transit time was calculated from the distance from the hit to the photomultiplier tube and the effective velocity of light along the block, v . This velocity was calculated from the parameters obtained for the position calibration.

Given

$$x = m(t_2 - t_1) + \text{constant} \quad (3.4)$$

where x is the hit position, m and *constant* are the calibration values and t_1 and t_2 are the times taken to travel to the photomultiplier tubes. For a shift in hit position, Δx ,

$$\Delta t_1 = -\frac{\Delta x}{v} \quad \text{and} \quad \Delta t_2 = \frac{\Delta x}{v} \quad (3.5)$$

It follows that

$$\frac{\Delta(t_2 - t_1)}{\Delta x} = \frac{2}{v} = \frac{1}{m} \quad (3.6)$$

ie

$$v = 2m. \quad (3.7)$$

Figure 3.3(b) shows the QDC *vs* TDC plot once the transit and flight times, and the walk correction for the start detector, have been subtracted.

Figure 3.3(c) shows scatter plots of QDC *vs* TDC constants once all the corrections have been made, using a rise time of 6ns measured from figure 3.3(b) for the E1 layer. The ridge is approximately flat suggesting that the parameterisation used is adequate. The increased width of the ridge in figure 3.3(b) is probably due to the rough calibrations used. However, the results suggest that the corrections are adequate for the present analysis.

3.3 Position Calibrations

The position of a hit in any detector in PIP is derived from the time difference between the signals at either end of the detector. The vertical position of a hit, y , is obtained from the ΔE_2 layer and the horizontal position, z , from the E1 layer. The third coordinate, x , is assumed to be the front face of the E1 layer for the purpose of calculating the particles' trajectories. Simple calculations suggest

that for the moderate proton energies considered here the light from the start of a track will always be the first to reach the photomultiplier tube, regardless of the track orientation. However, as the particles' energies become relativistic the speed of the light and particles will be similar, and at extreme angles light from further down the track may reach the photomultiplier tube first resulting in errors in the position measured. Therefore, more complicated techniques may be required to estimate the hit positions of pions and very high energy protons.

The points used in the position calibration for the E1 block were provided by the edges of the ΔE_2 strips. Four time difference spectra were obtained for each E1 block, each requiring a coincidence with a different ΔE_2 element. These spectra were superimposed on each other and the position where two spectra overlapped was taken to be the join between the two ΔE_2 strips. This yields 3 well defined positions at the overlaps and 2 less well defined positions at the ends. An example is shown in figure 3.4(a), where events containing protons stopping in the E1 layer PIP have been selected (section 3.1). Monte Carlo simulations have previously shown that this technique is sufficiently accurate [83]. The results are shown in figure 3.4(b) where a linear fit has been used. The end points fit well on the line showing that the use of light guides has greatly improved the linearity of the time *vs* position response compared to a previous detector which had no light guides [85].

A similar technique, *ie* selecting events in the individual E1 blocks, was used for the ΔE_2 elements. The results were similar to those of the E1 blocks, and a linear fit was again obtained.

This technique could not be applied to the subsequent layers as additional uncertainty is introduced by the scattering of the particles inside the thick scintillator blocks. As positions in these layers are required only for tracking particles and droop corrections (see section 3.5.2) a rougher calibration using only the ends of the time difference spectra was employed.

The shapes of the edges of the overlaps were used to estimate the position resolution by measuring their width at half height. The results suggest a resolution of ~ 3 cm FWHM in the E1 layer and ~ 5 cm FWHM in the ΔE_2 layer. These results are similar to those obtained from the analysis of cosmic data (section 3.5), but slightly larger than those obtained for the previous detector. These results may be misleading as neither of these methods is ideal for estimating the position resolution. A better method might be to set up masking plates in front of the detector with a series of ~ 1 cm slits. This would give a more direct and

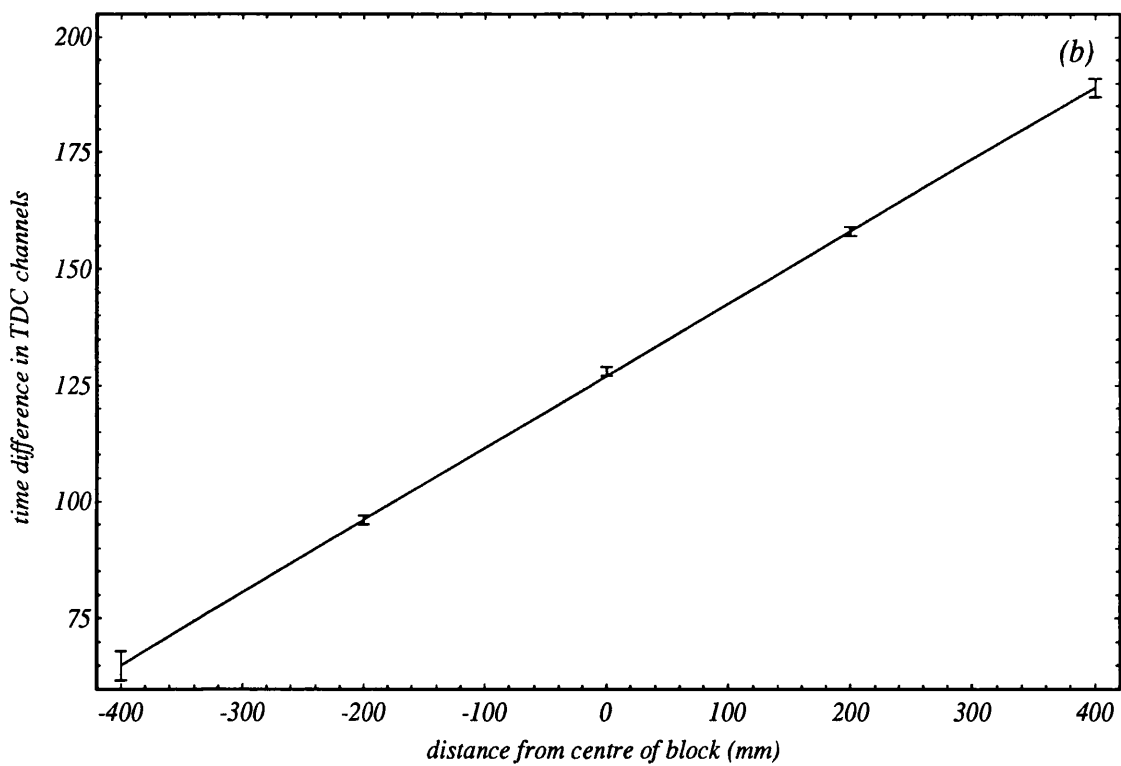
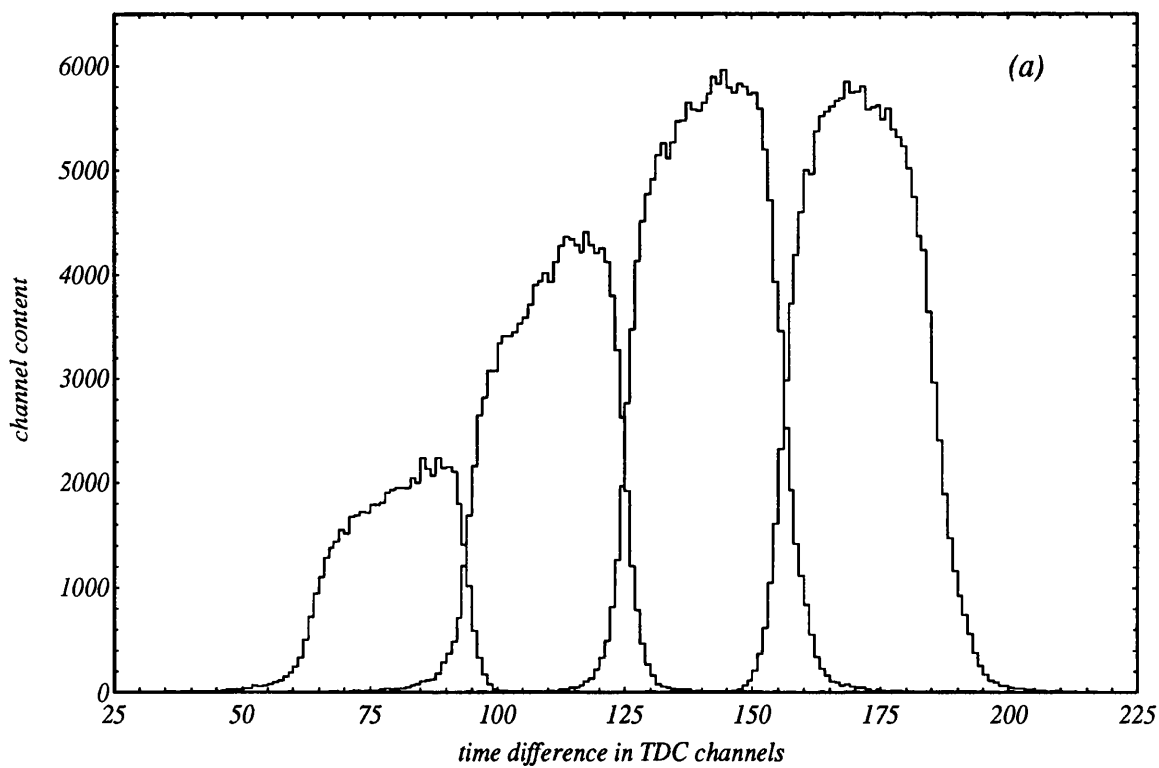


Figure 3.4: *Position calibration*

accurate measurement of the position resolution.

As the physical position of PIP relative to the target is well known it is easy to translate the position of a hit on the detector into the lab frame, and hence calculate the trajectory. The resulting uncertainty on the measured angles can also be estimated using both the position resolution and the uncertainty in the reaction position in the target. These were calculated at 90° and gave results of $\sim 5^\circ$ FWHM for the polar angle θ and $\sim 7^\circ$ for the azimuthal angle ϕ .

3.4 Energy Calibrations

3.4.1 The TAGGER

The TAGGER was calibrated independently of the main experiment. The spectrometer magnet underwent stringent tests [66] before being installed and its field profile was accurately mapped. An NMR probe is permanently set up inside the spectrometer, offset from the central axis so as not to intercept the electrons' trajectories, to monitor the field constantly. From this NMR reading and the recorded field maps the actual field distribution can be accurately calculated. This was verified by comparing the incident energy, calculated from the MAMI-B optics, with that obtained from the NMR field required to accurately position the residual beam on the correct axis as defined by a screen just in front of the Faraday cup. The results agree to within the bounds of experimental error, $\sim \pm 500\text{keV}$.

The trajectories of the recoil electrons can be readily calculated using the spectrometer field profile. As the position and orientation of the Focal Plane Detector (FPD) has been accurately measured a relationship between the hit position and the energy of the recoil electron can be deduced. Two sets of tests to determine the FPD calibration were performed. First low intensity beams of various incident energies were extracted from MAMI-B and their energies calculated from the hit position on the FPD using a standard 1 Tesla field in the TAGGER. The energies from the TAGGER and MAMI-B optics agreed well. Then an electron beam with an incident energy of 300MeV was scanned across the focal plane by altering the magnetic field. Although the spectrometer field profile has not been mapped at these settings below 1 Tesla there is agreement in the energies measured by the two different methods to within $\pm 500\text{keV}$.

3.4.2 PIP

The energy loss of particles in the PIP E blocks is obtained from the amplitude of the scintillation light which they produce. The total energy of the incident particles is then obtained by summing the energy losses measured in the E blocks and adding the calculated energy losses in materials between the target and E1 layers and material between succeeding E blocks. It is possible to estimate these losses in the ΔE layers from the scintillation light produced, but as they are both transmission layers there is very little energy deposited in them and their response is in 'fold-back'. Trying to measure these energies directly would therefore be difficult and result in poor resolution. The energy lost in the ΔE layers and that lost in the wrappings, the target and the air are estimated using standard range-energy tabulations [84]. This method has been used successfully in the analysis of the MAMI-A data [85].

In order to calculate the relation between the incident and emergent energies of particles traversing scintillator or other materials the relationship $R = cE^k$ was used. Hence the relationship between the incident and emergent particle energies (E and E' respectively) is given by the expression [85]

$$E' = \left[E^k - \frac{x}{c} \right]^{\frac{1}{k}} \quad (3.8)$$

where $x = R(E) - R(E')$ is the pathlength in the medium and c and k are fitted parameters.

To obtain the magnitude of scintillation light from an E block the geometric mean of the photomultiplier signals at the two ends was calculated. The relationship between the total light output from a plastic scintillator and the energy of the incident particle is known to be non-linear due to the quenching in scintillator efficiency for slow particles which have a high rate of energy loss. This relationship can be represented by the following expression [71], [86], [87]

$$L = a_1 E - a_2 (1 - \exp(-a_3 E^{a_4})) \quad (3.9)$$

where E is the incident proton energy, L the light detected and a_1, a_2, a_3, a_4 are parameters. The non-linearities contained in equation 3.9 are important only for energies below ~ 15 MeV, and the present electronic thresholds were set at ~ 18 MeV proton energy. Therefore for the range of energies measured in PIP equation 3.9 reduces to

$$L = a_1 E - a_2 = a_1 (E - E_o). \quad (3.10)$$

The effects of the quenching are contained in the energy offset E_o which has a value $\sim 8\text{MeV}$ for protons in plastic scintillator. Values of a_1 and E_o were contained within the calibrations described below. However, as the other particle types detected produce different degrees of quenching this calibration method is a function of particle type.

To calibrate PIP the two body photo-disintegration of deuterium was exploited. Below the pion threshold there is only one reaction channel in the photodisintegration of the deuteron, $D(\gamma, pn)$. As this channel has two bodies in the final state the kinematics are completely defined by 2 variables, here E_γ and θ_p which can both be independently derived. Data from CD_2 runs were used and events in which a proton was identified stopping in the E1 layer were selected (section 3.1). The proton energy expected from deuteron disintegration was then calculated from E_γ and θ_p , for events in the prompt region of the TAGGER TDCs (see section 4.1).

A scatter plot of the calculated proton energy versus the mean observed pulse height shown in figure 3.5 gives the required energy calibration. There is a background of events due to the $C(\gamma, p)X$ reaction, other D breakup channels above the pion production threshold, and random coincidences between PIP and the TAGGER (for which the calculated proton energy is incorrect). At the high electron beam currents used in these experiments an average of 6 residual electrons were detected in the TAGGER for each event. If more than one of these electrons arrived within the prompt region (section 4.1) it is impossible to tell which one is associated with the photon causing the reaction. In this circumstance each E_γ is calculated and used in the analysis. However, a clearly defined ridge due to the $D(\gamma, pn)$ reaction is seen and so no attempt was made to remove any of these background components. A second, shorter, ridge can also clearly be seen, this is due to protons from the $^{12}\text{C}(\gamma, p)^{11}\text{B}$ two-body breakup reaction.

Figure 3.5(a) shows the results before the energy losses of protons on the way to the E1 block have been estimated and corrected for. The ridge becomes severely non-linear at low energies due to this effect. Figure 3.5(b) shows the same data but with the estimated losses in the transmission layers subtracted from the calculated energy. The ridge is now approximately straight along its entire length, the offset and slight deviation at low energies being due to quenching effects in the scintillator discussed earlier. The values of the offset E_o obtained for each E1 block are all close to 8 MeV as expected [71].

Although the calibration described above works well for the E1 layer it is more

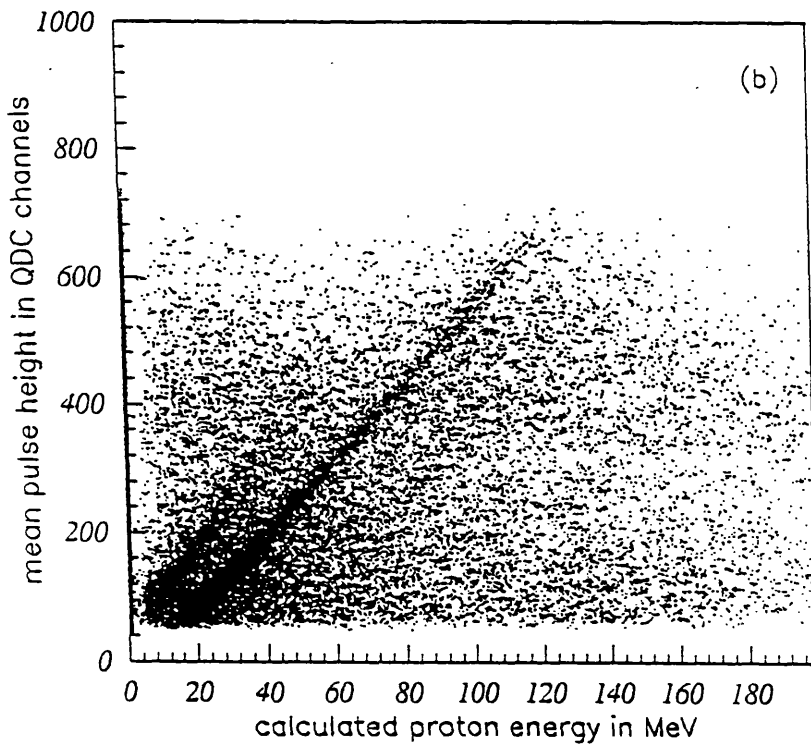
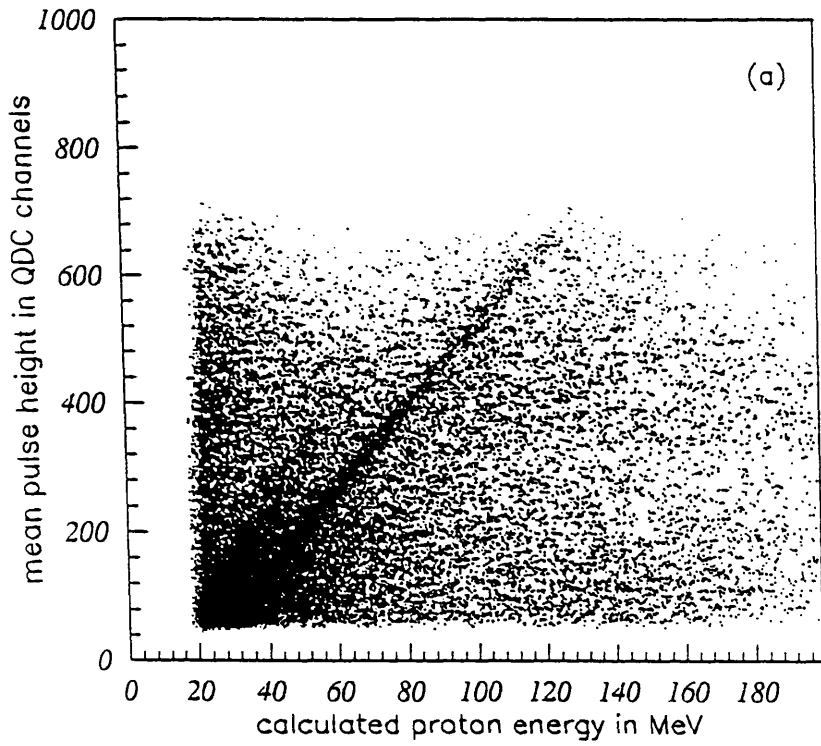


Figure 3.5: *Energy calibration for the E1 layer*

difficult to use in the subsequent layers as the various background components discussed above increase with energy whereas the $D(\gamma, pn)$ cross section decreases. A method of inter-calibrating the layers of the detector with cosmic muons is discussed in section 3.5 and this has been used to extend the calibration of the E1 layer to the E2-E4 layers. In this procedure the pulse heights from the E2 layer were normalised to a block in E1 and the deposited energy in the E2 layer calculated. Comparisons of the relative values obtained from the two methods for the E1 layer showed that the results are equivalent to within the resolution.

The total energy of a particle stopping in E2 is therefore the measured energy deposited in E1 and E2 plus the calculated energy loss in the wrappings between E1 and E2, and the calculated energy lost in getting to E1. The total energy deposited in the E2 scintillators was calculated from the normalised sum of the pulse heights. The total ‘measured’ energy thus obtained is plotted against the energy calculated from the $D(\gamma, pn)$ reaction kinematics in figure 3.6. Again the clear ridge due to the $D(\gamma, pn)$ reaction is seen, extending the calibration to 180MeV where the $D(\gamma, pn)$ cross section can no longer be observed above the background.

The width of the ridge is the difference between the measured energy and that obtained from the two-body kinematics, and is a measure of the energy resolution. However, there are a number of other factors which broaden the difference and which must be unfolded to extract the intrinsic energy resolution. These additional uncertainties are due to the finite resolution of the photon energy and proton angle measurements (ΔE_γ and ΔE_{θ_p} respectively) and the uncertainty in the energy loss in the target (ΔE_{targ}).

The range of possible energy losses in the target is dependent on the maximum path length within the target. The distance traversed within the target is smallest for backward proton angles and so only events in which protons hit the two backward ΔE_2 elements in PIP were considered in estimating the detector resolution.

The difference between the measured energy from pulse height and calculated energy for $D(\gamma, pn)$ kinematics was calculated for a number of proton energy bins and the background due to carbon subtracted. This left a narrow peak due to $D(\gamma, pn)$ events whose width was determined using a Gaussian fit (figure 3.7). The FWHM contributions from other sources were calculated from the deuterium kinematics to be 0.7MeV from ΔE_γ , 1.2MeV from ΔE_{θ_p} and 1.3MeV from ΔE_{targ} . These were subtracted in quadrature leaving the intrinsic resolution of 3.3MeV

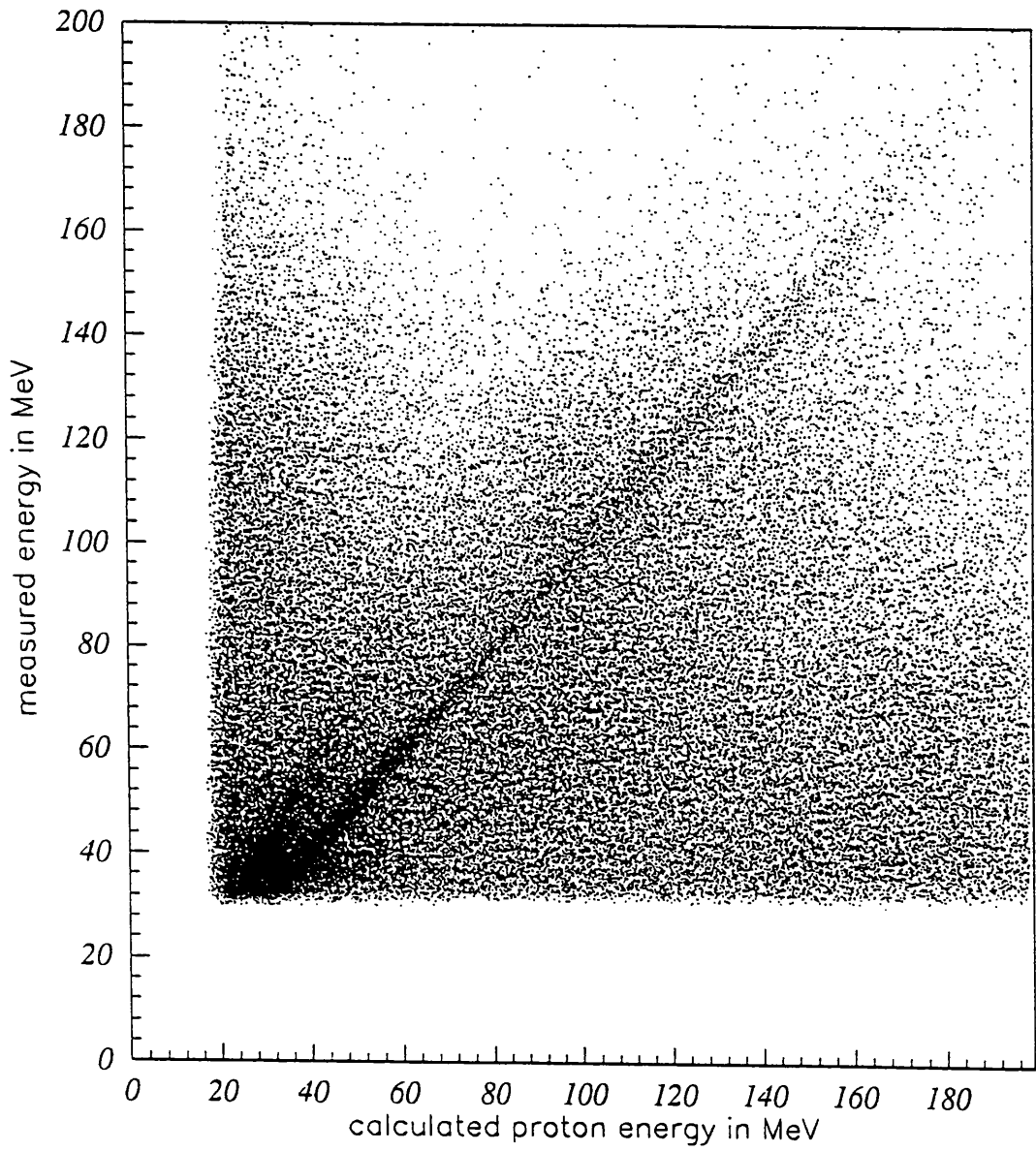


Figure 3.6: *Measured vs calculated energy*

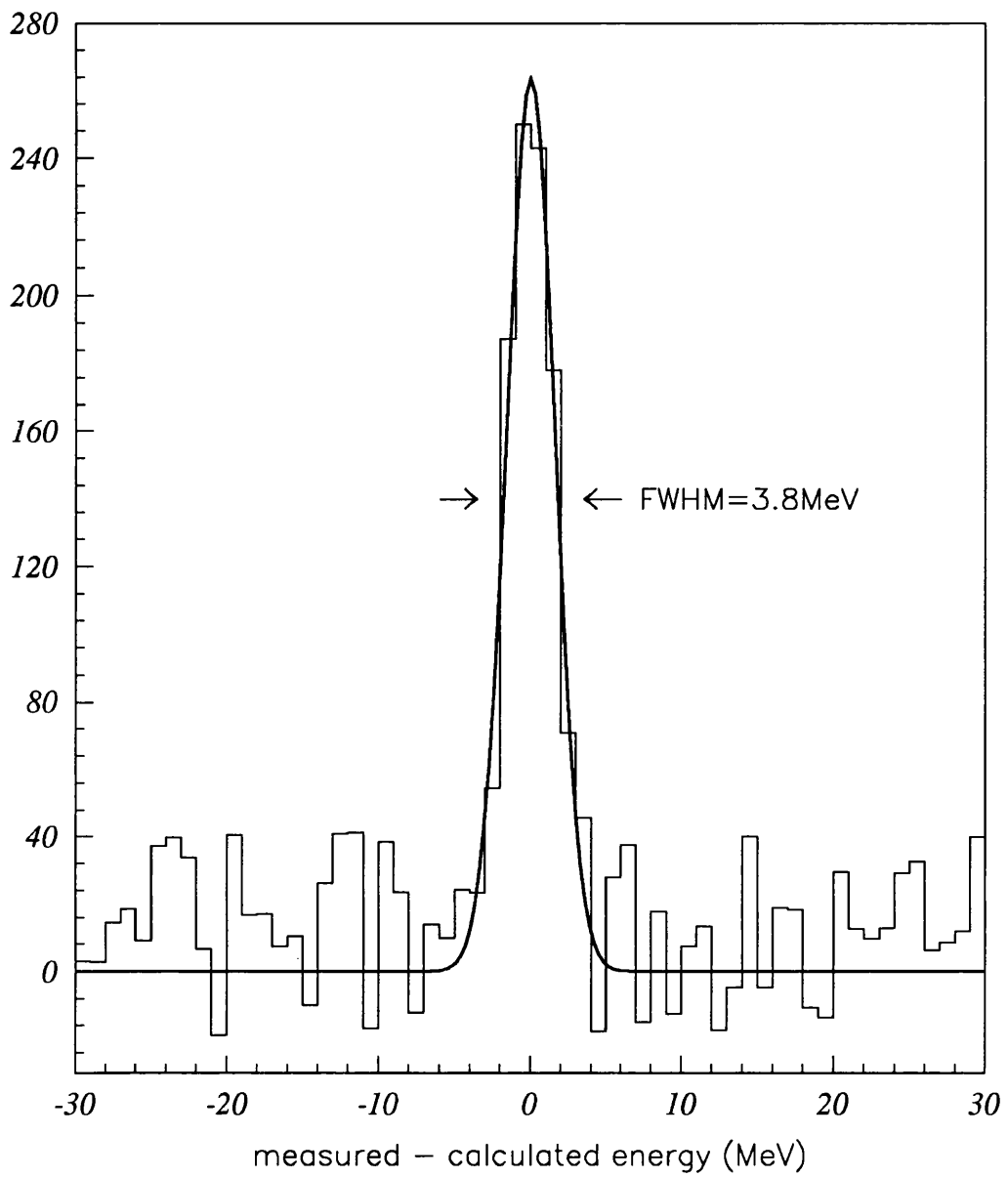


Figure 3.7: *Energy resolution for protons of energy 50-60MeV*

FWHM for the 50-60MeV bin shown in figure 3.7. This preliminary value of $\sim 6\%$ was typical for all energies up to 150MeV, above which the statistical variations due to the small $D(\gamma, pn)$ cross section makes the resolution hard to estimate. A more accurate estimation should be forthcoming once the position resolution has been better measured and a detailed simulation of the detector response has been attempted.

3.5 Cosmic Ray Data and Gain Monitoring

3.5.1 Energy calibrations

As mentioned earlier, the use of two body kinematics to calibrate the E2-E4 blocks becomes harder at higher energies and cosmic ray data must be used to provide the energy calibrations for these layers [88]. The cosmic muons deposit a constant 2MeV/cm in plastic scintillator and since the cosmic rays are all travelling approximately vertically they have similar path length in the scintillator and therefore produce a peak in the QDC spectrum. By considering the position of this peak in each block relative gains can be calculated. To sharpen the peak the QDC signals were corrected for the path length of the muons in the scintillator, reducing differences due to the larger path lengths at trajectories other than vertical. As both the cosmic and two body calibrations were performed on the E1 layer it was possible to express the relative gains as calibrations once corrections had been made for the different thicknesses of the E1 and E2 layers.

The fitting of these cosmic ray trajectories also provided additional information about the position resolution [74]. The position of the cosmic ray was calculated for every block in the layer it passed through and a straight line fitted to these positions. The difference between the fitted trajectory and measured positions in each block were then used to give an indication of the position resolution. The results obtained in this way were similar to those obtained by the position calibration at $\sim 3\text{cm}$ FWHM for the E1 layer.

3.5.2 Droop corrections

The assumption that the attenuation of scintillation light along the bars is exponential is only an approximation and the appropriate correction was obtained from the cosmic ray data [88]. To do this the geometric mean of the pulse height was calculated at various positions along the length of the bars, having again

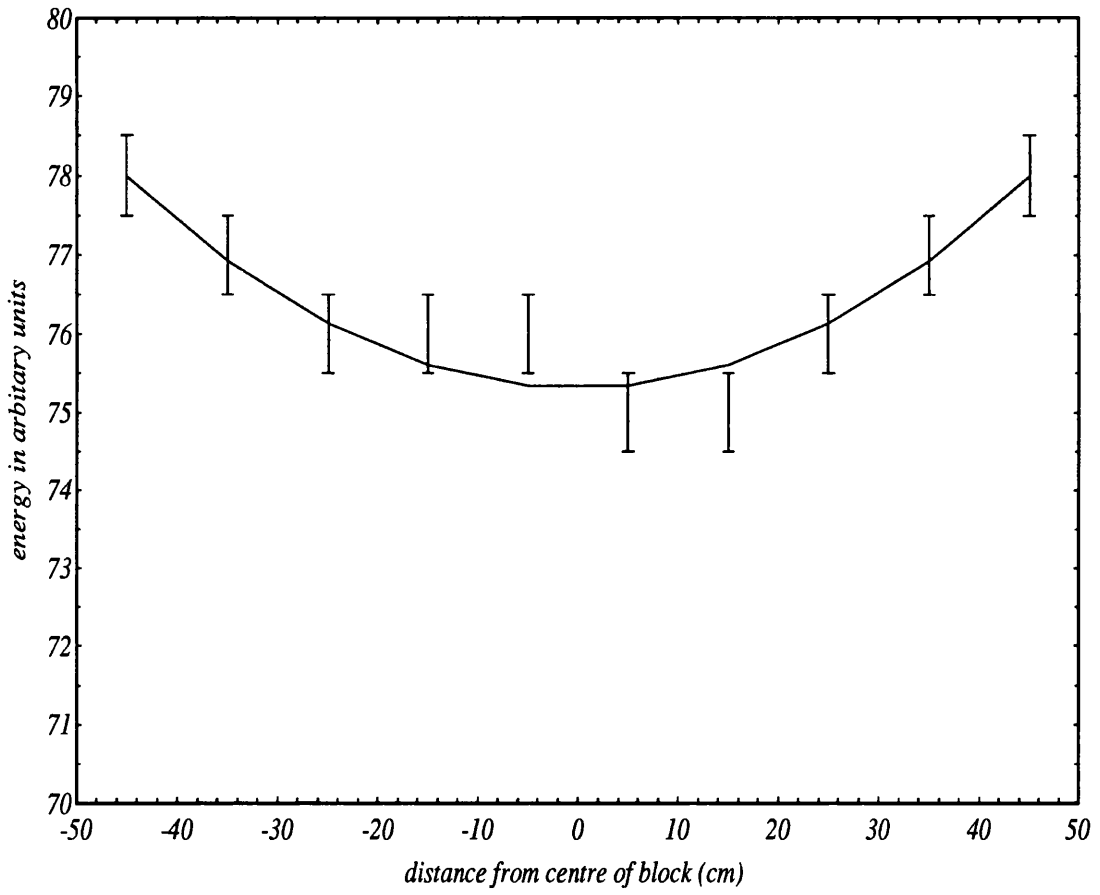


Figure 3.8: *Droop along an E bar*

corrected for the different path lengths through the scintillator. Results for a block in the E1 layer are shown in figure 3.8 which shows that the variation due to residual droop is $\sim 3\%$ in the E1 and E2 layers. A parabolic function was fitted to this data and used to correct the geometric means for the residual droop, figure 3.8.

3.5.3 Gain monitoring in PIP and TOF

The amplitude of the cosmic peak signal in the PIP E block scintillators should remain stable, any drifts being due to changes in the detector gain. Thus monitoring the amplitude of the cosmic peak as a function of time will show any drifts in gain. Off-line analysis showed that the amplitude of the cosmic peak varied by less than 5% for all E blocks throughout the data taking period [88].

Cosmic ray peaks would be very broad in the vertical scintillators and therefore in TOF the gain monitoring is performed by using a stable LED flasher pulse [75]. This is a useful method of gain monitoring as both the pulse height and timing can be set independently, allowing the pulse to arrive at a different time to the data with a pulse height reflecting that of the data. As the LED produces a very narrow peak in the pulse height spectrum any drifts can be accurately assessed over a short timescale. A similar system has now been developed for gain monitoring in PIP [89] in future experiments, this will allow gain drifts to be monitored over shorter timescales than cosmic information permits.

3.6 Detector Performance

An example of a proton energy spectrum is shown in figure 3.9. This is a good guide to the performance of PIP as it highlights the effects of the upper and lower thresholds discussed previously. The data were restricted to events which had photon energies between 390 and 410MeV, and the resulting spectra are shown for two separate angles.

Protons of energies as low as 30MeV are detected, but the actual lower energy threshold should be taken as 40MeV. Between these limits the probability of a proton being detected is determined by its trajectory, protons normal to PIP have to traverse less material before reaching the E1 layer and deposit more energy in the detector and can produce a trigger. Protons of incident energy 40MeV have sufficient energy to trigger the detector regardless of track orientation. PIP was

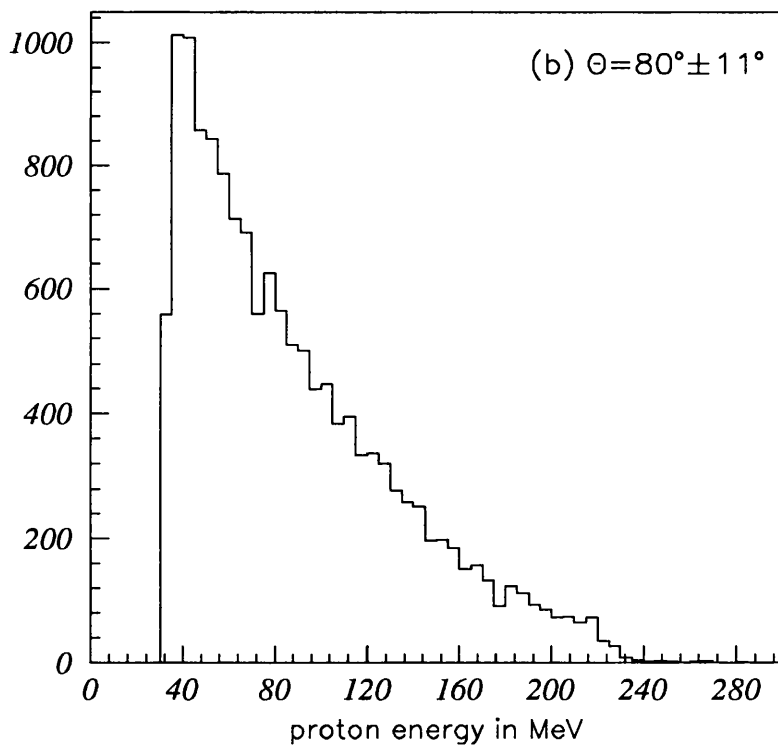
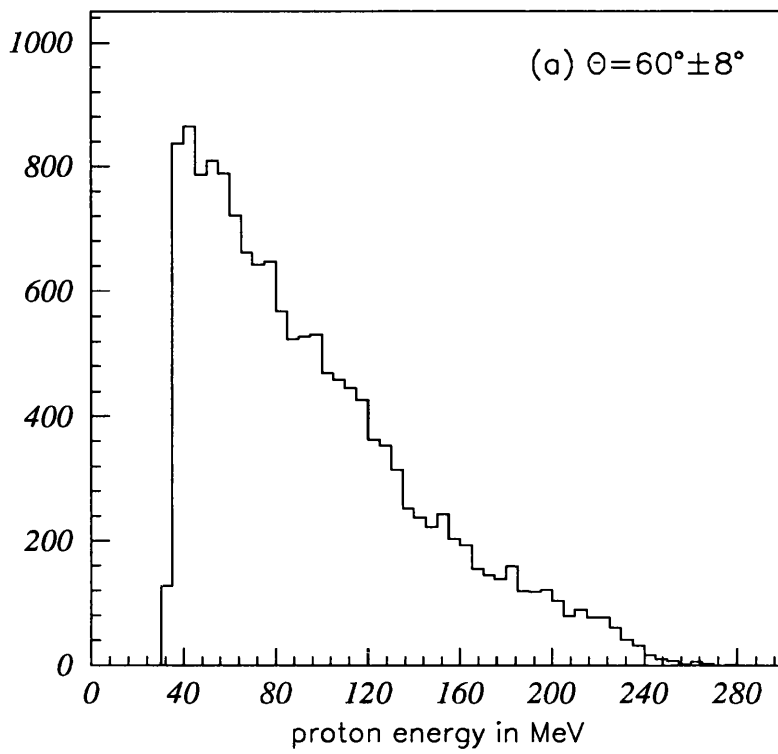


Figure 3.9: A typical proton energy spectrum

designed to have an effective threshold of $\sim 30\text{MeV}$, but the value here is slightly higher due to the software discriminator threshold and gain settings used.

A similar effect is observed in the upper energy threshold. Protons entering the E3 layer are in fold-back in the E2 layer and therefore will not be identified as protons in the $E-\Delta E$ spectra. The presence of the upper energy threshold is apparent for incident photon energies of 400MeV and greater, and lies between 220 and 240MeV at 60° (figure 3.9(a)). The threshold is again a function of geometry, and is nearer 200MeV at 90° (figure 3.9(b)), where the protons have to traverse the least depth of scintillator before reaching E3. This upper threshold can therefore be increased simply by including the E3 and E4 layers as required.

Chapter 4

Data Analysis

Introduction

The results presented in this thesis are from the analysis of tagged photon data from a ^{12}C target. The beam time comprised 20 hours using the main trigger and 10 hours using a trigger which required a coincidence with TOF. The data are displayed as proton energy spectra where the counts have been corrected to give differential cross sections. Both inclusive (γ, p) reactions and exclusive (γ, pn) , (γ, pp) and $(\gamma, p\pi)$ reactions, in which both the emitted particles are detected in coincidence, are studied.

The spectra were generated by the program ACQU [90] which was written at the Kelvin Lab and the CERN package PAW [91] was used in subsequent subtraction and normalisations. A theoretical comparison to the data is provided by the Monte Carlo simulation PICA [95].

4.1 Data Reduction

Before any cuts were made on particle type cosmic and flasher events were removed from the data to avoid contaminating the spectra. This was achieved by rejecting all events in the empty TAGGER channel associated with the cosmic trigger (section 2.5.1).

The remaining data were examined to select events containing protons stopping in the first two layers of PIP yielding the (γ, p) data sets used to obtain the inclusive cross sections. Further sets of coincidence data were generated for the exclusive reactions studied. The methods used for selecting the particle types in the various detectors are described below.

PIP

As described in section 3.1 the charged particles in PIP are identified from $E-\Delta E$ measurements (figure 3.1). Protons stopping in the first layer were selected by choosing events where there was a hit in the proton region of one of the sixteen $E1-\Delta E_2$ pixels. This cut accepted events ($\sim 2\%$) where a particle outwith the proton region in one pixel was detected in coincidence with a proton in another pixel. The method of particle selection rejected some of those protons which passed through more than one block in any layer and which therefore deposited only part of their energy in each block. As this geometrical effect is of order 3% no attempt was made to recover these events. Protons stopping in the E2 layer

were selected by requiring an event in the proton ridge in the 'or' of E2 *vs* the 'or' of E1 plot. Again a small number ($< 4\%$) of protons will be lost if they deposit energy in more than one block in either layer.

TOF

The TOF array was used to identify the second particle. To keep the neutron efficiencies and charged particle acceptances constant it was decided to ignore stand F, which was mounted behind E. It was also decided to ignore stand A, which lay close to the beam, to reduce the random background accepted. In addition, only those bars whose QDCs and TDCs were present and stable throughout the entire period of data taking were used. These cuts resulted in a total of 64 out of a possible 96 bars being used.

The plots used for identifying the particles in TOF are shown in figure 3.2. Neutrons, protons and pions were selected by defining generous regions around their loci on these plots. These regions accept random events which have to be accounted for by subtracting off a suitably normalised random sample, this is discussed fully in section 4.2.2 below.

The use of pulse height *vs* time plots for charged particle identification (figure 3.2(a)) successfully discriminates between protons and deuterons. However, there is an overlap between the high energy protons and pions as a very limited range of both particles' energies are stopped in the 5cm thickness. Some additional information can be gleaned from E- ΔE plots, but it is impossible to avoid some contamination of pions by high energy protons. The use of more than one thick layer of scintillator, such as in stands E and F, would improve the separation as a larger range of particle energies are stopped.

The situation for neutrons is somewhat more complicated due to the need to reduce background (section 4.2). There was a gap between segments in the ΔE which shadowed 3-4 bars of stand D. Since charged particles at these angles could not trigger the ΔE , protons could no longer be distinguished from neutrons using the ΔE signals. Instead, the region on pulse height *vs* time plots normally used to accept protons was used to reject those protons contaminating the neutron data set. This results in a $\sim 4\%$ loss of yield in the (γ, pn) data set. Similarly there will be a $\sim 6\%$ loss of yield in the (γ, pp) and $(\gamma, p\pi)$ data sets due to the lost solid angle.

The TAGGER

Each ladder channel has a TDC started by the event trigger and stopped by a signal from a residual Bremsstrahlung electron. Figure 4.1 shows the TDC spectrum constructed from an ‘or’ of all channels of the ladder. Each ladder channel has been aligned so that the ‘prompt’ peak is in the same TDC channel. This prompt peak is generated by the electrons associated with the photon causing the reaction and is clearly visible for all TAGGER channels. The continuum under the prompt peak is generated by residual electrons which are not associated with the photon causing the reaction. At the electron beam current used in this experiment each event has an average of six residual electrons detected in the focal plane. These random electrons can occur at any time within the TDC gate, including the prompt region. To correct for the randoms underneath the prompt peak, random events are selected from the other regions shown in figure 4.1. The method used to subtract random events is discussed in the next section.

4.2 Random and Background Subtraction

Reduced data sets of the reactions of interest; (γ, p) , (γ, pn) , (γ, pp) and $(\gamma, p\pi)$ were generated for the analysis. As PIP makes the trigger a significant fraction of events in the prompt coincidence regions in the TAGGER and TOF are randoms, and these must be accounted for by subtracting off purely random events. Another source of background is caused by interactions with the air around the target, interactions away from the target being unlikely to hit the start detector and form the trigger. These are measured in an empty target run and are also subtracted from the final spectra.

4.2.1 The TAGGER

The largest random contribution comes from the randoms below the prompt peak in the TAGGER. These randoms cannot be identified event-by-event. Instead an equivalent number of purely random events are subtracted from the final spectra using the random regions discussed in the previous section. Two large equal sized regions were used, one before the prompt peak and one after, to ensure that the correct fraction is removed and to provide good statistical accuracy. Events from these regions, which are chosen to be much broader than the prompt region, have to be renormalised before the subtraction. It has been shown [92] that

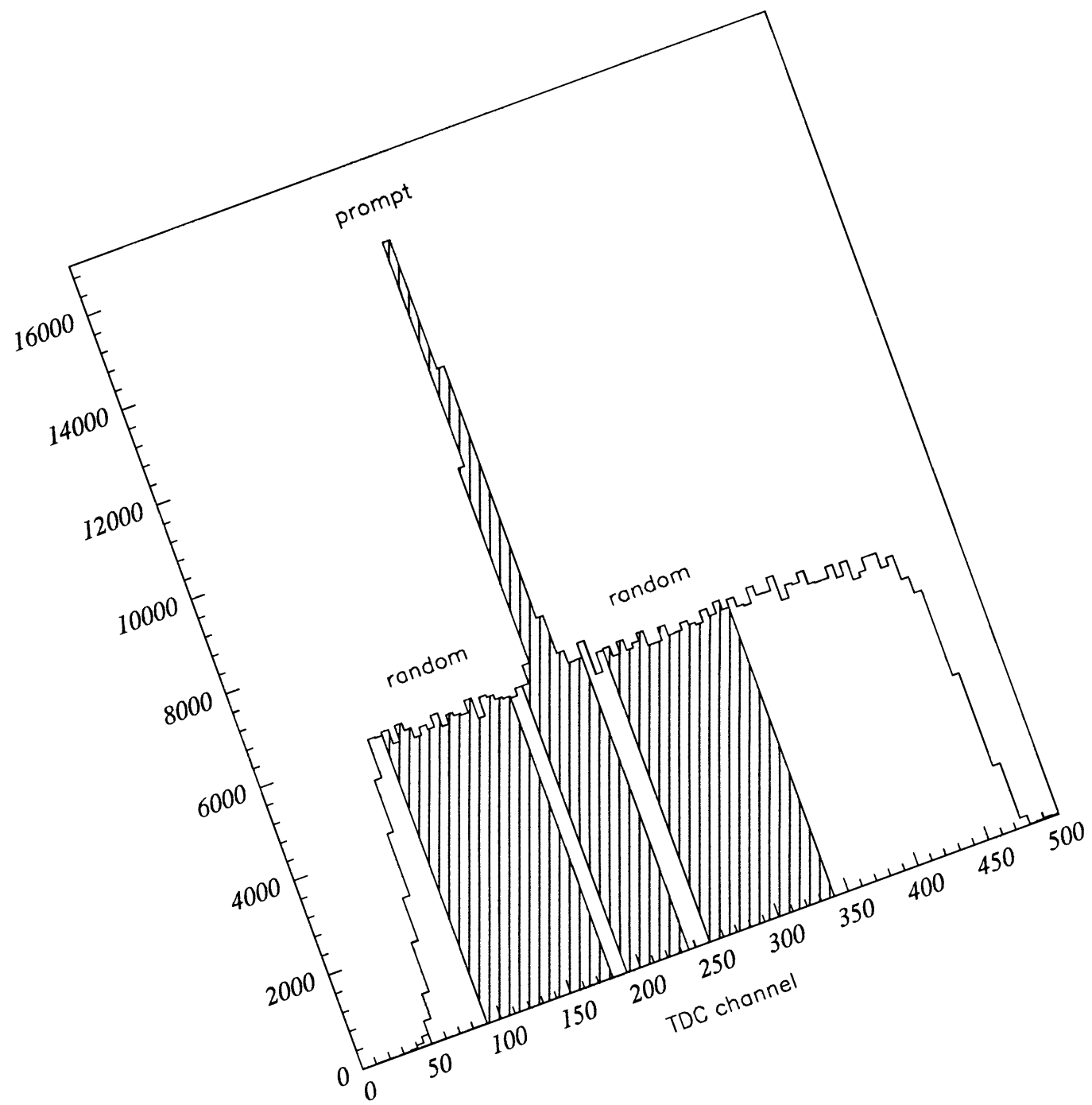


Figure 4.1: TAGGER TDC spectrum

the background continuum is not flat but exponential, and the component after the prompt peak is decreased by those events where the TDC is stopped by a prompt event before the random arrives. In this experiment the single channel rates were kept low enough to ensure that the background distribution is almost flat permitting the simple subtraction procedure described here.

Two sets of spectra were always generated in the analysis, one from the prompt region and one from the random. The subtraction of these spectra is discussed in the next section.

4.2.2 TOF

The fraction of randoms is small, $<5\%$, for the charged particles in TOF as the ΔE coincidence requirement is fairly rigorous and the particles' loci are well defined. The fraction of randoms is larger for the neutrons, $\sim 15\%$, as their loci are less well defined and neutrons cannot be distinguished from the dense region of low pulse height events caused by electromagnetic interactions (figure 3.2(b)). A software threshold of $\sim 4\text{MeV}_{ee}$ (4MeV equivalent electron energy) was set to reject these low pulse height events. This reduced the fraction of randoms to $\sim 6\%$ whilst only slightly reducing the neutron detection efficiency (section 4.4).

To account for the remaining randoms, data sets containing random events in TOF were generated. There is a separate data set for each reaction of interest generated using the plots shown in figure 3.2. The areas on these plots both before the γ flash (the time associated with a relativistic particle reaching the detector) or beyond the valid time range (times greater than the flight time of the slowest particle able to trigger the detector) have only genuinely random events. The random data sets were generated by defining cuts within either random area which were the same shape as the 'real' cuts, but compressed to fit the space available. As the 'real' events occupy most of the TDC range these regions have smaller areas and must be weighted appropriately leading to an increase in the statistical uncertainty. This does not present a problem in the present analysis as the fraction of randoms have been reduced by using a 4MeV_{ee} software threshold, but it could cause a problem if the analysis required information from stand A.

4.2.3 Yield Calculations

The yield is defined as the number of events left once all random subtraction have been made

$$yield = Y_1 - f_\gamma Y_2 - f_N Y_3 + f_\gamma f_N Y_4 \quad (4.1)$$

where Y_1 is the number of events which are prompt in both the TAGGER and TOF, Y_2 the number which are random in the TAGGER and prompt in TOF, Y_3 the number which are prompt in the TAGGER and random in TOF and Y_4 the number which are random in both the TAGGER and TOF, and f_γ and f_N are the appropriate weighting factors for the TAGGER and TOF randoms. The last term is required as the doubly random events are otherwise subtracted twice. The weighting factors are simply the ratio of the real to random time regions.

There is a fourth random component, which has been ignored in equation 4.1, due to events with a prompt TOF TAGGER coincidence but a random proton in PIP. This component was found to be negligible.

Figure 4.2 shows the relative sizes of these components for a typical proton energy spectrum from a $^{12}\text{C}(\gamma, pn)$ data set. The random events are much fewer than the prompt, and the largest component comes from randoms in the TAGGER. In (γ, pp) and $(\gamma, p\pi)$ reactions the TOF random component is smaller than for (γ, pn) reactions.

The inclusive yields do not require any information from the TOF detector. Therefore only two terms, similar to the first two in equation 4.1 but in which the yields solely refer to the TAGGER, are required for these measurements.

The yields of all data sets still contain the background events caused by interactions in air rather than the target. To correct for these events the above procedure was repeated using data generated with the target removed. The relative strengths of each target out contribution is similar to that of the target in data shown in figure 4.2. The target in and target out contributions after all the random subtraction have been made are shown together in figure 4.3, which again shows a typical proton energy spectrum from a $^{12}\text{C}(\gamma, pn)$ data set. This shows that the target out contribution is very small, typically $< 5\%$, but even so it was subtracted.

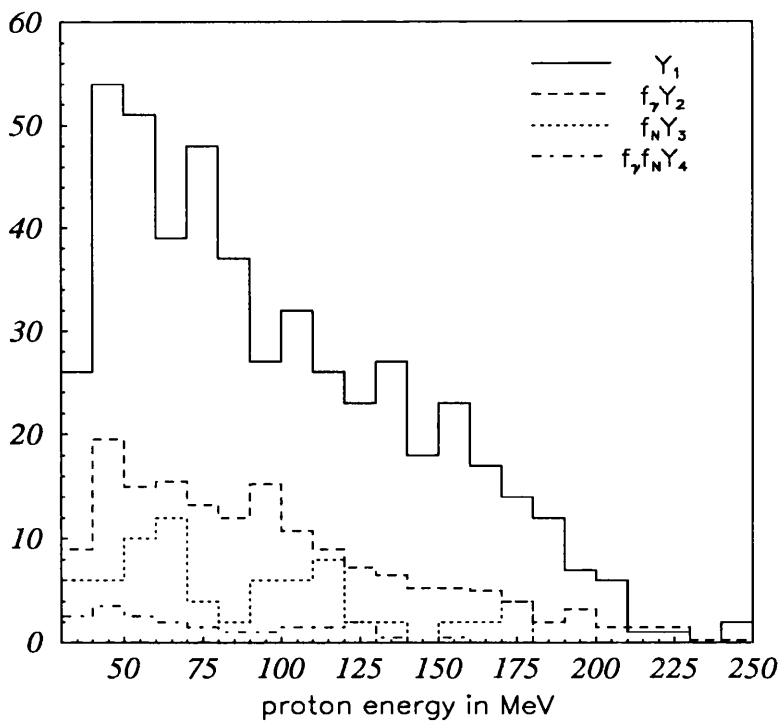


Figure 4.2: *Relative sizes of real and random components*

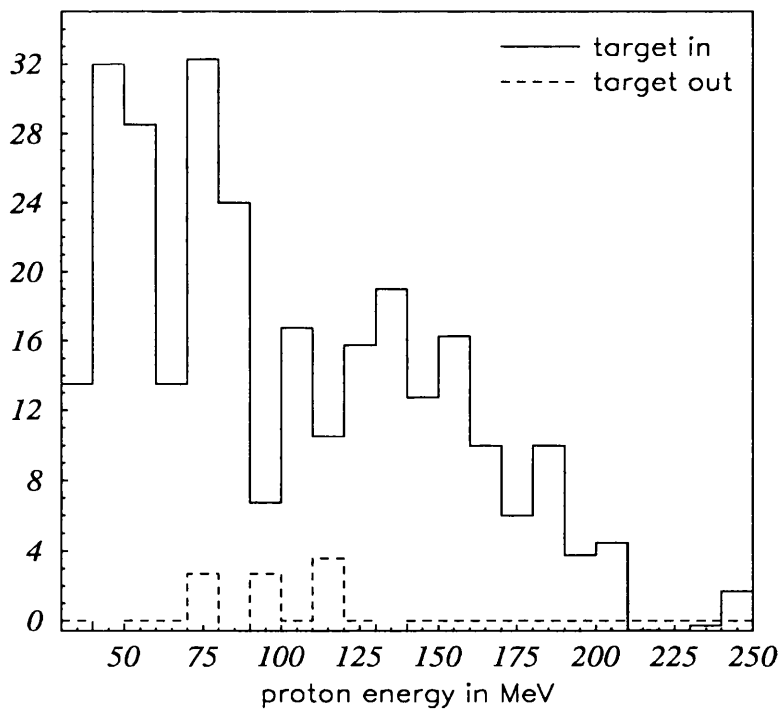


Figure 4.3: *Relative sizes of target in and target out components*

4.3 Cross Section Calculations.

The cross sections were calculated as a function of proton energy in PIP. The first spectra generated were inclusive (γ, p) where the proton was detected in PIP. The data are displayed as partial differential cross sections. These differential cross sections were calculated using the following expression.

$$\frac{d^2\sigma}{d\Omega_p dE_p} = \frac{yield \times 10^{30}}{\Sigma_{lad} \times \epsilon_t \times \Omega_p \times \epsilon_p \times n_{target} \times \Delta E_p} \mu b/sr/MeV \quad (4.2)$$

where *yield* is defined in equation 4.1, Σ_{lad} is the number of electrons in the relevant region of the focal plane, ϵ_t is the tagging efficiency expressed as a fraction, Ω_p is the solid angle bin size in sr, ϵ_p is PIP's proton detection efficiency again as a fraction, n_{target} is the number of target nuclei / cm² normal to the photon beam and ΔE_p is the proton energy bin width in MeV.

No dead time corrections were required as both the ADCs on PIP and the scalers on the TAGGER were gated off during the deadtime. Σ_{lad} was calculated from the contents of the scalers for those channels within the photon bin considered. The photon bins were all 20MeV wide. The measurement of the tagging efficiency is described below, a separate value was calculated for each photon energy bin. PIP's efficiency for detecting protons was assumed to be 1.0 above the energy detection threshold. The inclusive data were binned in 5MeV proton energy bins.

PIP's total solid angle was calculated as 964 ± 6 msr. However, to limit the range of angles considered, and thus enhance the features expected in the spectra, the data were split into four angular sets defined by the ΔE_2 element which was hit. The ΔE_2 elements are numbered 1 - 4 from upstream to downstream and have the following solid angles. The small asymmetry in the values is because PIP was placed slightly downstream relative to the centre of the target.

element	polar range	solid angle (msr)
1	128.5-112.0°	194
2	112.0-90.7°	283
3	90.7-69.2°	287
4	69.2-52.3°	200

Table 4.1: *Polar range and solid angle covered by each ΔE_2 element*

The number of target atoms was calculated from the following expression

$$n_{targ} = \frac{(\text{target thickness in g/cm}^2) \times N_A}{(\text{atomic mass in g}) \times \sin\theta_t} (\text{cm})^{-2} \quad (4.3)$$

where N_A is Avogadro's number and θ_t is the angle of the target to the beam. n_{targ} was calculated at $2.624 \times 10^{22} (\text{cm})^{-2}$ for the 1.5mm thick graphite target used.

The exclusive data, (γ, pn) , (γ, pp) and $(\gamma, p\pi)$, were also displayed as a function of proton energy in PIP. A similar expression to equation 4.2 was used to calculate the exclusive cross sections,

$$\frac{d^2\sigma}{d\Omega_p dE_p} = \frac{\text{yield} \times 10^{30}}{\Sigma_{lad} \times \epsilon_t \times \Omega_{PIP} \times \epsilon_p \times \epsilon_N \times n_{targ} \times \Delta E_p} \mu\text{b/sr/MeV} \quad (4.4)$$

where the symbols are as defined above with the addition of ϵ_N which is TOF's detection efficiency for the associated particle. This was assumed to be 1.0 for the charged particles. The detection efficiency is much smaller for neutrons, and the method of its calculation is discussed below. A larger proton energy bin size of 10MeV was chosen for the exclusive data because of the poorer statistics.

This expression neglects the solid angle of TOF since it intercepts a large fraction of the trajectories of the associated particle for both quasi-deuteron and quasi-free pion events. It is possible, in principle, to correct for the solid angle missed by the associated detector by using Monte Carlo simulations, see for example [20]. However, such calculations require the explicit use of the reaction mechanisms and as more than one mechanism competes at these energies this approach was not considered appropriate. The effect of the incomplete solid angle coverage of TOF is discussed in more detail in the next chapter.

The exclusive spectra were generated from data taken at different times and with different trigger requirements. These data sets had slightly different tagging efficiencies and so the factor $\Sigma_{lad} \times \epsilon_t$ was calculated separately for each photon energy bin in each data set.

4.3.1 Tagging Efficiency.

The tagging efficiency measurement is required to calculate the fraction of residual electrons counted by the scalers in the TAGGER focal plane which have an associated photon passing through the TAGGER collimator to hit the target (see section 2.2.4). It was measured using separate runs in which a Pb glass detector

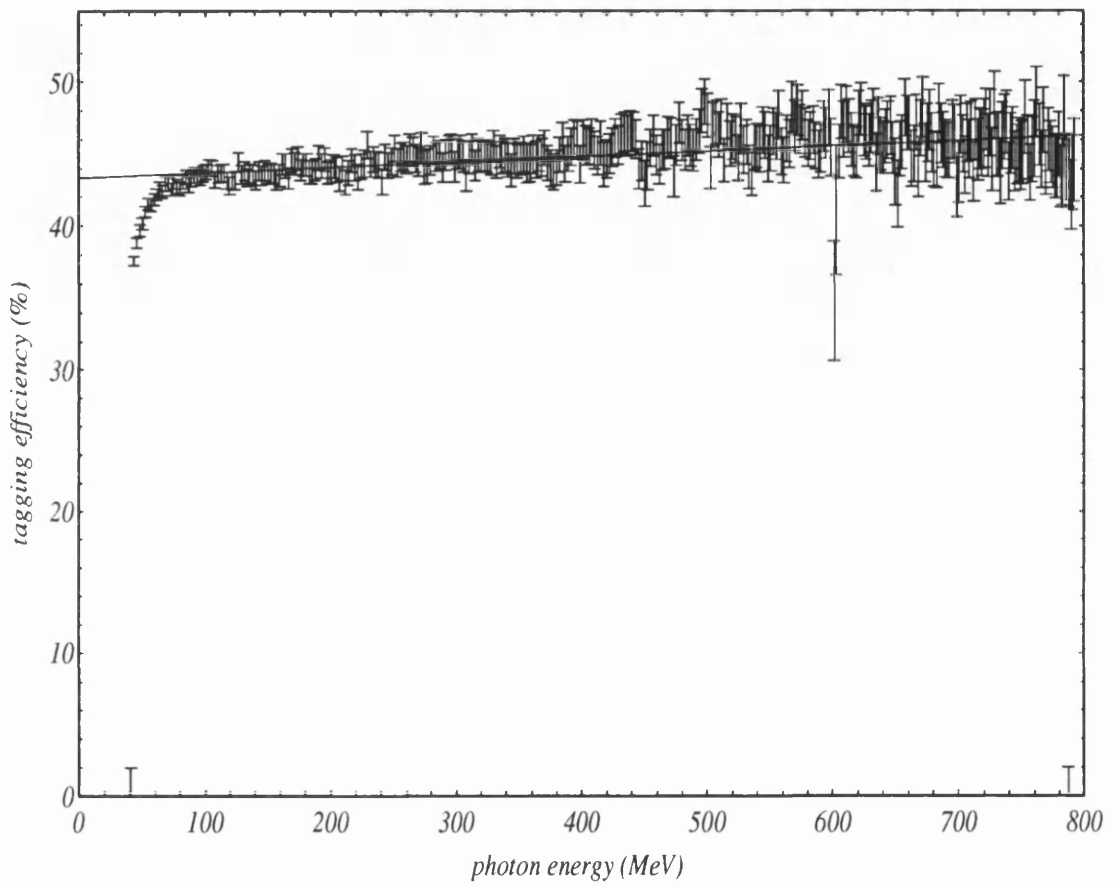


Figure 4.4: *Tagging efficiency as a function of photon energy*

placed directly in the photon beam and which also provided the event triggers. The tagging efficiency, as defined in equation 2.1, was calculated for each channel of the ladder detector by taking a ratio of the number of counts in each TAGGER TDC to the number of counts in the corresponding scaler. Figure 4.4 shows the tagging efficiency as a function of photon energy from a typical run. The efficiency is smoothly varying with photon energy to within the statistical errors except at low energies. Scatter plots of Pb glass QDC *vs* TAGGER channels showed that these low energy photons did not always trigger the detector discriminator. It was therefore decided to extrapolate the straight line fit to cover all energies as shown. There are also a number of dead channels and channels with significantly lower tagging efficiency. These were ignored as they all fell outwith the photon energy range of interest. Separate values were calculated for each photon energy bin considered using the value at the centre of the bin.

The overall tagging efficiency was found to be fairly constant at about 45% throughout the data taking period. This value is significantly lower than the 58% expected from a calculation which includes the effect of multiple scattering in the radiator but not the effect of divergence of the electron beam [83], [93]. It is thought that the low tagging efficiency resulted from slight misalignments in the collimators.

4.3.2 Neutron detection efficiency

Since neutral particles do not directly produce ionisation and excitation in scintillator but are instead detected by the signals produced by the charged particles they knock-out along their passage. Therefore a neutron will only be detected if it knocks out charged particles of sufficient energy to trigger the detector. This results in a lower detection efficiency for neutrons which is both a function of incident energy and detector threshold.

The average neutron detection efficiency was calculated using the STANTON code [86]. The results are shown as a function of neutron energy in figure 4.5 for two different detector thresholds. In the present experiments the hardware thresholds were kept at a minimum, $< 1\text{MeV}_{ee}$ for charged particles, but were raised in the software to 4MeV_{ee} for neutrons to reduce background contributions (see section 4.4.2). For this purpose the response of the TOF scintillator was taken from [94] normalised to the proton punch through point at $\sim 79\text{MeV}$. The uncertainty in the threshold from this rough calibration is $\sim \pm 0.5\text{MeV}_{ee}$.

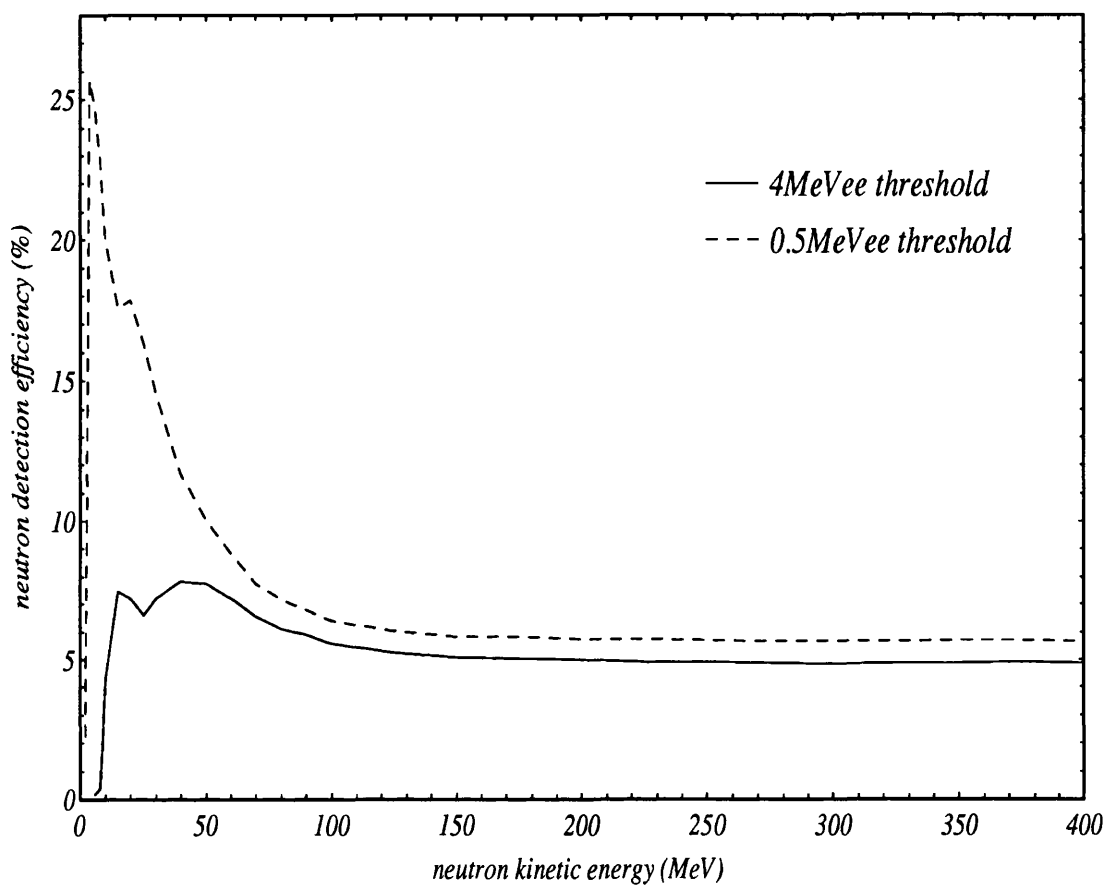


Figure 4.5: Neutron detection efficiency as a function of neutron energy

The neutron detection efficiencies for both thresholds are included in figure 4.5. The (γ, pn) data presented in this thesis is integrated over neutron energies and an average value of ϵ_n was used for the cross section calculations. As the neutron energy distribution is not flat, but peaks at low energies, a weighted average was calculated. The expected neutron energy distribution was obtained from the Monte Carlo simulation code PICA (see section 4.5) for several incident photon energies. The average detection efficiency obtained for these neutron energy spectra is 6.6%, and did not vary significantly with the different photon energies, and this value was used in equation 4.4.

4.4 Statistical and Systematic Uncertainties

The proton energy spectra are shown in chapter 5 with only the statistical uncertainties from the determination of the yield indicated. The other factors used in calculating the cross sections also have associated uncertainties common to all spectra. These systematic uncertainties fall into two categories.

The first category consists of the uncertainties due to the precision in the measurements; their contributions are estimated below.

- The factor Σ_{lad} has an associated statistical error. However, as the value of Σ_{lad} was consistently greater than 10^{10} its contribution to the overall uncertainty was negligible and was therefore ignored.
- Figure 4.4 shows the magnitude of the uncertainty in calculating ϵ_t . The value of $\sim 4\%$ displayed reflects the statistics from a typical single run for a single TAGGER channel. A value of 1% was obtained by averaging over a number of files and over the 20MeV photon energy bins used in the analysis.
- The calculations of the solid angle have an associated error arising from the uncertainty in the determination of the position of PIP. It is estimated that the measurement of the position of PIP relative to the target is accurate to $\pm 2\text{mm}$ in each dimension resulting in uncertainties of the order 1%. There is an additional uncertainty due to the extended beam spot on the target, but this was found to be insignificant compared to the error from determining the position of PIP and was therefore ignored.
- The determination of n_{targ} also has an uncertainty. This is due to the errors in estimating both the thickness of the target and its angle. The thickness

of the target was calculated from the ratio of the area of the target face to its mass, with an uncertainty of 0.7%. The target angle was set using the computer controlled target ladder. Tests showed that there was a negligible error in rotating the ladder through a fixed angle, leaving only the ladder alignment as a source of uncertainty. Its contribution was estimated at 0.2° resulting in an overall uncertainty of $\sim 1\%$ in n_{targ} .

- The authors of the STANTON computer code [86] found that its results matched experiment to within a few percent. However, the estimation of neutron detection efficiency has an uncertainty due to the indeterminacy in measuring the software threshold. The error of $\pm 0.5\text{MeV}_{ee}$ leads to an error of $\sim 5\%$ in the weighted average efficiency. Assuming that STANTON is also accurate to within $\sim 5\%$ results in an indeterminacy of 7% in ϵ_n .

The total systematic uncertainty was estimated at $\sim 1.5\%$ for the inclusive measurements and is similar to the statistical uncertainty in the yields. The (γ, pp) and $(\gamma, p\pi)$ measurements have the same systematic uncertainty which is smaller than their statistical uncertainties ($\sim 5\%$). However, the systematic uncertainty increases to $\sim 7.5\%$ for the (γ, pn) measurements due to the uncertainty in the neutron detection efficiency. This is still smaller than the statistical uncertainty of $\sim 12\%$ for (γ, pn) reactions.

The uncertainties discussed above reflect the overall precision in the measurements. There is a second source of experimental error caused by limitations in the measurement techniques which cannot be reduced by increasing the precision of the measurement. The charged particle detection efficiencies fall into this category. Charged particles cause ionisation along their tracks causing the plastic to scintillate and the integral of the scintillation light along the track gives a measure of the energy deposited within the scintillator. However, the track may be shortened, and hence the energy will be underestimated, if the particle loses energy by inelastic processes. The effect of these losses does not affect the total number of particles detected, but rather increases the number of low energy particles to the expense of the high energy particles. These processes have been studied by Measday and Richard-Serre [70] and their results suggest that about 3.3% of 50MeV protons detected in plastic scintillator will be affected rising to 26% for 200MeV protons and 60% for 400MeV protons. For this reason only those events with protons stopping the first two layers of PIP are considered in

the present work and no corrections are attempted. However, this introduces an uncertainty of up to 26% at high proton energies which could have been corrected by dividing each proton energy bin by the appropriate peak efficiency.

There are similar systematic uncertainties in the TOF detector. For example, it is possible to estimate the number of charged particles lost due to nuclear interactions in air before they reach TOF by Monte Carlo simulation. However, no such corrections were attempted in this first stage of analysis as they do not grossly affect the main features of the proton energy spectra and the results are good enough for a first comparison with a simple theoretical model (PICA).

4.5 Theoretical Simulations.

The theoretical comparison was mainly provided by the Monte Carlo simulation PICA written by Gabriel and Alsmiller [95]. In it the photon is assumed to interact with the nucleus via the quasi-deuteron mechanism or by quasi-free pion production on a nucleon. The emitted particles are then followed through the nucleus, with final state interactions being included via an intranuclear-cascade model.

The calculation uses a nucleon density of the same shape as the charge density derived from electron scattering data. It approximates this density distribution by splitting the nucleus into three concentric spheres each of uniform density and assumes that the proton-neutron density ratio is constant throughout the nucleus. A binding energy of 7MeV is assumed for the most loosely bound nucleons, the depth of the potential for nucleons then being the appropriate Fermi energy plus 7MeV. The pion potential is assumed to be equal to that of the nucleon with which it is interacting.

The quasi-deuteron contribution is calculated using Levinger's parameterisation of the cross section [2] (see equation 1.4). The deuteron cross section in the energy range considered here was obtained from the average of the experimental data available in 1969. Recent deuterium measurements with tagged photons agree with these early results [96], and therefore there is no significant error introduced from this source. PICA assumes that the proton and neutron forming the quasi-deuteron were both initially in the same region in the nucleus. This simplifies the calculation, but slightly modifies the definition of the Levinger parameter due to the renormalisation required to ensure that the number of pn pairs is equal to NZ . The original calculations used a Levinger parameter $L = 10.3$ derived

from the work of Garvey *et al* [14]. Following initial comparisons between the data presented here and PICA it was found that this value of L overestimated the quasi-deuteron contribution and the present work uses a value of 4.1. The choice of the value of the Levinger parameter is discussed in more detail in the next chapter.

The quasi-free pion production calculation uses the cross section for the free photon-proton reaction, the cross section for the neutron being obtained from charge symmetry calculations. PICA only models single pion production and has limited usefulness for photon energies above $\sim 350\text{MeV}$. The interaction is modelled assuming that the pions are emitted isotropically in the centre of mass frame, and the free cross section is modified to account for Pauli blocking and the effect of the nuclear potential.

Once the primary interaction has been determined the reaction products are followed through the nucleus with final state interactions being modelled using free particle-particle cross sections. Nucleon-nucleon and pion-nucleon scattering, charge exchange and pion absorption are all considered. PICA checks that the reaction is allowed by the Pauli principle and products whose energies are greater than the Fermi energy are followed through the nucleus until they are emitted. Products whose energy is less than the Fermi energy are assumed to be no longer free and their energy is shared by all the remaining nucleons. The code also allows for the de-excitation of the residual nucleus by an evaporation process. However, since the emitted particles are too low in energy to trigger the detectors in the present experiment this part of the calculation was not used.

PICA can be run using either a monochromatic or a Bremsstrahlung photon source. To minimise the number of events required a monochromatic photon source was used to generate a separate data set for each experimental photon bin using an energy equal to the central energy of the experimental photon bin. The code outputs the particle type, energy and direction cosines of each reaction product and a simple program was written to read in this data and output proton energy spectra for the various reactions studied taking account of the detector acceptances. Particle thresholds of 10MeV for neutrons, 30MeV for protons and 15MeV for charged pions were also included, these were estimated from average particle ranges and energies and were slightly low as they ignore the small discriminator threshold on TOF. No upper energy threshold was included. This inclusion of the detector acceptances in the theoretical model ensures that any effects due to incomplete coverage by TOF are present in both the experimen-

tal and theoretical spectra allowing a proper comparison between the two. As both the data and theory suggest that the peaks in the proton energy spectra are much broader than the experimental resolution no modelling of the detectors' resolution was attempted.

Simulated data sets for the inclusive (γ, p) reaction channel and the exclusive (γ, pn) , (γ, pp) and $(\gamma, p\pi^\pm)$ reaction channels were generated for each of the photon bins considered. Each data set was generated using $10^8 - 10^9$ incident photons resulting in a statistical accuracy better than that of the experimental data. The yield from PICA was converted into differential cross sections by dividing out the incident number of photons, the solid angle of the relevant ΔE strip and the proton energy bin size. This output from PICA was then used to compare with the experimental data.

A typical example of the output from PICA is shown in figure 4.6. This shows the $^{12}\text{C}(\gamma, p)$ cross section at $60^\circ \pm 10^\circ$ for an incident photon energy of 300MeV and does not include the effects of the upper and lower proton energy thresholds. All of the expected features are apparent in this spectrum, and the output from PICA is split into QD and QFPP components to aid the discussion. The QD component is fairly small by 300MeV, but is still visible and rises to a peak at $\sim(E_\gamma - S_{2N})/2$, where S_{2N} is the separation energy for the $^{12}\text{C}(\gamma, pn)$ reaction, as expected from the reaction kinematics. However, the QFPP component is near its maximum at this photon energy and generates a large peak at low proton energies. This is again expected from the reaction kinematics as the mass of a pion must be provided in this channel. It is evident from this spectrum that most of the QFPP component will be suppressed by the $\sim 40\text{MeV}$ proton energy detection threshold. A full comparison between PICA and the present experimental data is made in the next chapter.

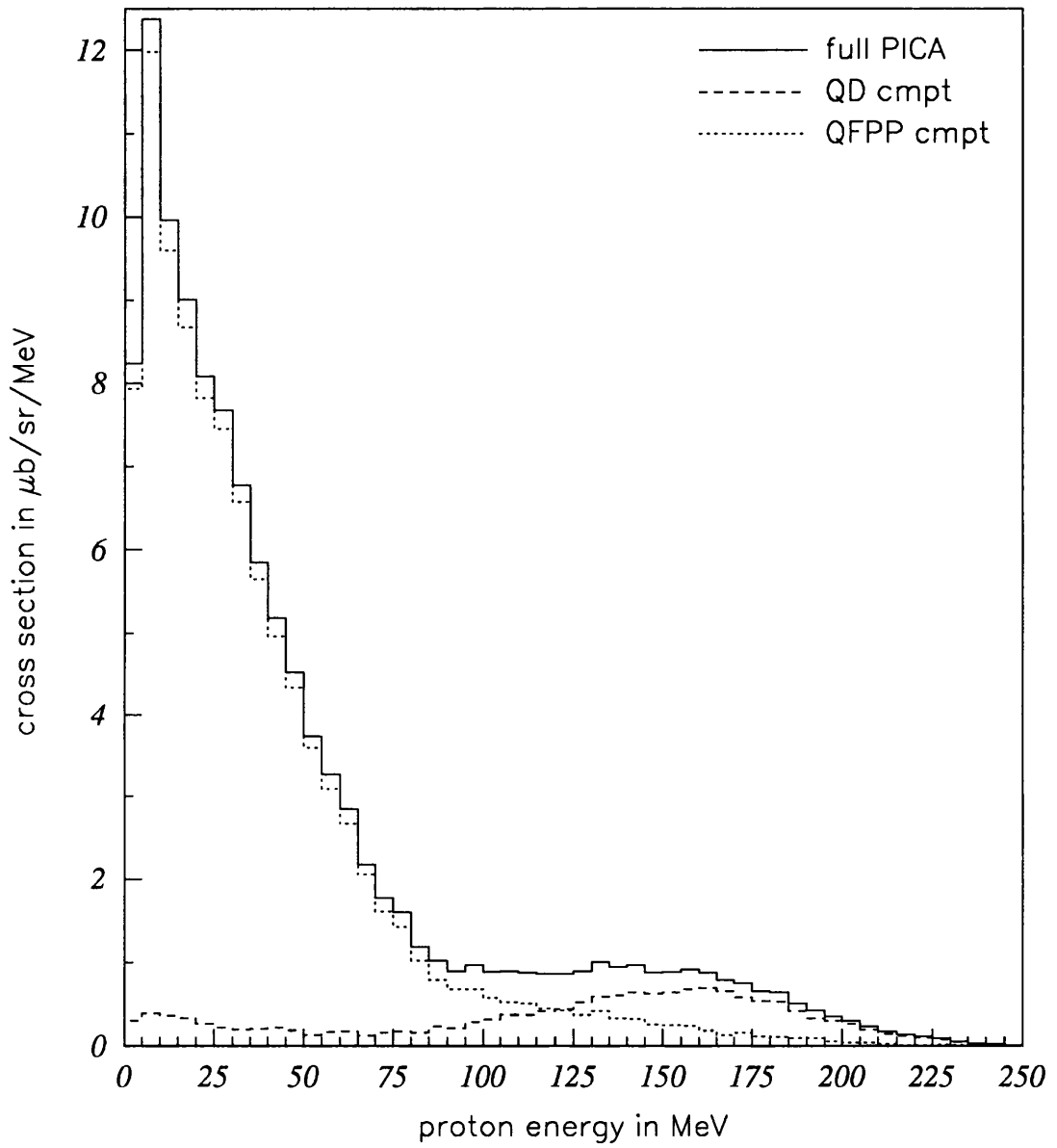


Figure 4.6: An example of a $^{12}\text{C}(\gamma, p)$ simulated cross section

Chapter 5

Discussion and Conclusions

Introduction

The data from the inclusive (γ, p) reaction channel and the exclusive (γ, pn) , (γ, pp) and $(\gamma, p\pi)$ reaction channels are presented in the form of partial differential cross sections as a function of proton energy. The present data are compared to a number of previous measurements, [26],[29],[97]. A theoretical comparison to the data is provided by the intranuclear cascade code PICA [95] and some further comparisons are also made with the newer microscopic models, [38],[47]. Conclusions about the present measurements and their theoretical interpretation are drawn, and the performance of the new detector PIP is assessed.

5.1 Comparison with Previous Experiments

There are a small number of previous tagged photon measurements to which the present data can be compared, [27],[29],[26],[97]. However, such comparisons are fairly limited as none of these measurements are as extensive as the present study and do not cover as large a photon energy range or as large an angular range as the present experiment. Furthermore there is a very limited range of exclusive measurements to provide a comparison to the present work.

5.1.1 Inclusive Measurements

The (γ, p) inclusive cross section has previously been measured as a function of proton energy at a number of photon energies and angles at Bonn, Tokyo and Frascati. These measurements are discussed in detail and compared with the present measurement in figures 5.1 and 5.2 below.

Arends *et al* have measured the $^{12}\text{C}(\gamma, p)$ cross section in two separate tagged photon experiments at Bonn, one in 1980 [27] and the other in 1991 [29]. In both experiments the cross section was measured at photon energies between 200 and 400MeV and the proton was detected in a magnetic spectrometer. In the first experiment a carbon target was used and the spectrometer was set at several angles in the range 44° and 130° , in the second several targets were studied at a fixed angle of $52^\circ \pm 6^\circ$. Exclusive cross sections were also measured in these experiments, and are compared to the present data in the next section.

Two different groups at the tagged photon facility at INS in Tokyo have measured the $^{12}\text{C}(\gamma, p)$ cross section. The work by Homma *et al*, [23], [24], [25], is discussed in Chapter 1, but is not used for comparison here as their proton

detector was set at 30° , outwith the range of the present measurements. Baba *et al* [26] measured the cross section from ^9Be and ^{12}C targets using tagged photons of energy 360-600MeV. The protons were detected in a magnetic spectrometer set at 23° , 55° and 130° . The cross sections were presented as a function of proton momentum, and were therefore converted into proton energy space for comparison to the present data. The cross sections measured at forward angles agree with those measured by Homma *et al*.

Some inclusive cross sections have also been measured using the LEALE photon beam at Frascati [97] with the aim of bridging the gap between the earlier measurements performed at Mainz and those performed at Tokyo and Bonn. This facility produces a photon beam using the positron annihilation method, and therefore requires positron Bremsstrahlung subtraction. The $^{12}\text{C}(\gamma, p)$ cross section was measured at photon energies of 159 and 198MeV and the protons were detected simultaneously by 5 ΔE -E scintillator telescopes which were placed at 32.5° , 55° , 80° , 105° and 130° to the photon beam.

Figure 5.1(a) shows the comparison between the present (γ, p) data, the Frascati data and the Bonn data from 1991. The incident photon energies are all close to 200MeV and the proton is detected at angles close to 60° . In these comparisons with various previous measurements, and in the subsequent comparisons with theory, it should be remembered that the present data have not been corrected for the inelastic losses discussed in section 4.4. The effect of these losses is to systematically feed yield from high proton energies to low proton energies, therefore decreasing the cross section at the highest proton energies by up to 25%. There is no evidence of the two peaked structure discussed in the previous chapter since at this photon energy the quasi-free pion production mechanism cannot provide protons of sufficient energy to trigger PIP.

The present data agree well with that from Frascati except at the lowest proton energies. This is not unexpected since the cross section from positron annihilation is most sensitive to the positron Bremsstrahlung subtraction at these low energies. The agreement between the present data and the Frascati data at high proton energies is expected since both experiments used scintillator detectors and are therefore both sensitive to inelastic losses. On the other hand, the Bonn data have a cross section which is larger by a factor of between 3 and 4. Although their angular and photon energy bins are slightly different to the present experiment, the difference is too small to seriously affect the comparison. The Bonn data do, however, have a similar shape to the present data.

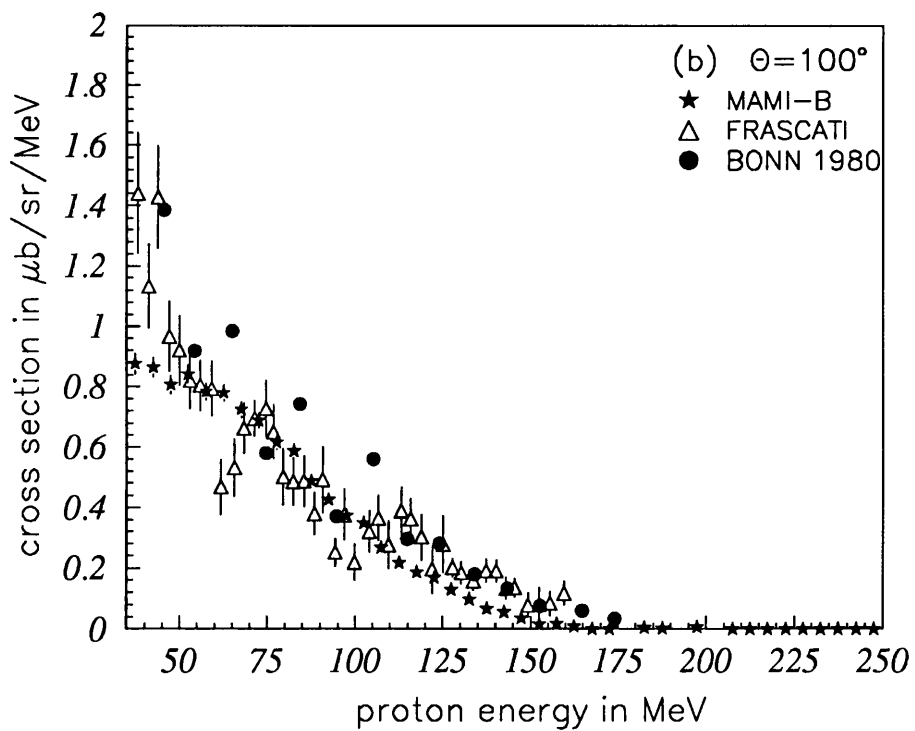
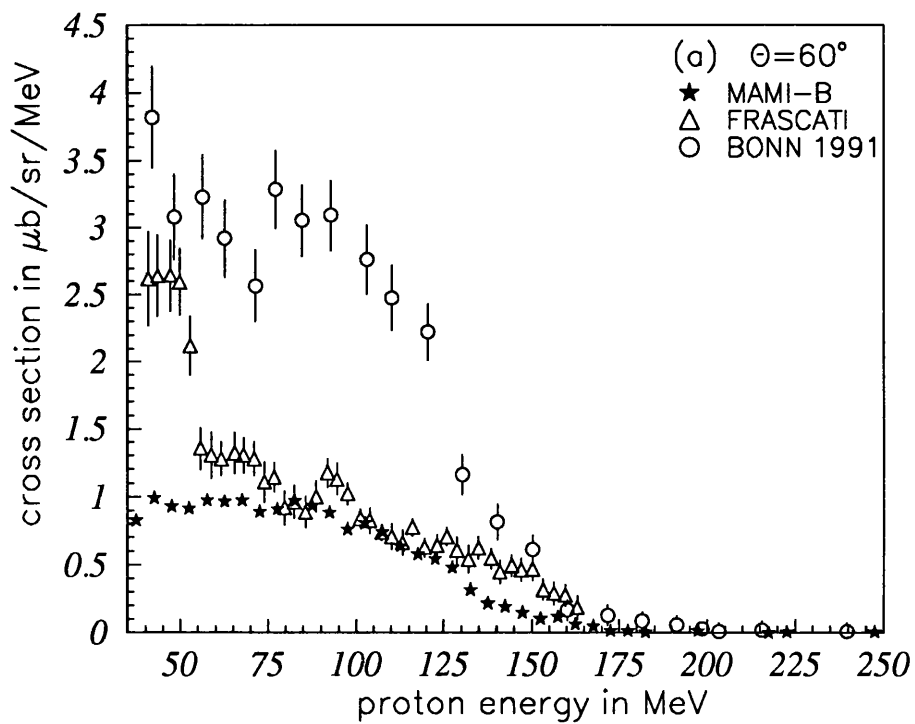


Figure 5.1: The (γ, p) cross section at $E_\gamma \sim 200\text{MeV}$

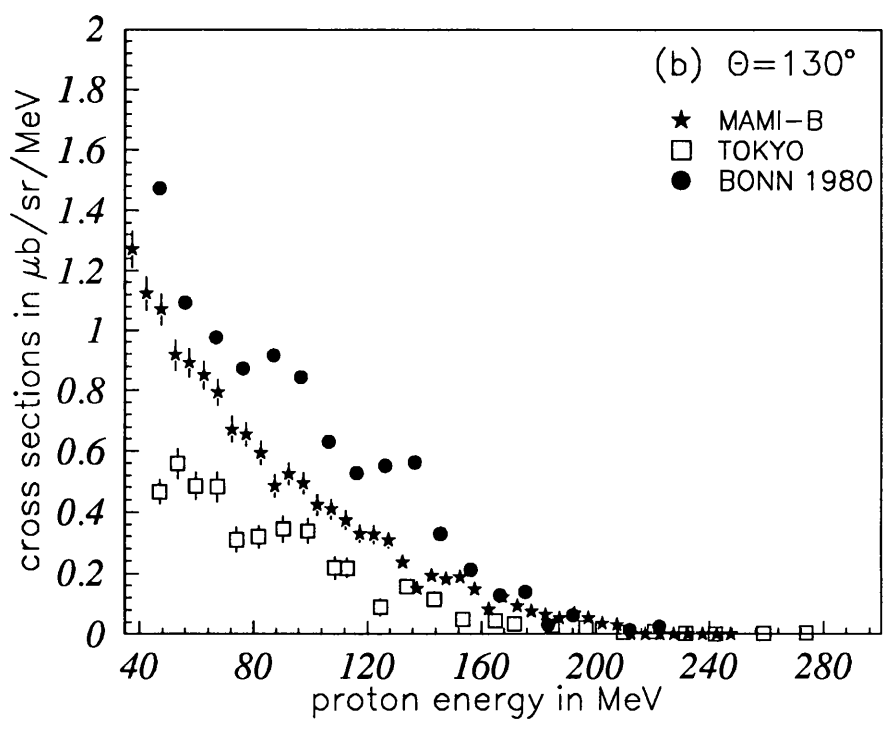
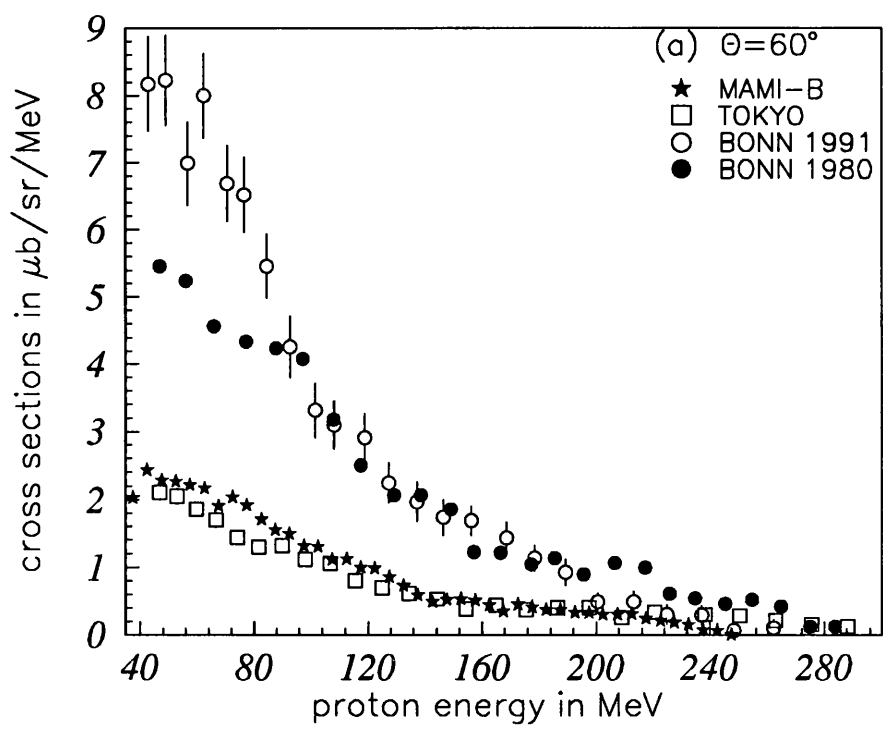


Figure 5.2: The inclusive (γ, p) cross section at $E_\gamma \sim 400 \text{ MeV}$ and $\theta_p \sim 60^\circ$

The data from Frascati and the 1980 Bonn data are compared to the present data at a backward angle in figure 5.1(b). The incident photon energy was again $\sim 200\text{MeV}$ and the protons were detected at $\sim 100^\circ$ in both experiments. The spectra are again fairly featureless as the cross section is almost entirely due to the quasi-deuteron mechanism. There is now good agreement among all three sets of data, except at low proton energies for the reasons discussed previously.

Figure 5.2(a) shows a comparison between the present data and the data from Tokyo and both Bonn experiments at $\sim 400\text{MeV}$ incident photon energy and at $\sim 60^\circ$ proton detection angle. At this higher photon energy the quasi-free pion production mechanism is dominant providing the large cross section at low photon energies, the long tail evident on all data sets indicates that the quasi-deuteron mechanism is still contributing at these higher photon energies.

The present data and that from Tokyo agree in both shape and magnitude, if account is taken of the effect of the upper proton energy threshold in PIP and the effects of inelastic losses at high proton energies. Correcting for these losses would tend to increase cross section of the present data at high proton energies while slightly decreasing it at low proton energies thus improving the agreement between the two data sets. Neither set of data from Bonn agrees in magnitude with the other two measurements although the shapes are fairly similar, except at low proton energies where there is a significant discrepancy which is likely to be due to differences in the treatment of the data in the magnetic spectrometer during analysis [98].

Figure 5.2(b) shows a comparison between the present data and the data from Tokyo and the 1980 Bonn experiments again at $\sim 400\text{MeV}$ incident photon energy but at a backward angle proton detection angle of $\sim 130^\circ$. The quasi-free pion production mechanism produces heavily forward peaked protons, so the majority of the cross section at this angle is provided by the quasi-deuteron mechanism. The resulting spectra are therefore fairly featureless, just consisting of the tail of the QD distribution.

Both of the earlier data sets show some agreement in magnitude with the present results, the Bonn data being somewhat larger and the Tokyo data somewhat smaller. The shapes are also in agreement, although only the present data have sufficient statistics to produce a relatively smooth distribution.

This comparison between the present and previous data gives confidence in the present work. The present data agrees with both that of Baba *et al* and Anghinolfi *et al* over a range of photon energies and proton detection angles. The

data of Arends *et al* also shows reasonable agreement with the present data at backward angles, but is considerably larger than all the other data sets at forward angles. The reason for this discrepancy is not clear.

5.1.2 Exclusive Measurements

Both of the sets of data published by Bonn which were discussed in the previous section include coincidence data. Unfortunately, the earlier data [27] use a restricted angular range in the associated particle detector to enhance the features of the QD and QFPP reactions, and is therefore not suitable for a direct comparison with the present data.

The later Bonn data were obtained with the proton detector at $52^\circ \pm 6^\circ$ and the time-of-flight spectrometer used to detect the associated particle covering $\sim 10^\circ$ - 140° . This is very similar to the present detector geometry. However, there is a large difference in the azimuthal coverage of the two detector systems. The Bonn time-of-flight spectrometer has an azimuthal opening angle of $\sim 35^\circ$ which matches the $\sim 10^\circ$ opening angle of the magnetic spectrometer. On the other hand, PIP has an azimuthal opening angle of 44° compared to 14° - 23° in TOF, which will therefore not intercept the trajectories of all the associated particles. The present cross sections were therefore multiplied by a factor of 3 to roughly remove the effect of the lost particles in TOF. This makes the assumption the emitted particles are approximately coplanar with only a small spread in azimuthal opening angle due to the initial Fermi momentum, as would be expected from a simple QD model. However, if there is a large azimuthal opening angle a factor closer to 1 would be more appropriate.

The Bonn exclusive cross sections were obtained using an ^{16}O target. However, the cross sections have been shown to vary slowly with A [29], differences being $\sim 10\%$ rather than 25% as predicted by Levinger [2] and QFPP calculations. Therefore comparisons between this and the present ^{12}C data should be feasible.

The cross sections, after renormalisation of the present data, are shown in figures 5.3 and 5.4 for incident photon energies of 300 and 400MeV respectively. The two data sets agree fairly well for all reaction channels both in magnitude and in shape at both incident photon energies. This may be fortuitous, however, given the roughness of the renormalisation of the present data, the slightly different detector geometries, and the different target nuclei.

The agreement between the exclusive cross sections obtained from present

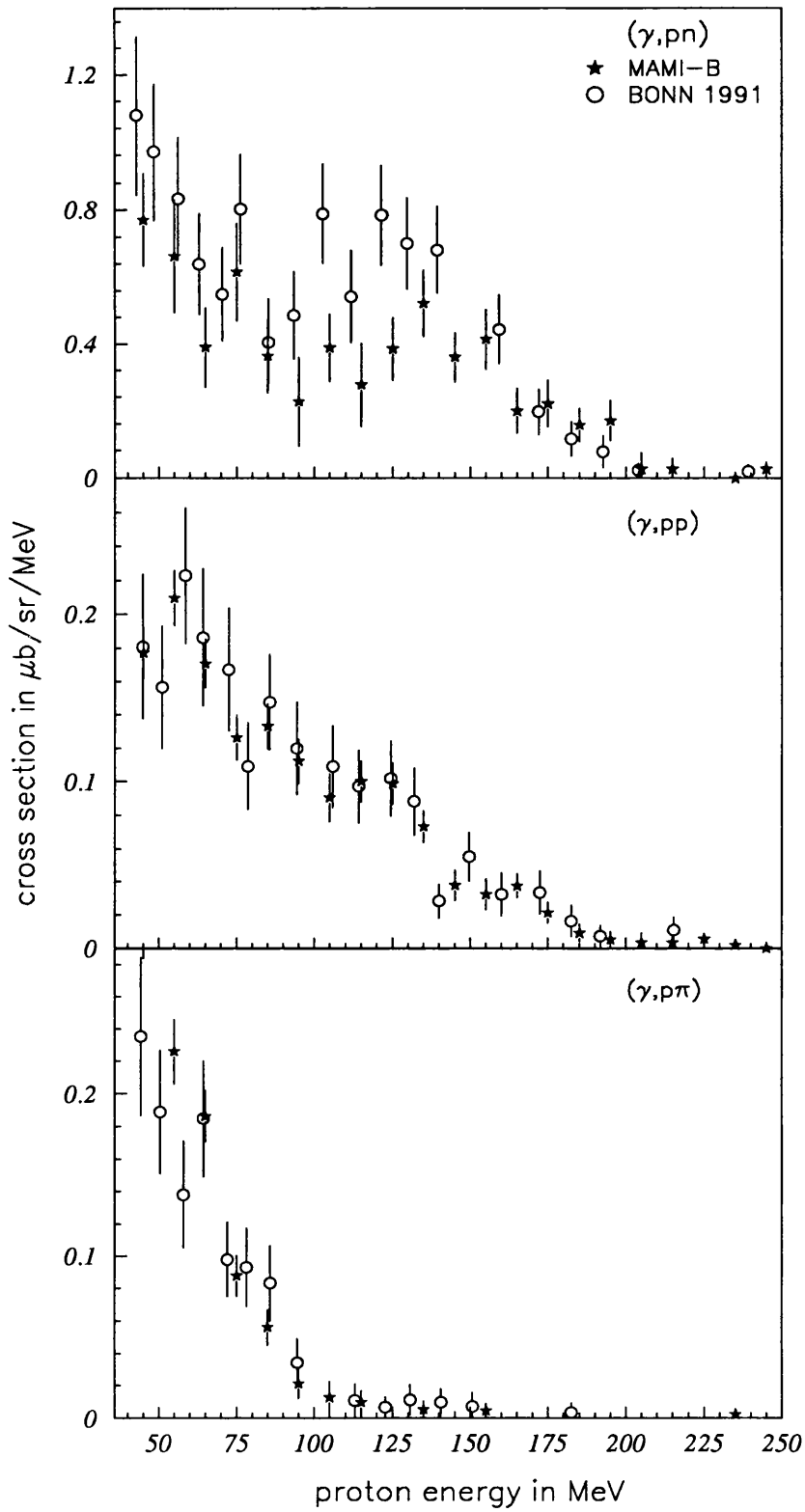


Figure 5.3: Renormalised exclusive cross sections at $E_\gamma \sim 300\text{MeV}$ and $\theta_p \sim 60^\circ$

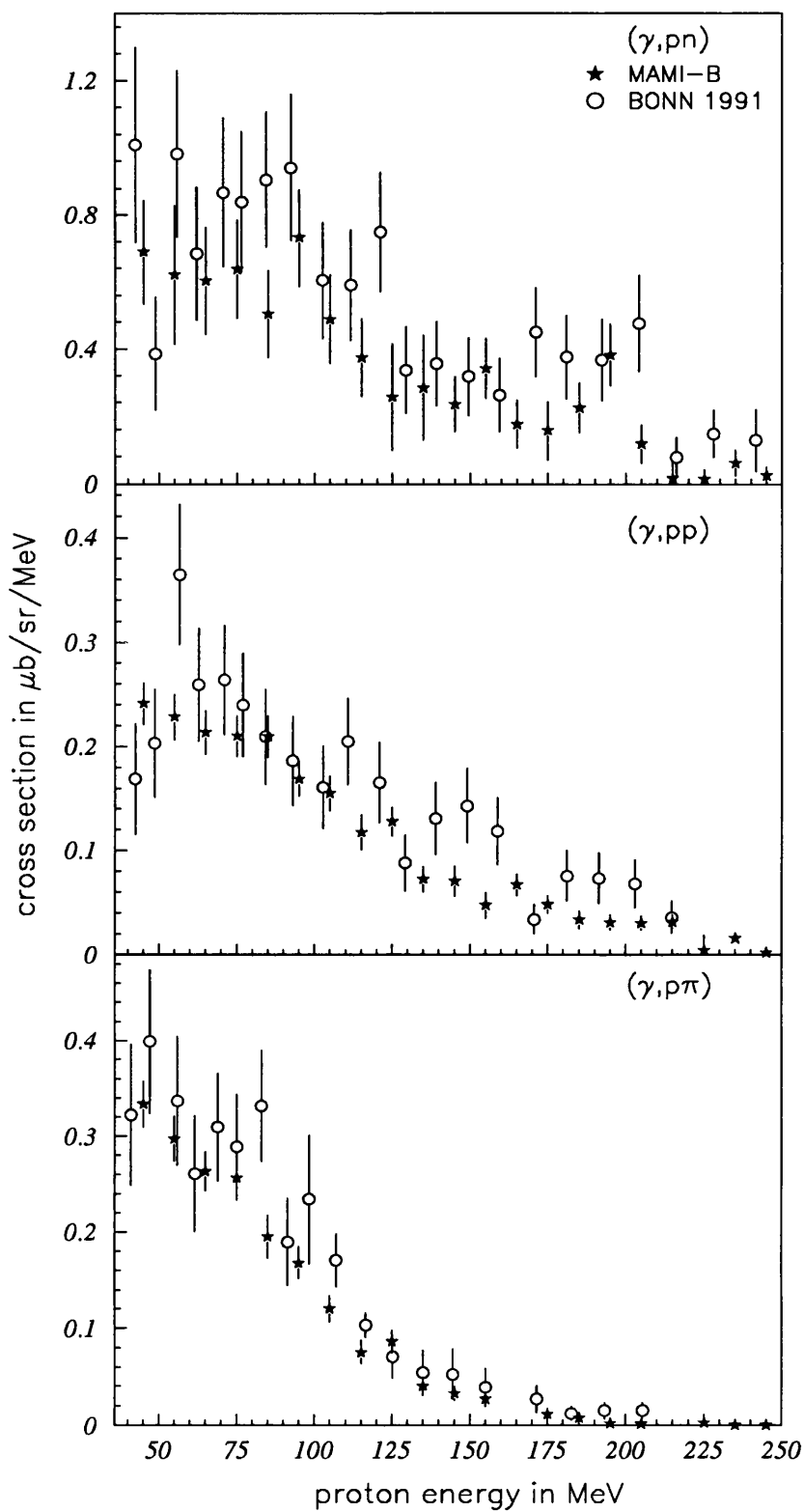


Figure 5.4: Renormalised exclusive cross sections at $E_\gamma \sim 400\text{MeV}$ and $\theta_p \sim 60^\circ$

data and that from Bonn is puzzling given the disagreement in the inclusive cross sections at forward angles. However, the ratios of (γ, pn) to (γ, p) cross sections are instructive. In the data obtained at 400MeV incident photon energy for proton energies above 150MeV the present data has a ratio of almost 1 (once the solid angle of TOF is accounted for) whereas the Bonn data has a ratio of approximately 0.4. Since the inclusive (γ, p) cross section should be mainly due to the quasi-deuteron process under these kinematic conditions the ratio is expected to be ~ 0.8 due to the effects of FSI on the correlated neutron [99] again providing credence to the present result.

In the two sets of data the (γ, pn) cross section shows evidence of both the quasi-deuteron and quasi-free pion production mechanisms at both photon energies. The $(\gamma, p\pi)$ cross section falls off far more rapidly with proton energy than either of the other channels, as expected since it is exclusively generated by quasi-free pion production. In contrast, the (γ, pp) cross section falls off less rapidly than the $(\gamma, p\pi)$ but does not have the clear structure of the (γ, pn) , and subsequent comparison with theory verifies that this reaction channel is the most difficult to understand.

Although this comparison between the present and previous data does not provide much additional information about the underlying physics, it is nevertheless instructive about the detector performance. The degradation of proton energy caused by inelastic collisions was discussed in section 4.4, and is expected to affect $\sim 26\%$ of protons of 200MeV. However, as this simply redistributes the affected protons towards lower proton energies the effect has little consequence on the shape of the proton energy spectra, as is suggested by the similarity between the present and previous results. Therefore including the E3 and E4 layers should be feasible, and should improve the comparison between the data and theory by increasing the upper proton detection threshold.

5.1.3 Checks on Experimental Cross Sections

Before any detailed discussion of the experimental data was attempted an independent analysis was carried out to check the overall normalisation of the cross sections. The CD_2 data, which had been taken to obtain energy calibrations of the detectors, was used to evaluate the $D(\gamma, p)$ cross section between 50 and 400MeV [100]. In this process the carbon background was subtracted off using data taken with the ^{12}C target. The results were compared to the parameterisations of the

deuterium cross section by Rossi *et al* [101] and Jenkins *et al* [102]. The cross section obtained from the present data agrees with the two parameterisations to within their quoted errors.

The $^{12}\text{C}(\gamma, p)$ cross section was also checked by an independent analysis of a sample of the data [100] using a different version of the analysis program. The results agree well with the cross sections reported in this thesis.

5.2 Comparison between the Data and Theory

The improved quality data provided by recent tagged photon measurements have prompted various groups to readdress the theory behind intermediate energy photonuclear reactions in complex nuclei. Most of these new models are still in preliminary stages, or are designed to examine a particular aspect of the cross section. It was therefore decided to compare the present data to the intranuclear cascade code PICA [95]. Although PICA is a phenomenological calculation it should provide help here in fully assessing the contribution of the QD and QFPP mechanisms to the measured cross sections. PICA has also provided a useful interpretation of previous photonuclear data [26],[29]. Limited comparison between the present data and new microscopic theoretical models [38],[47] is also attempted.

Performance of PICA

As an independent check of how well PICA can describe photonuclear interactions at intermediate energies, the total absorption cross section calculated by PICA was compared to an experimental ^{12}C cross section measurement [103]. The experiment used the photohadronic technique which involves counting the photoreaction products, and can reliably identify and reject the large electromagnetic background from atomic processes. This total absorption measurement provided one of the data sets used to define the ‘Universal Curve’ [1] and compares well with other data sets obtained by other measurement techniques and from other nuclei. The results are shown in figure 5.5. PICA predicts the gross features of the data at all energies, but detailed comparison indicates that there are a number of important differences which are discussed below.

Below the pion production threshold the cross section is exclusively due to the quasi-deuteron process, hence comparison between PICA and the total absorption

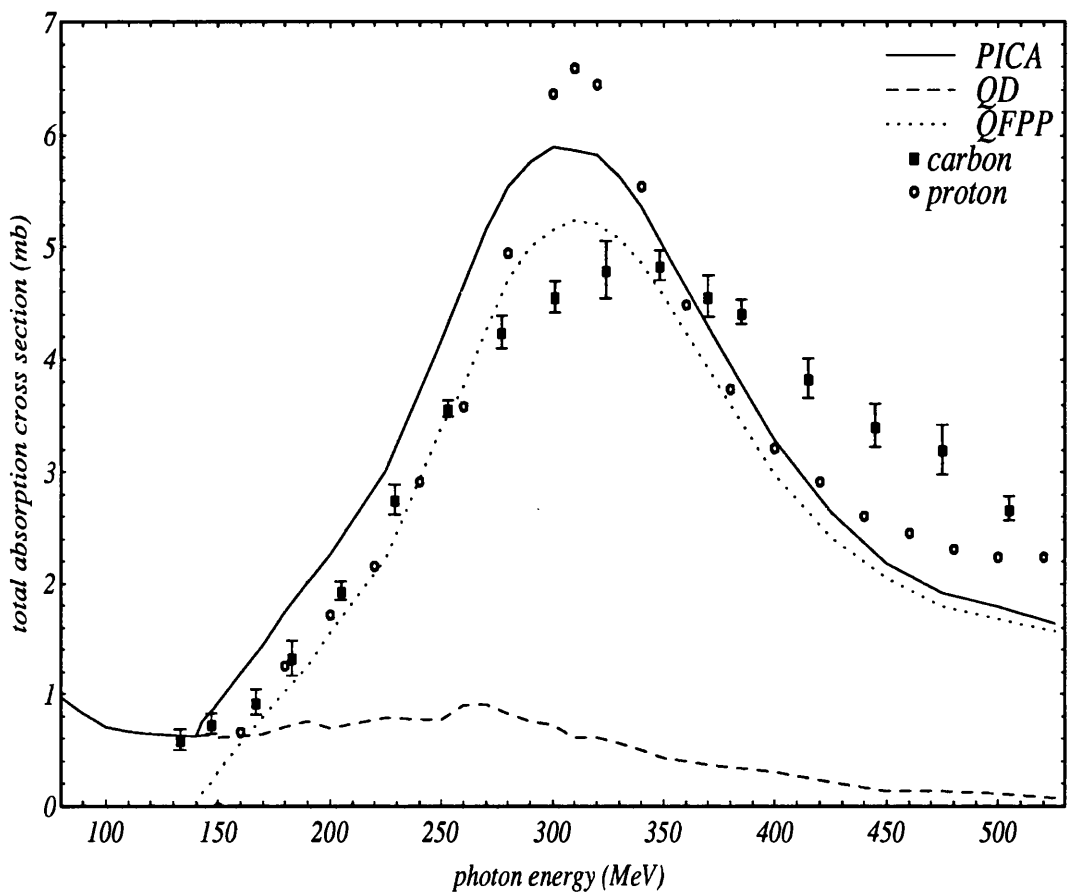


Figure 5.5: The ^{12}C total photoabsorption cross section

data in this energy range should help assess the validity of the Levinger parameter used. Initial comparison between PICA and the experimental data indicated that the value 10.3 used by the authors of PICA [95] was considerably too large. There is only one point in the Saclay ^{12}C data set below the pion production threshold, and so L was estimated by comparing the average σ_{total}/A for several elements shown in [103] to the deuterium cross section [96] yielding a value of 4.1 ± 0.6 . This is considerably smaller than the value of 10.3 used by Arends *et al* [29], but this may not be significant given the discrepancy between the Bonn and present (γ, p) cross section discussed in section 5.1. However, Baba *et al* also use a comparatively large value of $L=8.0$ [26] and get good agreement with PICA, but their measurements were taken at relatively high photon energies where the quasi-deuteron component is very small in relation to the quasi-free pion component. Anghinolfi *et al* did not compare their data to PICA, but do quote an L value of 5.

Above the pion production threshold the total absorption cross section rises sharply due to the excitation of the $\Delta(1232)$ resonance. At these energies the cross section predicted by PICA is markedly different to the experimental data shown in figure 5.5. Also shown are the separate QD and QFPP components provided by PICA and the total absorption cross section of the proton [1] multiplied by a factor 12. Although the QFPP cross section is smaller than that of the proton, as expected, it is larger than the ^{12}C cross section and is similar to the proton cross section in shape. The total cross section predicted by PICA also peaks at the same photon energy as the proton cross section, not $\sim 30\text{MeV}$ higher as observed in ^{12}C and other complex nuclei. These discrepancies suggests that effects of final state interactions (FSI), Fermi momentum of the nucleons and Pauli blocking of final states are not properly modelled in PICA.

Above the $\Delta(1232)$ resonance the cross section from the PICA calculation falls. The QFPP Δ peak is significantly narrower than expected in complex nuclei due to the deficiencies discussed above and PICA therefore underestimates the cross section at these high photon energies. However, PICA is not intended to be used at photon energies above $\sim 350\text{MeV}$ [95] as it neglects the double pion production mechanism, which is not as large as that from single pion production.

Since the QFPP component in PICA is obviously distorted it was decided to modify the magnitude of the QFPP component's cross section before comparing PICA to the experimental data. Normalisation factors were calculated for each photon energy bin studied to bring the QFPP component of PICA in line with

the Universal Curve. The shape and size of the QD component was not altered by this process. The omission of double pion production in PICA is not expected to have a large influence on the observed reaction channels for the present detector geometry. The QFPP normalisation factors used are tabulated below.

photon energy bin (MeV)	QFPP normalisation factor
200±10	0.79
300±10	0.74
400±10	1.22
500±10	1.23

Table 5.1: *PICA QFPP normalisation factors*

5.2.1 The $^{12}\text{C}(\gamma, p)$ Reaction

Figure 5.6 shows the (γ, p) cross section as a function of proton energy for protons hitting the most forward ΔE_2 element (*ie* $52^\circ < \theta_p < 69^\circ$) at incident photon energies of 200, 300, 400 and 500MeV. The data are compared with PICA calculations carried out for the same geometry and photon energy bins. The QD and QFPP components obtained by PICA are also displayed to aid the discussion.

The PICA calculations predict two distinct peaks in the proton energy spectrum at photon energies above the pion production threshold. The higher peak at $\sim (E_\gamma - S_{2N})/2$ is generated by events from QD processes. The expected position of this peak is shown by the arrows on the spectra and agrees with both the calculation and the data. The other peak is due to QFPP and occurs at low proton energies as $\sim 140\text{MeV}$ is required for pion production. The spectra are truncated at low proton energies to account for the detector proton energy threshold and only the tail of the QFPP distribution is evident. As the detector also has an upper proton energy limit at 220-240MeV the spectra are also truncated at 250MeV.

There are obvious differences in the predicted behaviour of the two peaks as a function of photon energy. The magnitude of the QD component falls slowly with increasing photon energy, and it appears broader and at increasing proton energy as is expected from the reaction kinematics. It dominates the spectra at $E_\gamma=200\text{MeV}$ but is almost totally suppressed at 500MeV where the peak is beyond the upper proton energy threshold. The QFPP component, however,

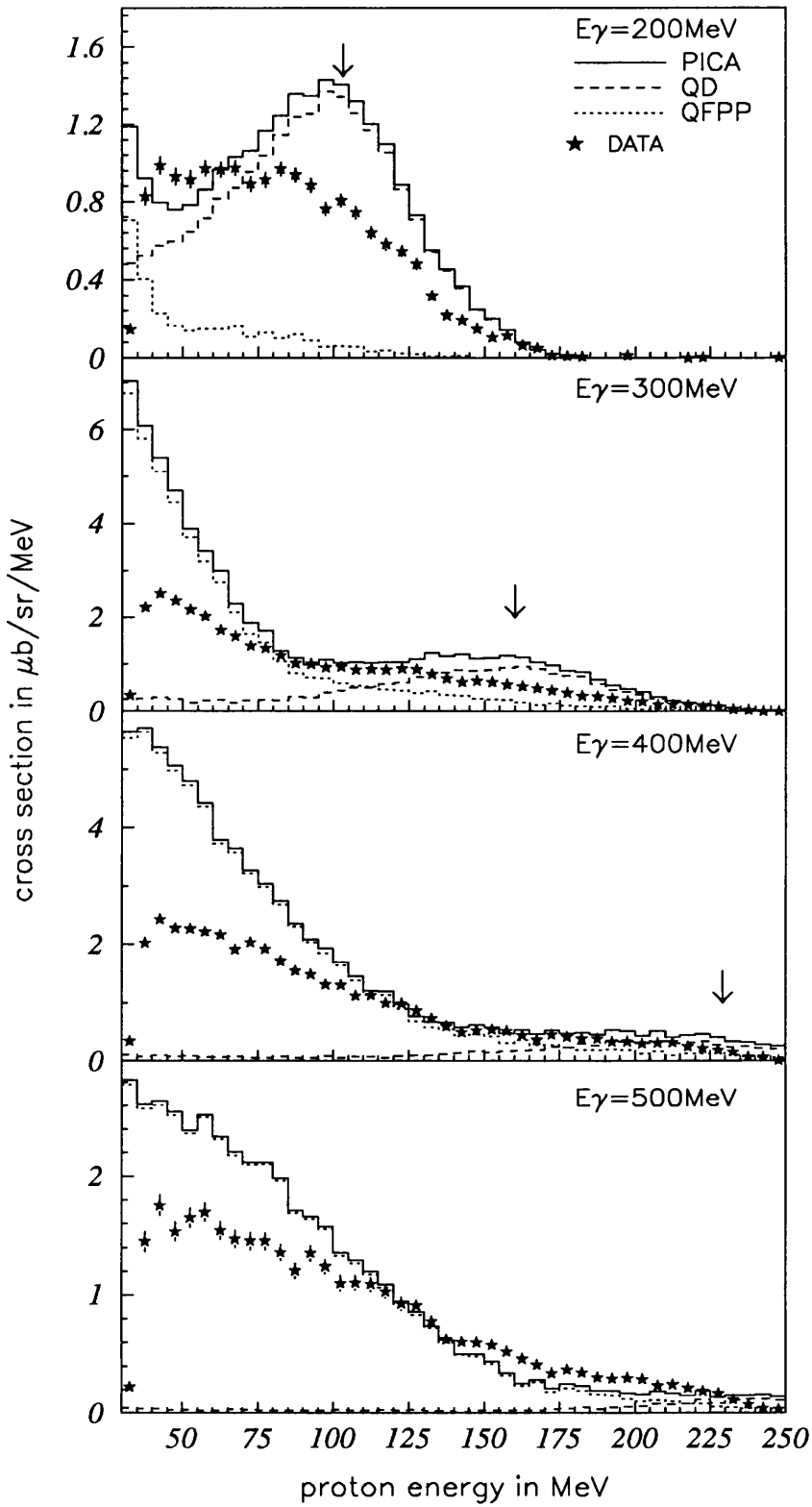


Figure 5.6: The $^{12}\text{C}(\gamma, p)$ cross section at $61^\circ \pm 8^\circ$, the arrows mark the expected centroid of the QD peak.

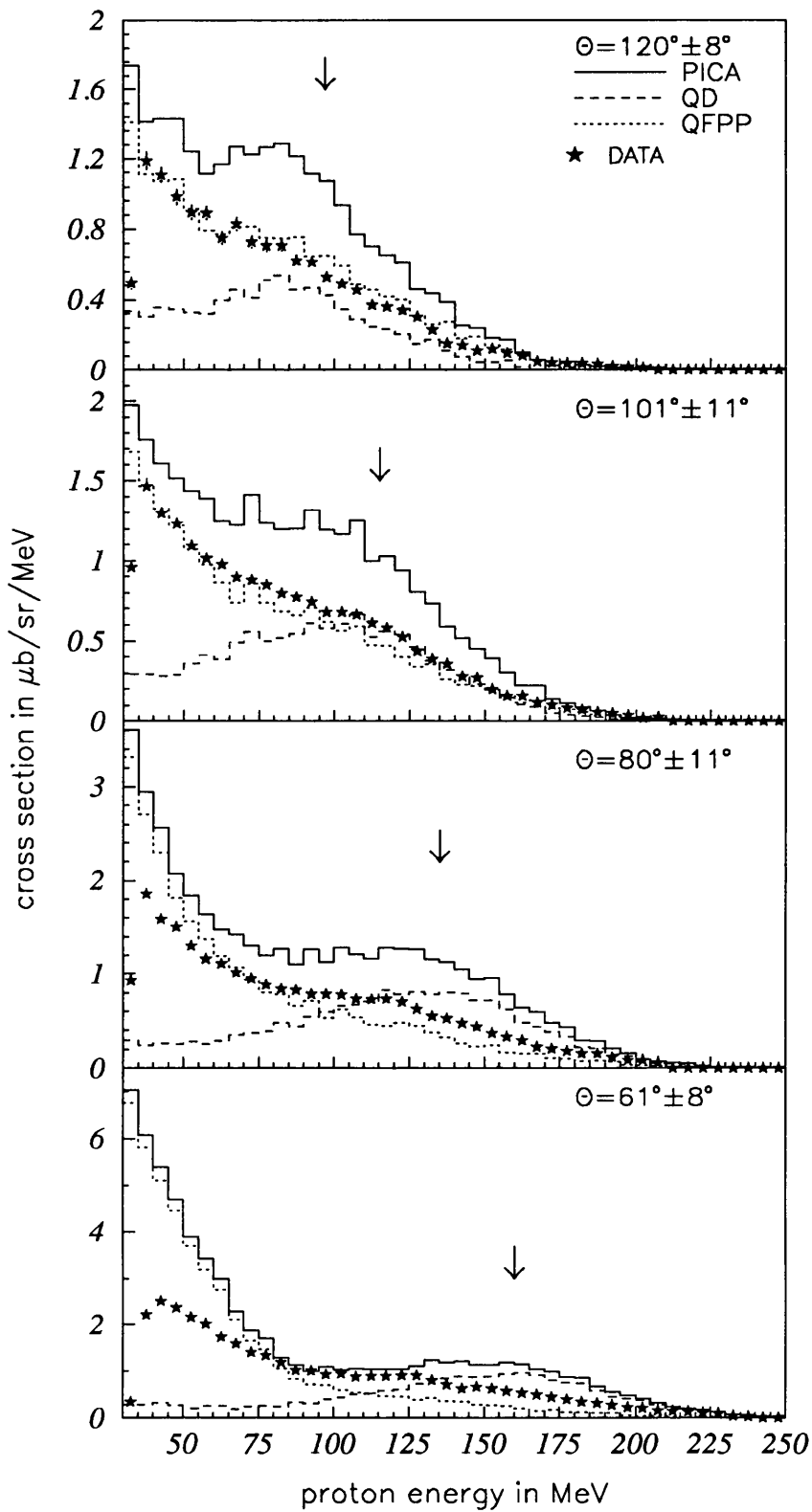


Figure 5.7: The $^{12}\text{C}(\gamma,p)$ cross section at $300 \pm 10 \text{ MeV}$

rises to a maximum between 300 and 400MeV before falling again. This peak also moves to higher proton energies with higher photon energy, again due to the reaction kinematics, but the detector threshold is too large to show the low energy side of this peak at any photon energy. At 300MeV and above the QFPP peak dominates the predicted cross section.

The data show some indication of the structure predicted by PICA, although the two mechanisms are not so clearly distinguished. A small QD component moves to higher proton energies as E_γ changes from 200 to 400MeV and is also totally suppressed by the upper proton energy threshold of the detector at $E_\gamma=500\text{MeV}$. In addition, at lower proton energies a peak with QFPP kinematics rises in strength and then falls as E_γ is increased, in agreement with calculations. The strength of this peak is overpredicted by PICA despite, or at higher photon energies perhaps because of, the renormalisations discussed above. PICA predicts the cross section to be largest at 300MeV and to fall more rapidly than the data which peak between 300 and 400MeV.

Figure 5.7 shows the (γ, p) cross section as a function of proton energy at an incident photon energy of $\sim 300\text{MeV}$ for the four ΔE_2 elements. The interpretation of the (γ, p) spectra at all angles is similar, although the distinction between the two peaks becomes less evident in the data at backward angles with the QD strength appearing as an elongated tail on the QFPP distribution. The strength of the cross section is overpredicted by PICA at all angles. This appears to be due to too large a QFPP component.

The calculated behaviour of the two components is again obviously different. The magnitude of the QFPP component decreases rapidly with proton angle, whereas the QD component has a much weaker angular dependence and appears to peak at proton angles between 60° and 80° , roughly 90° in the centre of mass frame. However, both distributions move to smaller proton energies at large proton angles because of the reaction kinematics and therefore more of the QFPP peak is evident above the proton detector threshold at small angles perhaps exaggerating the angular dependence of its cross section. The greatest distinction between the two processes is at the smallest proton angles. There is some evidence of this behaviour in the data, but it is again less structured than PICA.

The features of the data discussed above are general, and are as expected from the rather naive level of theory incorporated in PICA. In order to gain a

more complete understanding of the processes involved it is necessary to look at coincident data. Each exclusive reaction channel studied is discussed in detail in the next sections.

5.2.2 The $^{12}\text{C}(\gamma, pn)$ Reaction

Below the pion production threshold the (γ, pn) cross section is generated by quasi-deuteron type processes. However, at higher photon energies additional contributions arise due to the effect of quasi-free pion production. Pions produced in these processes may subsequently be reabsorbed on nucleon pairs leading to the emission of two secondary nucleons, or scattered knocking out neutrons with the result that all three particles are emitted. The present experimental geometry is optimised to detect nucleon pairs from direct absorption resulting in a small efficiency for the detection of all three particles emitted in indirect processes.

Figure 5.8 shows the (γ, pn) cross section, or more exactly the proton energy spectrum for events in which a coincident neutron is detected in the TOF array, at fixed proton angle of $61^\circ \pm 8^\circ$ for incident photon energies of 200 - 500MeV. The two-peaked structure is evident in the PICA calculation for this exclusive reaction channel, and the peaks are somewhat stronger than for the inclusive (γ, p) channel. The QD peak is clearly visible at all photon energies up to 400MeV, and is even suggested at 500MeV despite being largely cut off by the upper proton energy threshold. The lower energy peak is again due to the QFPP events in which the pion suffers FSI causing a nucleon pair to be emitted. The predicted strength of the QD component of the cross section falls slowly with photon energy in the Δ resonance region and much faster above $\sim 400\text{MeV}$. On the other hand, the QFPP component is negligible at 200MeV and rises to a maximum between 300 and 400MeV before falling again.

The agreement between PICA and the data in this channel is rather good. The strength of the QFPP distribution is only overpredicted by PICA at 400MeV, and the QD component appears to slightly overpredict the data at all incident photon energies, and especially at 300MeV.

The (γ, pn) cross section is also shown at four angles for an incident photon energy of 300MeV in figure 5.9. PICA shows that the two peaks overlap at all but the most forward angles making it difficult to assess the contributions of the two reaction mechanisms separately. However, there is some suggestion that the QD component is not a strong function of angle and rises to a maximum between

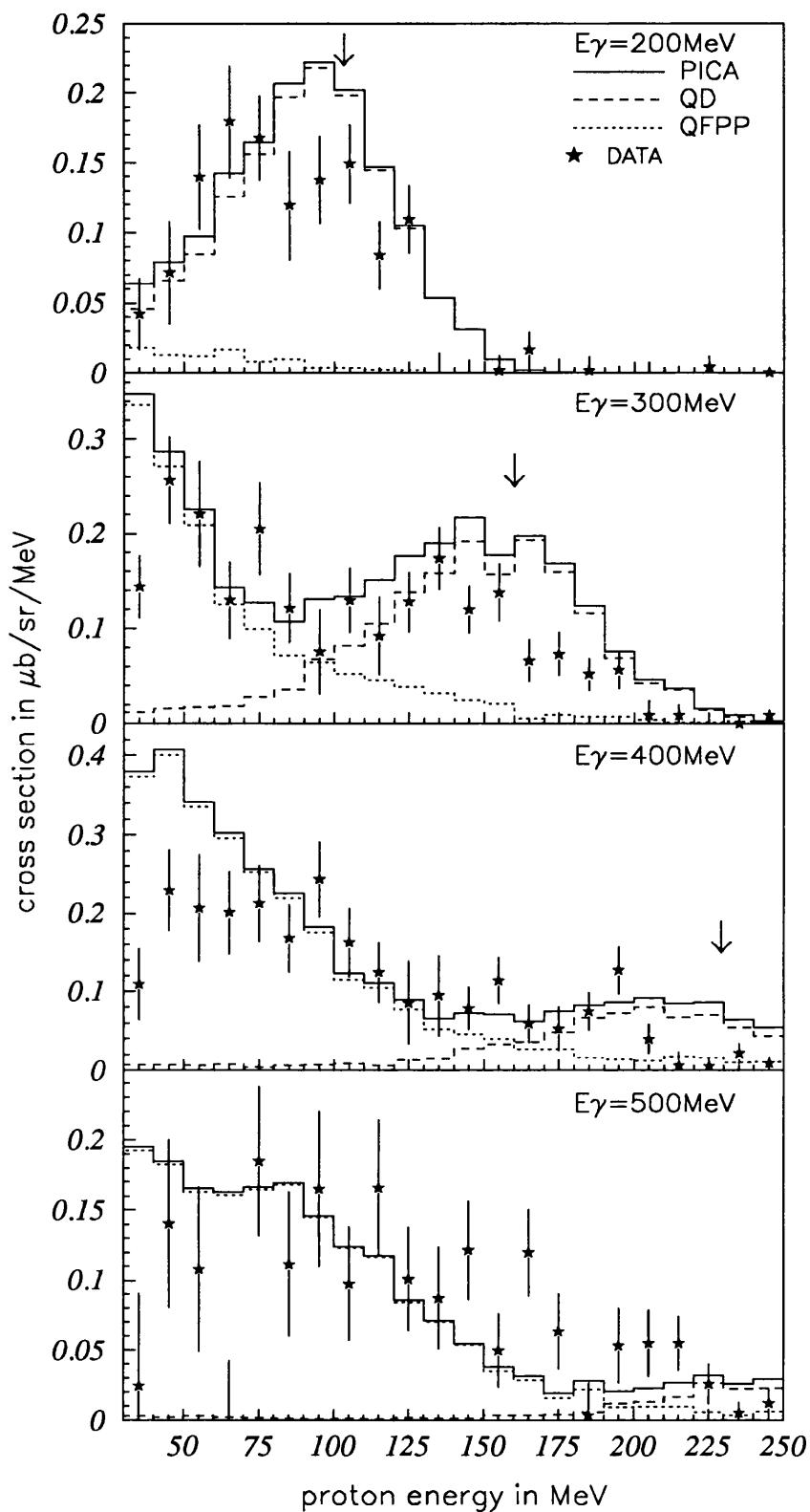


Figure 5.8: The $^{12}\text{C}(\gamma, pn)$ cross section at $61^\circ \pm 8^\circ$

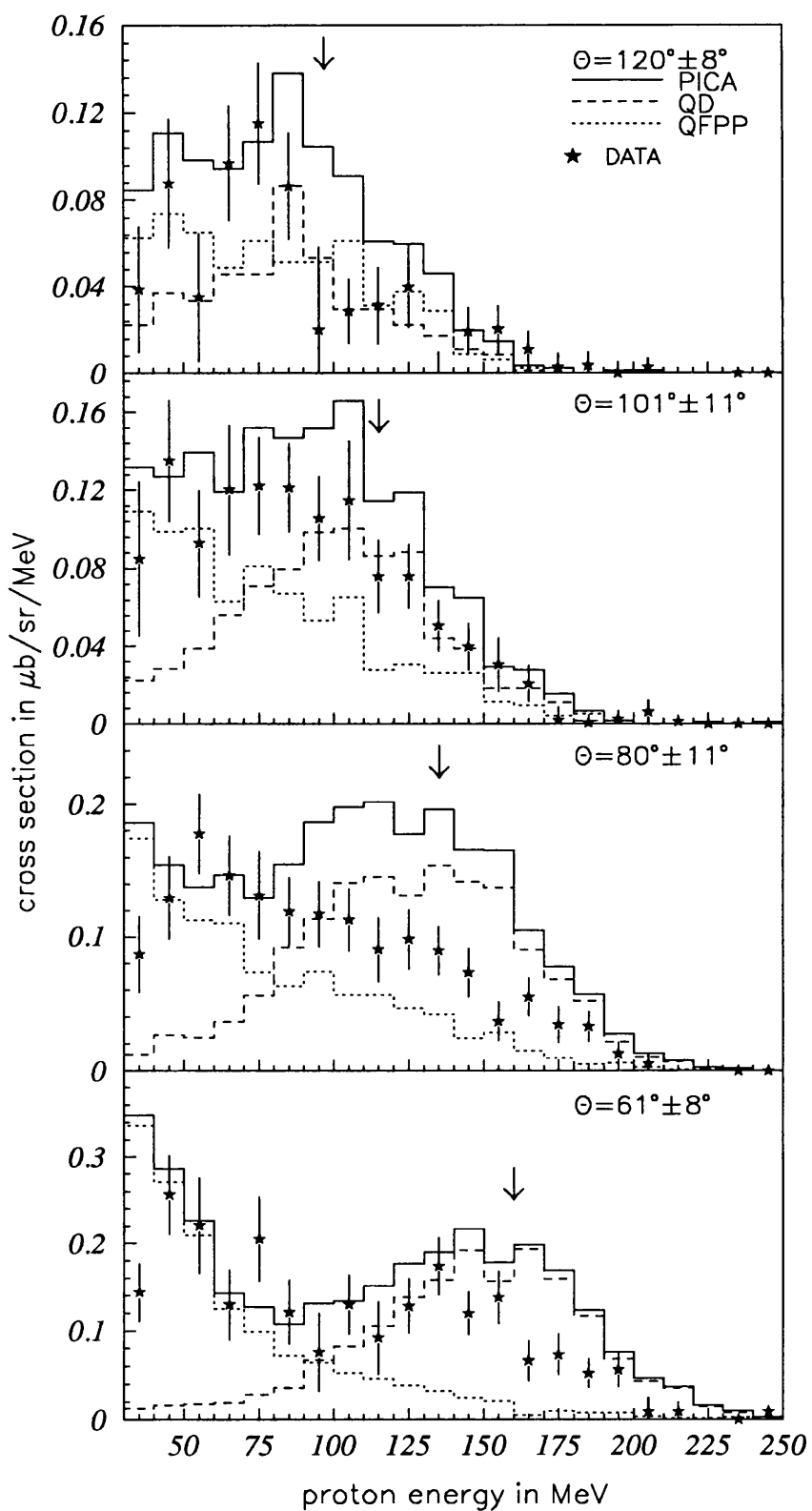


Figure 5.9: The $^{12}\text{C}(\gamma, pn)$ cross section at $300 \pm 10 \text{ MeV}$

60° and 80°. The QFPP component, however, appears to be a much stronger function of angle, reaching a maximum at forward angles where more of its peak is visible.

These features are also evident, if less distinct, in the data. The QFPP component agrees well at all photon energies, but the QD component is somewhat overestimated, especially at $\sim 80^\circ$ and $\sim 101^\circ$. This suggestion that the data have a slightly different angular distribution than that of the real deuteron, as assumed by PICA, agrees with recent theoretical predictions by Ryckebusch *et al* [37].

5.2.3 The $^{12}\text{C}(\gamma, p\pi)$ Reaction

Unlike all other channels, the $(\gamma, p\pi)$ reaction is solely fed by the QFPP mechanism. As discussed previously, PIP misses most of the protons from the QFPP process, and those detected arise mainly from the edges of the Fermi momentum distribution of the nucleons in the nucleus or from FSI scattering.

Figure 5.10 shows the cross section at a fixed angle of $61^\circ \pm 8^\circ$ at photon energies from 300 to 500MeV. There are no data at 200MeV where the protons produced by QFPP are below the PIP energy threshold. The single QFPP peak predicted in this channel behaves similarly to the predicted QFPP components discussed previously. Its strength is greatest at 300MeV incident photon energy, but at higher photon energies, where the detectors are better matched to the reaction kinematics, more of the peak is visible.

Although the spectra are fairly featureless, just consisting of the tail of the QFPP distribution, there is again good agreement between PICA and the data. The data have a cross section which appears to reach a maximum between 300 and 400MeV whereas PICA still predicts the cross section to be largest at 300MeV. However, unlike the other reaction channels, the agreement between PICA and the data is good for all incident photon energies.

Figure 5.11 shows the cross section at four angles for an incident photon energy of 300MeV. The forward peaked nature of the QFPP component is very apparent from these spectra with the cross section increasing by about a factor 10 from backward to forward angles.

The agreement between the renormalised PICA and the experimental data is very good for all angles. Despite the small discrepancy in the magnitude, the variation of the cross section with angle is well represented, as is the width of the observed distribution.

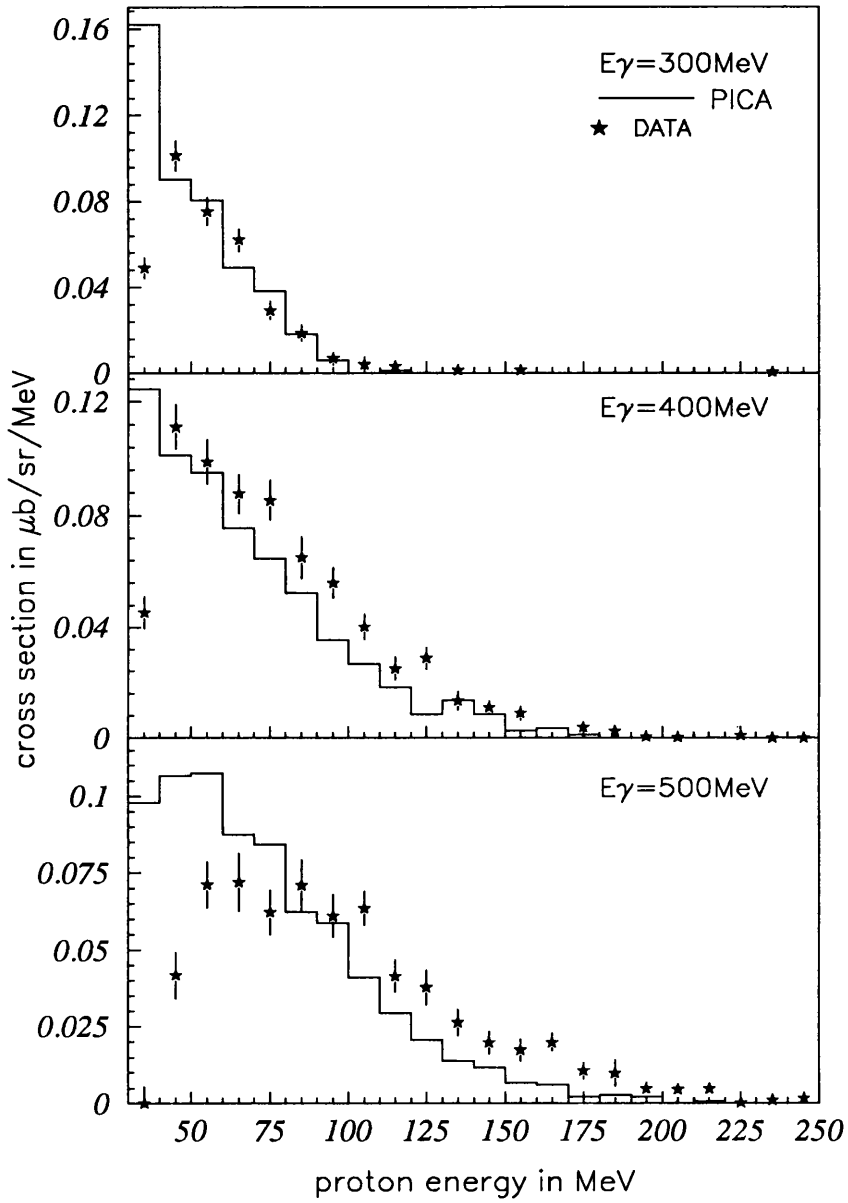


Figure 5.10: The $^{12}\text{C}(\gamma, p\pi)$ cross section at $61^\circ \pm 8^\circ$

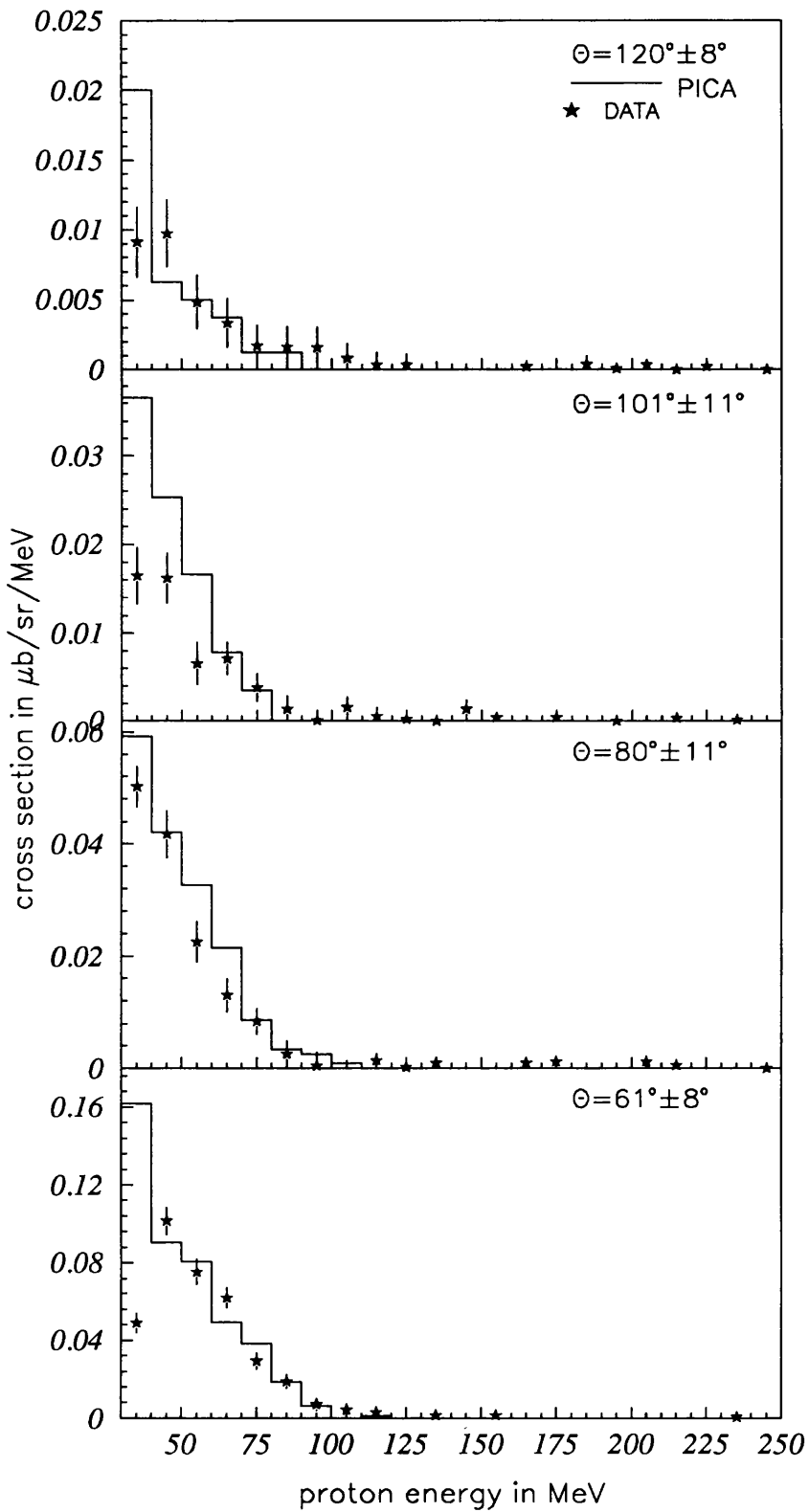


Figure 5.11: The $^{12}\text{C}(\gamma, p\pi)$ cross section at $300 \pm 10 \text{ MeV}$

The agreement between the QFPP component in PICA and the data in the two main reaction channels ((γ, pn) and $(\gamma, p\pi)$) is unexpected given the large discrepancy between the QFPP component and the inclusive (γ, p) reaction channel. The experimental geometry is such that TOF intercepts a large fraction of possible trajectories of the associated particle in reactions with QFPP kinematics, suggesting that the missing particles may have been lost through final state interactions. In this case both the predicted absorption cross sections and the strength of final state interactions are overestimated by PICA.

5.2.4 The $^{12}\text{C}(\gamma, pp)$ Reaction

The (γ, pp) reaction channel is more controversial than the others. The quasi-deuteron model [2] does not predict its presence, and it was originally assumed to arise from a (γ, pn) reaction followed by FSI [9]. However, Gottfried suggested that it could arise if the photon was absorbed by a pair of protons in a relative 3P state [8]. Recent theoretical studies of this reaction channel by the Pavia group have suggested that although the (γ, pp) cross section is small it is more likely to show evidence of short range nuclear correlations than the (γ, pn) channel as the effects of meson exchange currents are negligible [32].

The experimental results are equally contradictory. (γ, pp) cross sections of complex nuclei have been measured in the QD energy region at the order of a few percent of the corresponding (γ, pn) cross section, *eg* [19], [25]. The results show that the reaction kinematics indicate a quasi-deuteron type reaction, but more detailed analysis has suggested a (γ, pn) reaction followed by FSI. The situation becomes even more confusing at higher photon energies as new channels arising from quasi-free pion production and $\Delta(1232)$ excitation are opened. Indeed some of the increasing ratio of the (γ, pp) to (γ, pn) cross sections in this energy range has been taken as evidence of QFPP followed by FSI [27].

The (γ, pp) cross section is shown at four different photon energies and a fixed angle in PIP of $61^\circ \pm 8^\circ$ in figure 5.12. The measured cross sections are much smaller than for (γ, pn) , rising from $\sim 10\%$ of the (γ, pn) cross section at 200MeV to $\sim 40\%$ at 500MeV. This relative increase is in general agreement with previous measurements, and with recent theory [37] which predicts a significant, if smaller, increase in the ratio of (γ, pp) to (γ, pn) cross sections from quasi-deuteron type processes.

PICA predicts a fairly featureless proton energy distribution, and suggests

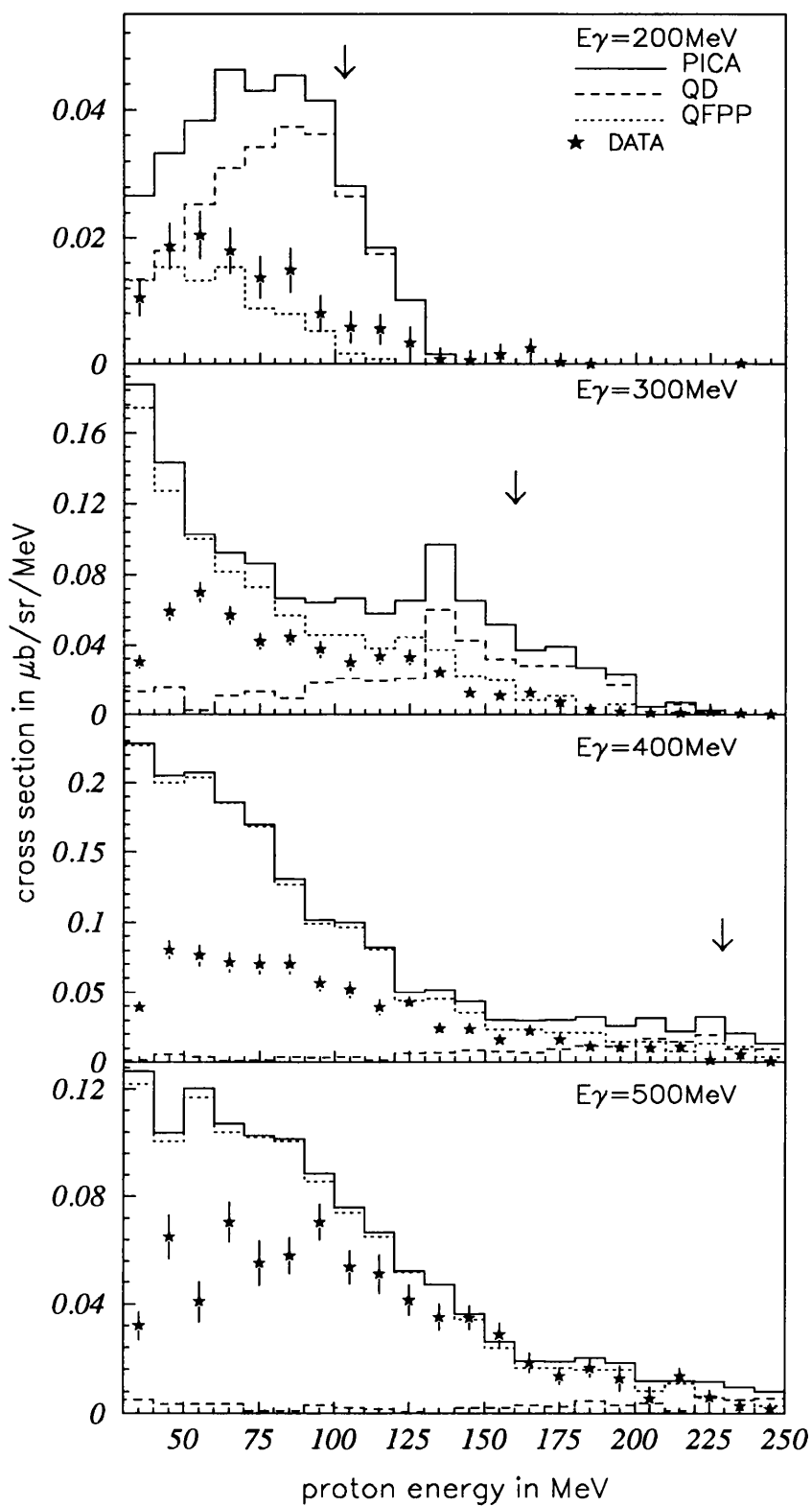


Figure 5.12: The $^{12}\text{C}(\gamma, pp)$ cross section at $61^\circ \pm 8^\circ$

that the spectra are dominated by the QFPP component which is strongly peaked towards low proton energies. The predicted QD component is small and falls rapidly with increasing photon energy. The QD peak is largely washed out by FSI, and is only evident at 200 and 300MeV photon energy. A pronounced QD peak would provide evidence of (γ, pp) events following (γ, pn) absorption and charge exchange in a final state interaction.

PICA consistently overestimates the magnitude of the (γ, pp) cross section at all photon energies. The predicted structure is totally absent in the data, which have a fairly flat distribution at all incident photon energies. However structured distributions are also predicted by PICA for the (γ, pn) reaction whose measured spectra are also less distinct.

Figure 5.13 shows the (γ, pp) cross section at the four proton angles at 300MeV incident photon energy. Unlike the (γ, pn) reaction, the predicted (γ, pp) cross section increases steadily with decreasing angle, but not nearly as rapidly as that of the pure QFPP $(\gamma, p\pi)$ cross section. There is very little change in the predicted structure of the (γ, pp) cross section with changing detection angle. PICA has some evidence of a QD peak moving to smaller proton energies with increasing proton angle, but this is largely hidden by the dominant QFPP mechanism.

Like PICA, the experimental cross section increases with decreasing proton angle, but the change is more rapid in the data than in PICA. Indeed, PICA overestimates the cross section about about a factor 2 at forward angles but a factor 4 at backward angles. However, again the measured cross sections are possibly even less structured than the predicted.

Both the QD and QFPP components are consistently overpredicted by PICA, and as the (γ, pp) channel is solely fed by events which undergo FSI this suggests that FSI are too strong in PICA. It remains an open question whether a better treatment of FSI will enable the energy and angular behaviour of the (γ, pp) spectra to be explained fully or whether evidence of a direct $2p$ absorption can be found. However, its is already obvious that there is no sign in the data of a strong direct $2p$ absorption mechanism.

5.2.5 Other Theories

In Chapter 1 a number of new microscopic theories were discussed. Two of these calculations, those of Carrasco *et al* and those of Ryckebusch *et al* have been compared to the Bonn data in references [47] and [38] respectively. It was

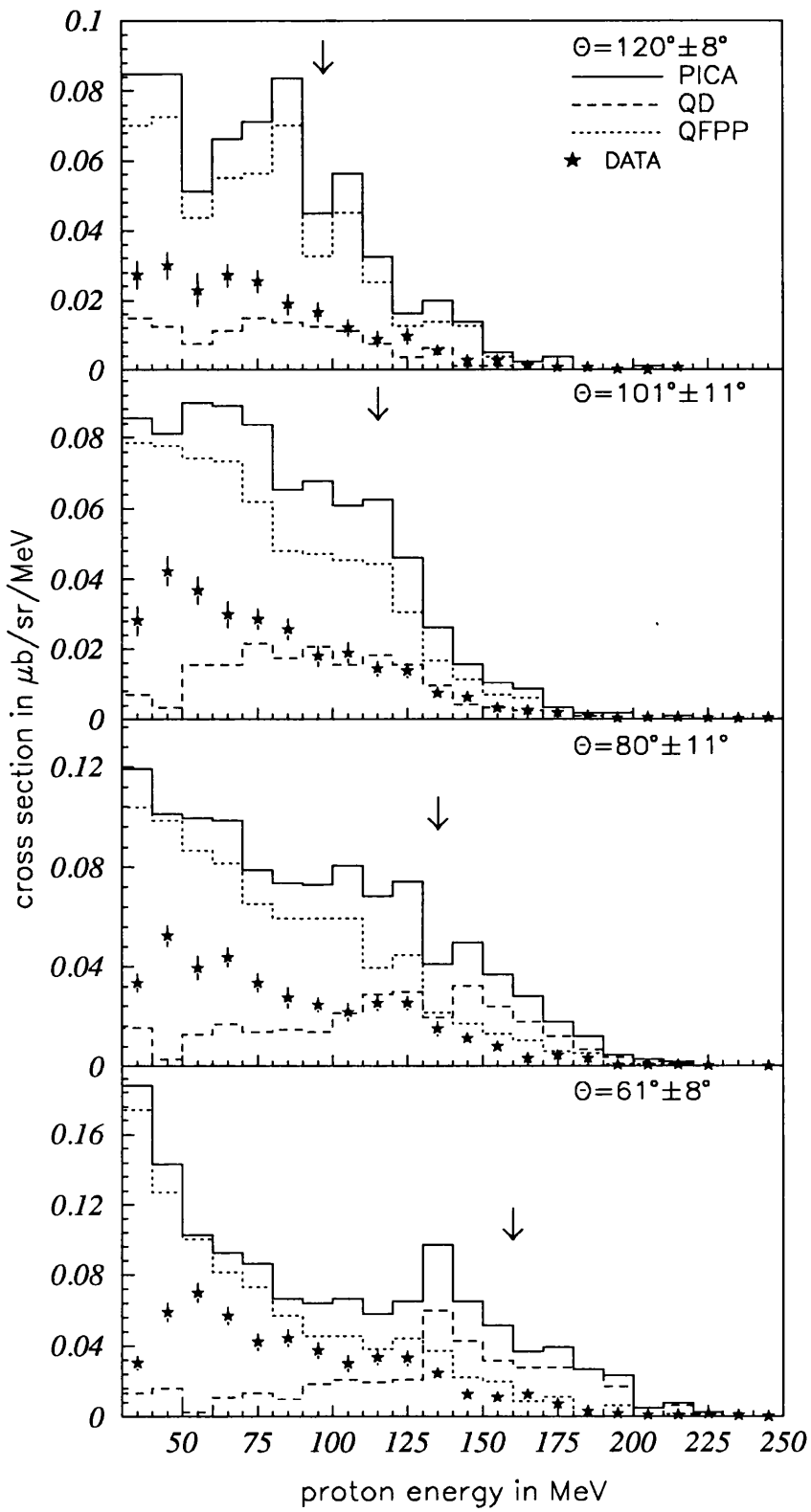


Figure 5.13: The $^{12}\text{C}(\gamma, pp)$ cross section at $300 \pm 10 \text{ MeV}$

therefore decided to compare these theoretical predictions with the present data, keeping in mind the differences between Bonn and the present experimental data described above.

Figure 5.14 shows the results from the calculations of Ryckebusch *et al* for the $^{16}\text{O}(\gamma, pn)$ and $^{16}\text{O}(\gamma, pp)$ cross sections at a proton angle of $\sim 50^\circ$ at $\sim 300\text{MeV}$ [38]. As discussed in section 1.3.2 these calculations use an unfactorised cross section. Absorption is assumed to take place on meson exchange and isobar currents, and final state interactions are included via a distorted wave impulse approximation (DWIA). It should be noted, however, that this theory does not include any QFPP mechanisms, and therefore cannot predict the large cross sections at low proton energies. However, the group is presently extending their calculations to include such processes in order to provide a more complete comparison to the experimental data at intermediate photon energies [104]. The data from both the present experiment, renormalised to account for missing solid angle in TOF, and the Bonn experiment on oxygen are shown as a comparison.

The (γ, pn) calculation matches both sets of data tolerably well at proton energies greater than 100MeV . It should be noted that the cross sections from both sets of data fall off rather quicker than the calculations. In the case of the present data this may be partly due to the upper energy threshold of the proton detector at $220\text{-}240\text{MeV}$, and which could be raised in subsequent analysis by including the E3 and E4 layers of PIP to allow a more complete comparison.

Similar agreement between the calculation and both sets of (γ, pp) data is seen at high proton energies. Here the distortions from FSI are known to be important in predicting the magnitude of the cross section [38]. Although this is encouraging for any future attempts to study the effects of SRCs on the (γ, pp) cross section as this model includes direct absorption on pp pairs, the earlier comparisons with PICA have indicated that this reaction is also sensitive to QFPP processes. All channels will have to be included in the calculations before the (γ, pp) reaction can be fully understood.

It is important to remember that these calculations by Ryckebusch *et al* were performed for the Bonn experimental geometry and for an ^{16}O target. Our results have been roughly renormalised to allow a comparison, and the resulting agreement may be fortuitous, indeed normalising by a factor greater than 3 would perhaps give better agreement.

Figure 5.15 shows the results from the calculation by Carrasco *et al* performed to compare with the Bonn $^{12}\text{C}(\gamma, p)$ experimental data [47]. The results are for a

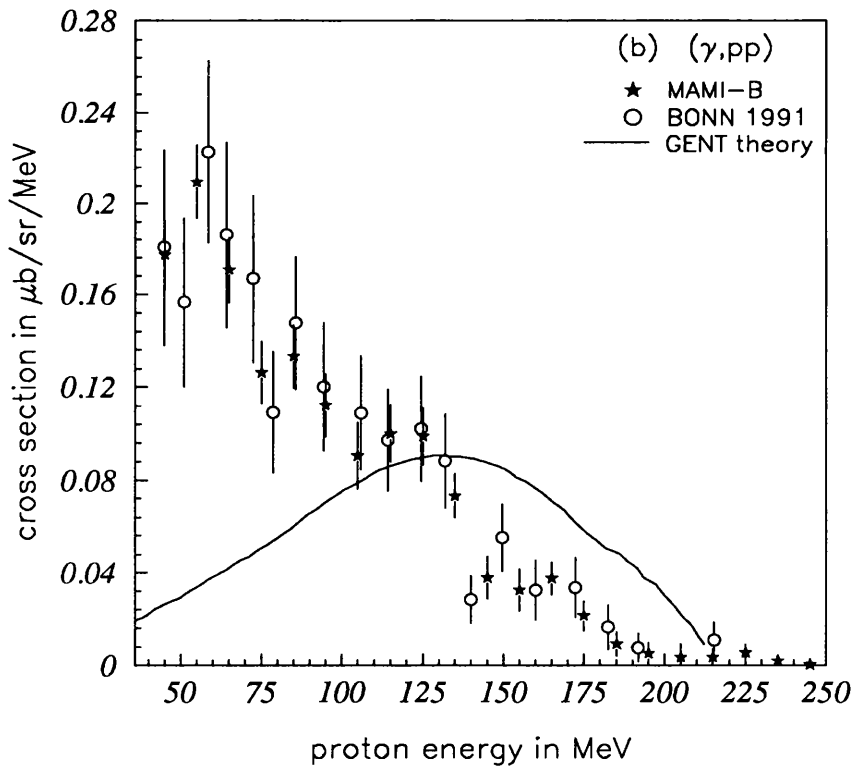
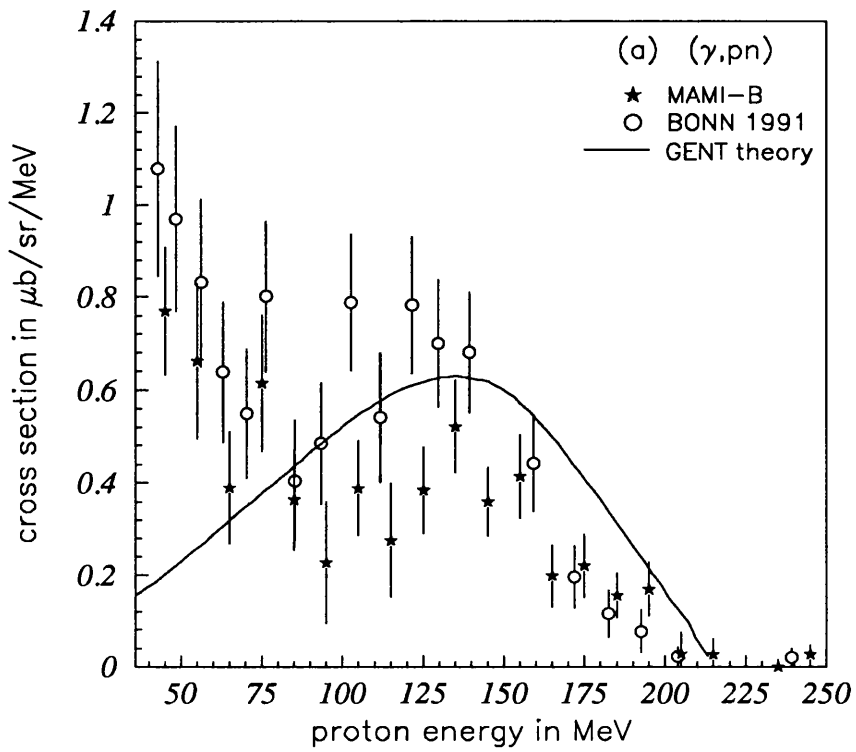


Figure 5.14: *Exclusive cross sections at $E_\gamma \sim 400\text{MeV}$ and $\theta_p \sim 60^\circ$*

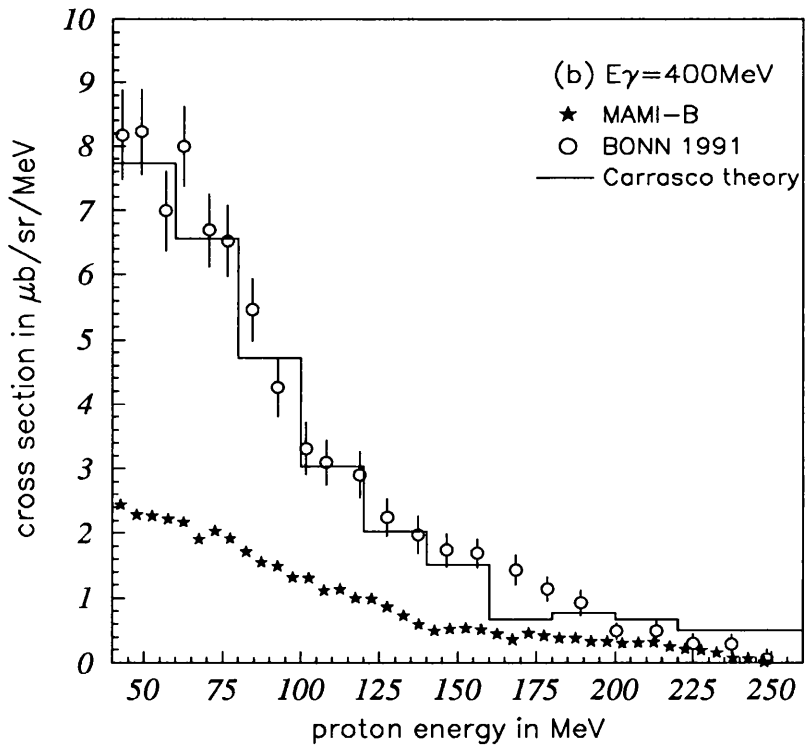
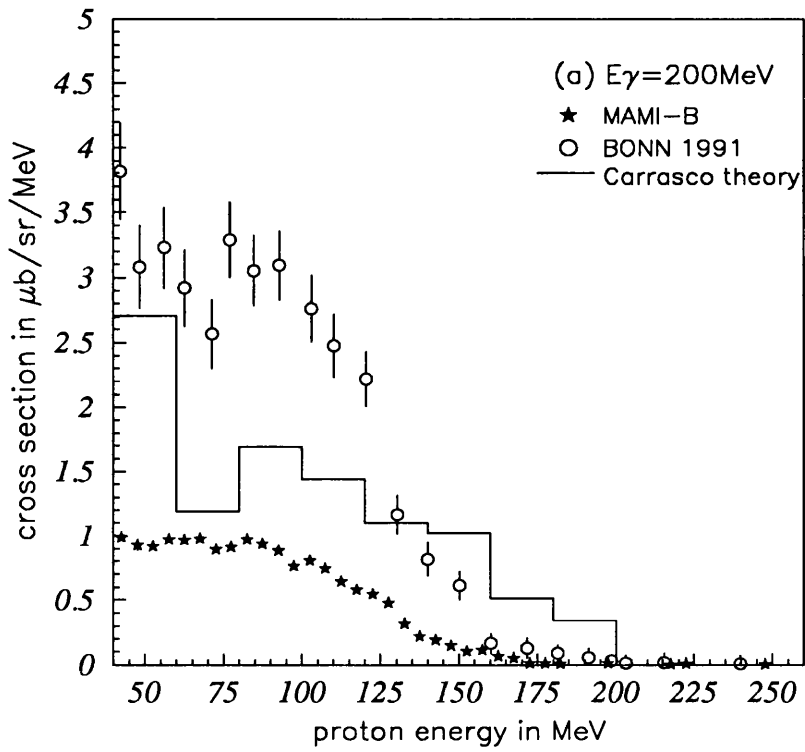


Figure 5.15: *Inclusive (γ, p) cross sections at $\theta_p \sim 60^\circ$*

proton angle of $\sim 50^\circ$ at photon energies ~ 200 and ~ 400 MeV. This theory includes all the basic couplings between the photon and nucleons and should therefore provide a more complete comparison to the data than any other calculation. The data from both the present experiment and the Bonn experiment are again displayed.

The theory agrees well with the Bonn data at 400 MeV, and therefore does not agree with the present data in magnitude. The original publication does not discuss the normalisation of the theoretical cross section, so it is impossible to tell how serious this discrepancy is. However, it should be possible to obtain reasonable agreement between the present data and this theory by a simple change of magnitude as the present data agrees in shape with that of Bonn. At 200 MeV the Bonn data and the theory do not agree either in magnitude or in shape, the theory looking rather like the PICA calculations with distinguishable QD and QFPP components. The theory also does not agree with the present data either in shape or in magnitude. At higher photon energies FSI are very important and the more realistic shape predicted by the calculation at this energy may rely more on its ability to model FSI than on its ability to model the basic photonuclear interaction. In this light it is interesting to note that the theory agrees well with the data from lead at both energies [47], as the features of this data should be dominated by FSI effects at all photon energies.

5.3 Conclusions

Presented in this thesis are results from the first round of experiments performed at MAMI-B with the PIP and TOF detectors. These detectors have the potential to fully define the reaction kinematics of photonuclear reactions leading to the emission of two particles in order to explore fully the processes contributing to the absorption of photons by complex nuclei at intermediate energies. The experimental system has therefore been designed to have missing energy resolution of order 7 MeV and opening angle resolution of order $5-10^\circ$.

One of the main objects of this thesis project was to test the performance of the new detector systems at MAMI-B, and in particular the charged particle detector PIP. The results of the calibrations are shown in chapter 3 and show that PIP has largely met its design criteria. It is able to discriminate between the charged particles of interest (protons, pions and deuterons) and reject the large electromagnetic background of electrons. Any overlap between the π^+ s and

electrons can be removed by use of the afterpulse requirement. The position response of the ΔE_2 and E1 layers are both linear, and resolutions of 5cm and 3cm FWHM respectively were deduced. These resolutions were slightly larger than expected, perhaps because of the convoluted calculation methods used, and more work is therefore required to more accurately estimate the values, or explore why they are slightly larger than expected. An energy calibration of the E1 and E2 layers was obtained using both cosmic ray and $D(\gamma, p)n$ information, and both methods were shown to give similar results. Energy resolutions of $\sim 6\%$ were estimated for all proton energies up to 150MeV, however, final values are not quoted as the method used to calculate the energy resolution is dependent on the only approximately known position resolution.

Some work remains to be done on PIP. Although the $D(\gamma, p)$ reaction does not produce many high energy protons it is possible to calibrate the E3 and E4 layers solely using cosmic ray data. This will allow the upper threshold to be increased to $\sim 350\text{-}400\text{MeV}$. Monte Carlo simulations will be useful not only to predict the detector's performance but also to supply some corrections, *eg* for inelastic losses within the scintillator.

The TOF array has been shown to provide good particle identification for both charged and neutral particles. Its calibration has not been addressed in this thesis, but will have to be done in order to make full use of the data available and to challenge properly the new microscopic theories emerging. Monte Carlo simulations will also be required for this detector array.

Data on the photoproduction of protons from ^{12}C have been obtained over the photon energy range 200-500MeV. The data have been presented as partial differential cross sections as a function of proton energy for both inclusive (γ, p) reaction and exclusive (γ, pn) , (γ, pp) and $(\gamma, p\pi)$ reactions. Although a full understanding of the importance of the different photon absorption processes will require the study of the kinematic correlations of the two or three particles emitted in such reactions, the present simpler analysis has provided a very useful overview of the data. It has proved possible to account for the general trends of the data in terms of just two basic mechanisms, quasi-free pion production and the absorption by nucleon pairs. It is clear therefore what detailed kinematic analyses should be attempted initially, and roughly what photon energy dependence may be anticipated for these processes.

The proton energy spectra have been compared to various previous measurements. Good agreement was obtained with the inclusive cross section of Baba *et*

al and Anghinolfi *et al*, and with the exclusive cross sections of Arends *et al* once differences in the solid angle coverage of the associated particle detector were approximately accounted for. However, the magnitude of the inclusive data of Arends *et al* does not agree at all well with the present work at forward angles.

The present data have also been compared to the intranuclear cascade code PICA. Once the absolute magnitude of the cross section had been scaled using total absorption measurements there is reasonable agreement between the data and PICA for the inclusive (γ, p) reaction channel. The comparison highlighted the relative importance of the quasi-deuteron and quasi-free pion production mechanisms which are dominant in this energy range. These observations are reinforced by the study of the exclusive (γ, pn) and $(\gamma, p\pi)$ reaction channels which PICA is better able to predict. PICA does not account well for the (γ, pp) data, and this combined with detailed comparisons suggest that PICA is too rough a calculation to fully explain the data, particularly in its treatment of final state interactions.

The data were finally compared to the microscopic theories of Ryckebusch *et al* and Carrasco *et al*. The results of both theories have been published over a limited kinematical range for comparison to the Bonn data. In addition the former calculation is at present incomplete, so a full discussion was not possible. However, the exclusive results of Ryckebusch were shown to be in reasonable agreement with the quasi-deuteron component of the present (γ, pn) and (γ, pp) cross sections. There was less good agreement between the present data and Carrasco and Oset's theory.

In the short term it is expected that a fuller comparison between the present data and these new theories will be possible. Ryckebusch *et al* are extending their calculations to include quasi-free pion production processes which should allow a comparison to all of the measured reaction channels. The difference in magnitude between the present data and the Carrasco and Oset inclusive cross sections need to be examined fully, but a comparison between their theory and the present data in all reaction channels is also required.

The ability of even such a simple calculation as PICA to reproduce the main features of the data shows that more subtle techniques are required to illustrate the effects of short-range correlations, meson exchange currents and Δ propagation on the photonuclear cross section. Although much of this information is inherent in PICA via the explicit use of the proton and deuterium cross sections, it is of particular interest to explicitly study these microscopic effects in the nuclear medium beyond the simple modifications due to Pauli blocking and Fermi

momentum. In order to fully explore such processes it is necessary to design experiments which can yield information about the nature of specific processes and the effects that they have on each other. It is therefore necessary to consult with the various theorists in the field to learn how to best challenge their theories and learn the most about the processes involved in photonuclear reactions at intermediate energies. Such discussions have already started, and have influenced the measurements taken during subsequent experiments.

Bibliography

- [1] J Ahrens, Nucl Phys A446 (1985) 229c.
- [2] JS Levinger, Phys Rev 84 (1951) 43.
- [3] B Krusche *et al*, *Proc Particles and Nuclei XIII International Conference*, Perugia (Italy), 1993.
- [4] JW Weil and BD McDaniel, Phys Rev 78 (1950) 738.
- [5] D Walker, Phys Rev 81 (1951) 634.
S Kikuchi, Phys Rev 80 (1950) 492.
- [6] C Levinthal and A Silverman, Phys Rev 82 (1951) 822.
- [7] KG Dedrick, Phys Rev 100 (1955) 58.
- [8] K Gottfried, Nucl Phys 5 (1958) 557-587.
- [9] RM Weinstein *et al*, Phys Rev 99 (1955) 1621.
- [10] H Myers *et al*, Phys Rev 95 (1954) 576.
- [11] PC Stein *et al*, Phys Rev 119 (1960) 348.
- [12] A Wattenberg *et al*, Phys Rev 104 (1956) 1710.
- [13] MQ Barton and JH Smith, Phys Rev 110 (1958) 1143.
- [14] J Garvey *et al*, Nucl Phys 70 (1965) 241-263.
- [15] SM Doran *et al*, Nucl Phys A559 (1993) 347-367.
- [16] S Klein, Universität Tübingen PhD Thesis (1990).
- [17] J Vogt, Universität Mainz PhD Thesis (1987).

- [18] SN Dancer *et al*, Phys Rev Lett 61 (1988) 1170.
- [19] JC McGeorge *et al*, *to be published*.
- [20] IJD MacGregor *et al*, Nucl Phys A533 (1991) 269-291.
- [21] L Issakson, *Workshop on Electromagnetically Induced Two-Nucleon Emission*, Tübingen March 1993.
- [22] GG Mauser, Universität Tübingen PhD Thesis (1993).
- [23] S Homma *et al*, Phys Rev Lett 52 (1984) 2026.
- [24] S Homma *et al*, Phys Rev Lett 53 (1984) 2536.
- [25] M Kanazawa *et al*, Phys Rev C 35 (1987) 1828.
- [26] K Baba *et al*, Nucl Phys A415 (1984) 462-476.
- [27] J Arends *et al*, Z Phys A298 (1980) 103-111.
- [28] J Arends *et al*, Z Phys A305 (1982) 205-212.
- [29] J Arends *et al*, Nucl Phys A526 (1991) 479-494.
- [30] L Boato and MM Giannini, J Phys G 15 (1989) 1605-1620.
- [31] S Boffi and MM Giannini, Nucl Phys A533 (1991) 441-454.
- [32] C Guisti, FD Pacati and M Radici, Nucl Phys A546 (1992) 607-621.
- [33] S Boffi *et al*, Nucl Phys A546 (1993) 473-490.
- [34] J Ryckebusch *et al*, Phys Lett B 291 (1992) 213-217.
- [35] L Van Hoorebeke *et al*, Phys Rev C 42 (1990) R1179.
- [36] J Ryckebusch *et al*, Nucl Phys A568 (1994) 828-854.
- [37] L Machenil *et al*, Phys Lett B 316 (1993) 17.
- [38] J Ryckebusch *et al*, *Accepted by Phys Rev C* (April 1994).
- [39] J Steinberger and AS Bishop, Phys Rev 86 (1952) 171.
 RM Littauer and D Walker, Phys Rev 86 (1952) 838.
 WSC Williams *et al*, Phys Rev 105 (1957) 1840.

- [40] S Kabe *et al*, Phys Lett 10 (1964) 354.
- [41] I Endo *et al*, Phys Lett 47B (1973) 469.
- [42] K Baba *et al*, Nucl Phys A306 (1978) 292-310.
- [43] IV Glavankov and VN Stibunov, Sov J Nucl Phys 30 (1979) 465.
IV Glavankov, Sov J Nucl Phys 49 (1989) 58.
PS Anan'in and IV Glavankov, Sov J Nucl Phys 52 (1990) 205.
- [44] LD Pham *et al*, Phys Rev C 46 (1992) 621.
- [45] RC Carrasco and E Oset, Nucl Phys A536 (1992) 445-508.
- [46] RC Carrasco, E Oset and LL Salcedo, Nucl Phys A541 (1992) 585-662.
- [47] RC Carrasco, MJ Vincente and E Oset, *WEIN '92 Conference*, Dubna June 1992.
- [48] X Li, LE Wright and C Bennhold, Phys Rev C 48 (1993) 816.
- [49] I Blomqvist and JM Laget, Nucl Phys A280 (1977) 405.
- [50] B Schoch, Phys Rev Lett 41 (1978) 80.
- [51] H Schmieden *et al*, Phys Lett B 314 (1993) 284.
- [52] SV Springham *et al*, Nucl Phys A517 (1990) 93-107.
- [53] A Sada *et al*, Nucl Phys A551 (1993) 125-134.
- [54] J Ryckebusch *et al*, Phys Rev C 46 (1992) R829.
- [55] EJ Beise *et al*, Phys Rev Lett 62 (1989) 2593.
- [56] JRM Annand *et al*, Phys Rev Lett 71 (1993) 2703.
- [57] HJ Weyer, *International Workshop on Pions in Nuclei*, Penyscola 1991, 441-451.
- [58] LC Smith *et al*, Phys Rev C 40 (1989) 1347.
- [59] SD Hyman *et al*, Phys Rev C 41 (1990) R409.
- [60] RD Ransome *et al*, Phys Rev C 42 (1990) 1500.

- [61] M Steinacher *et al*, Nucl Phys A517 (1990) 413.
 T Bauer *et al*, Phys Rev C 46 (1992) R20.
 RD Ransome *et al*, Phys Rev C 46 (1992) 273.
 P Weber *et al*, Phys Rev C 43 (1991) 1553.
 R Tacik *et al*, Phys Rev C 40 (1989) 256.
- [62] W Bertozzi, RW Lourie and EJ Moniz in *Modern Topics in Electron Scattering*, Eds B Frois and I Sick.
- [63] AEL Dieperink and PKA de Witt Huberts in *Annual Review of Nuclear and Particle Physics*, Eds JD Jackson , HE Gove and V Luth , Volume 40 (1990) 239.
- [64] E Jens, *Workshop on Electromagnetically Induced Two-Nucleon Emission*, Tübingen March 1993.
- [65] H Herminghaus *et al*, *Proc Linear Accelerator Conference*, Albuquerque, 1990.
- [66] I Anthony *et al*, NIM A301 (1991) 230.
- [67] SJ Hall and GJ Miller, *Kelvin Lab Annual Report 1990*, 35-38.
- [68] HA Bethe and W Heitler, Proc Roy Soc (London) A146 (1934) 83.
- [69] IJD MacGregor *et al*, NIM A262 (1987) 347.
- [70] DF Measday and C Richard-Serre, CERN 69-17 (1969).
- [71] *Scintillation Materials*, NE Technology Catalogue.
- [72] JRM Annand, NIM A262 (1987) 329.
- [73] T Hehl, *private communication*.
- [74] JA MacKenzie, *private communication*.
- [75] P. Grabmayr *et al*, *Future Detectors for Photonuclear Experiments*, Edinburgh 1991 225.
- [76] JRM Annand and B Oussena, NIM A330 (1993) 220.
- [77] *The VME-bus specification*, ANSI/IEEE Std 1014-1987.

- [78] *FASTBUS Modular High Speed data Acquisition and Control System*, ANSI/IEEE Std 960-1986.
- [79] *CAMAC a Modular Instrumentation System for Data Handling*, EUR 4100 e (1972).
- [80] S Cierjacks *et al*, NIM A238 (1985) 354.
- [81] JRM Annand, *Kelvin Lab Internal Report*.
- [82] W Braunschweig *et al*, NIM 134 (1976) 261.
- [83] PA Wallace, University of Glasgow PhD Thesis (1989).
- [84] WH Barkas and MJ Berger, NASA SP-3013 (1964).
- [85] SN Dancer, University of Glasgow PhD Thesis (1987).
- [86] RA Cecil *et al*, NIM 161 (1979) 439.
- [87] R Madey *et al*, NIM 151 (1978) 445.
- [88] T Yau, *private communication*.
- [89] DG Johnston, *private communication*.
- [90] JRM Annand, I Anthony and A Sibbald, *ACQU Manual, Kelvin Lab Internal Report*.
- [91] PAW - Physics Analysis Workstation, *CERN Program Library entry Q121*.
- [92] RO Owens, NIM A288 (1990) 574.
- [93] JC McGeorge, *private communication*.
- [94] TJ Gooding and HG Pugh, NIM 7 (1960) 189.
- [95] TA Gabriel and RG Alsmiller, Phys Rev 182 (1969) 1305.
- [96] RA Crawford, *private communication*.
- [97] M Anghinolfi *et al*, Nucl Phys A457 (1986) 645-656.
- [98] J Arends, *private communication*.

- [99] PD Harty *et al*, Phys Rev C 47 (1993) 2185.
- [100] PD Harty, *private communication*.
- [101] P Rossi *et al*, Phys Rev C 40 (1989) 2412.
- [102] DA Jenkins, PT Debebeves and PD Harty, *submitted to Phys Rev C*.
- [103] L Ghedira, Thèse d'Etat de l'Université d'Orsay, Paris XI (1984).
- [104] J Ryckebusch, *private communication*.